

Synaptrode: Creating neural interfaces with axon guidance and synapse induction

Jorik Waeterschoot

Thesis submitted for the degree of
Master of Science in Nanoscience
and Nanotechnology, option
Nanobiotechnology

Thesis supervisor:

Prof. dr. S. Haesler

Assessors:

Prof. dr. ir. J. Lammertyn

Prof. dr. ir. A. Ranga

Mentors:

Ir. J. Timmerman

Dr. J. Cools

© Copyright KU Leuven

Without written permission of the thesis supervisor and the author it is forbidden to reproduce or adapt in any form or by any means any part of this publication. Requests for obtaining the right to reproduce or utilize parts of this publication should be addressed to Faculteit Ingenieurswetenschappen, Kasteelpark Arenberg 1 bus 2200, B-3001 Heverlee, +32-16-321350.

A written permission of the thesis supervisor is also required to use the methods, products, schematics and programmes described in this work for industrial or commercial use, and for submitting this publication in scientific contests.

Preface

First of all, I wish to express my sincere appreciation to my supervisor, Jasper Timmerman, who guided me throughout the past year. He taught me about writing, presenting and a wide variety of scientific skills. Without his help this thesis would not have been possible. Thank you for all the time you invested in me Jasper, I really appreciate it. I would like to extend my thanks to Professor Sebastian Haesler for his advice and for creating an interesting working environment with his enthusiasm and interesting science stories. Special regards go to Jordi Cools for his trainings on various tools, tips and tricks for cleanroom processing, assistance with SEM imaging and proofreading of the thesis. Furthermore, I would like to recognize the invaluable assistance of the lab of Professor Lammertyn especially Jolien Breukers, Iene Rutten and Lorenz Van Hileghem for their trainings on PDMS molding and fluorescence microscopy. I wish to acknowledge Katarina Dittlau from the Ludo Van Den Bosch lab for her practical insights on cell cultures in microchannel devices. I am deeply grateful to the De Wit lab, especially Luís Ribeiro, for providing and assisting with the cell cultures. Special thanks should be given to the Limone team of VIB for helping out with the imaging of several of the samples and for their microscopy trainings. Next, I would like to express my appreciation to Ailsa Lee for helping me with the proofreading of my thesis and removing the final spelling mistakes. I also want to express my profound gratitude to my parents and sisters, for their continuous support and help especially during this special lockdown period. Finally, I would like to thank the jury for reading the text and the rest of the Haesler lab for contributing to a pleasant working environment. Thank you!

Jorik Waeterschoot

Contents

Preface	i
Abstract	iv
List of Figures	v
List of Tables	ix
List of Abbreviations and Symbols	xi
1 Introduction	1
1.1 Motivation	1
1.2 Scope	2
1.3 Structure	3
2 Background and Fundamentals	5
2.1 The neuron	5
2.2 The Synaptrode project	7
2.3 Axon growth	9
2.4 Axon guidance	12
2.5 Fabrication of grooves	21
2.6 Fabrication of microchannels	23
2.7 Summary	28
3 Materials and Methods	29
3.1 Mask design	29
3.2 Master fabrication	34
3.3 PDMS molding	37
3.4 Modeling	38
3.5 Groove etching	42
3.6 Cell growth	43
3.7 Summary	43
4 Results and Discussion	45
4.1 Master fabrication	45
4.2 PDMS molding	53
4.3 Modeling	62
4.4 Groove etching	67
4.5 Cell growth	71
4.6 Impact of the Corona crisis	72

4.7	New stamp designs	77
4.8	Summary	79
5	Conclusion	81
5.1	Future work	83
A	Tools and Chemicals	87
A.1	Tools	87
A.2	Chemicals	88
B	Protocols	91
B.1	Gold alignment marks	91
B.2	SU-8 protocol: SU-8 2002 (1.6 μm) start	91
B.3	SU-8 protocol: SU-8 2002 (2.3 μm) without Ti-prime	92
B.4	SU-8 protocol: SU-8 2002 (2.3 μm) with Ti-prime layer	92
B.5	SU-8 protocol: SU-8 2050 start	93
B.6	SU-8 protocol: SU-8 2050 (120 μm) with Ti prime layer	93
B.7	Ti-prime	94
B.8	PDMS molding	94
B.9	Mask cleaning	95
B.10	Groove etching	95
B.11	Channel/groove preparation and cell culture	95
B.12	Cell fixation and staining	96
C	Supplementary Data	97
C.1	SU-8 2002 and SU-8 2050	97
C.2	PDMS-molding data	98
	Bibliography	101

Abstract

In Professor Sebastian Haesler's lab at the Neuro-Electronics Research Flanders center a new platform is being created, facilitating measurements directly from the synapse, enabled by a multi-electrode array with vertical carbon nanotube electrodes. These electrodes can be modified with synaptogenic proteins, inducing synapse formation in neurons grown *in vitro*. To isolate the synapto-electrical signal from the neuronal noise, the synapse and soma need to be measured independently. In this thesis, two techniques for synapse-soma separation were investigated: separation with the help of microfluidic channels, produced via standard soft-lithography techniques, and separation using dry-etched silicon grooves.

Using standard photolithography techniques, a two-layer SU-8 master was produced with a central channel region of approximately $2.29\ \mu\text{m}$ high, and two well regions with a height of approximately $120\ \mu\text{m}$. A wide variety of channel designs were incorporated with channel widths varying between $3\text{-}30\ \mu\text{m}$ and lengths of $500\ \mu\text{m}$. The designs were transferred to PDMS by molding, after which the stamps were plasma treated and bonded to chips/glass. All different channel designs facilitated fluid transport as long as fluid was loaded directly after bonding. All features of the channel designs larger than $3\ \mu\text{m}$ were fully resolved. A COMSOL Multiphysics model demonstrated practically isolated well regions enabling selective functionalization of the electrodes. *In vitro* cell cultures show guided axon growth, a separation of $500\ \mu\text{m}$ is achieved in approximately 6-7 DIV. The same patterns were dry etched into silicon with a depth of approximately $3\ \mu\text{m}$ using an O_2/SF_6 plasma, with all features above $3\ \mu\text{m}$ fully resolved. Future *in vitro* cell cultures will show the efficiency of the grooves in separating soma and synapse. PDMS microchannels were concluded to be the most suitable for synapse-soma separation due to their isolating properties, no damage done to the chip and ease of manufacturing.

List of Figures

1.1	Schematic overview of Synaptrode chip with microchannels for axon guidance.	2
1.2	Schematic overview of Synaptrode chip with microgrooves for axon guidance.	3
2.1	Structure of a neuron.	6
2.2	Signal transmission through a chemical synapse.	7
2.3	Schematical figure of a surface modified with synapse inducing proteins.	8
2.4	On the left side the actual Synaptrode chip. On the right side a schematical top view of the chip. Without axon guidance the neuron can either grow straight or in any other random direction.	8
2.5	Growth cone structure of an elongating axon.	9
2.6	Stages of axon outgrowth.	10
2.7	Electron microscopy images of fasciculating axons.	11
2.8	N-CAM without vs N-CAM with PSA. PSA prevents axon fasciculation.	12
2.9	Neuron guided by micron scaled grooves.	14
2.10	Upon growth in shallow grooves neurites can extend and attach to the base of the groove. When using grooves with a larger depth neurites can no longer attach to this base as a result of the neurite being too short or the bend angle too large. Consequently, deeper grooves will favor parallel growth. The green pieces of the circle indicate the most probable bend angles.	15
2.11	Neuron guided by a microchannel.	17
2.12	Funnel-shaped axon diode for unidirectional axon growth.	19
2.13	Asymmetric loop back structure for unidirectional axon growth.	19
2.14	Barbed channels trapping neurites in one direction but letting them pass in the other.	19
2.15	Asymmetric arrowhead structures, trapping neurons in one direction but letting them pass in the other.	20
2.16	Bifurcating structures to split fasciculating neurites.	21
2.17	Schematic overview of groove fabrication directly in the silicon oxide/silicon layer of the chip.	22
2.18	Overview of the microchannel fabrication process.	24
2.19	Chemical structure of the Bisphenol A Novolak epoxy oligomer.	25

2.20	PDMS polymerization reaction: dimethylvinyl-terminated dimethylsiloxane reacting with dimethylhydrogen siloxane catalyzed by a platinum complex.	27
2.21	Oxygen plasma reacting with a PDMS stamp.	28
3.1	Schematic representation of photomask 1 and 2 with the position of the different designs indicated.	30
3.2	Picture of gold alignment marks.	34
3.3	Overview of gold lift-off process for patterning of alignment marks.	34
3.4	Picture (A) and 3D illustration (B) of SU-8 2002 layer.	35
3.5	Picture (A) and 3D illustration (B) of SU-8 2050 layer on top of SU-8 2002 pattern.	36
3.6	Picture (A) and 3D illustration (B) of a PDMS stamp bonded to glass substrate.	37
3.7	Model overview, one channel (3 μm width and 10 μm interspace) and its corresponding outlet well region were modeled. At the inlet the concentration was assumed to be constant.	39
3.8	Model overview, one channel was modeled. The concentration was assumed to be constant in the well regions.	41
3.9	Picture (A) and 3D illustration (B) of grooves etched in silicon.	42
4.1	Locations of thickness measurements on the master.	46
4.2	Four different exposure doses were evaluated. 89.6 mJ/cm^2 as recommended by MicroChem, 4x184.8 mJ/cm^2 from an existing protocol at imec (Appendix B: SU-8 2002 (1.6 μm)) and 2 values in between. Only the lowest two exposure doses resulted in limited pattern broadening due to overexposure. When exposing for 89.6 mJ/cm^2 some of the channels delaminated due to underexposure.	46
4.3	Close-up SEM images of SU-8 2002 (red) structures (after sputter coating a 0.8 nm layer Pt). Even with the optimised protocol (exposure dose of 3x89.6 mJ/cm^2) not all structures are fully resolved. SU-8 is still visible in the barbs of the barbed design and the corners of diamond structures in the splitting designs are rounded.	50
4.4	SEM image of channel 13 (SU-8 colored in red). Image obtained after sputter coating 3 nm of Pt. Structures are not fully resolved.	50
4.5	SEM image of an SU-8 2050 well structure (red). Images were obtained after sputter coating 3 nm of Pt.	51
4.6	Gold alignment marks were patterned via a lift-off process on the left and right side of the wafer. In (A) the location on the mask is illustrated. A brightfield microscopy image of the smallest alignment marks patterned on the silicon wafer is shown in (B).	52
4.7	Delamination of SU-8 2050 well structures from the underlying SU-8 2002 substrate.	53

4.8	PDMS stamp produced with a one-layer master. No fluid flow was observed due to collapse of the well region. Inside the well region some circles are present, these were pillars designed to prevent the collapse of this region, but due to a too large interspacing they could not give enough support to the PDMS.	53
4.9	Brightfield image of the PDMS stamp made with a two-layer master. Fluid is pipetted inside the inlet which then flows via the channel region from the left to the right well.	54
4.10	Stereoscopy (A) and SEM images (B, C and D) of the cross-section of a PDMS stamp. PDMS is colored in blue. SEM images obtained after sputter coating 3 nm of Pt.	54
4.11	SEM images of smallest features on PDMS stamps. Features smaller than 3 μm were not fully resolved. Images were obtained after sputter coating 3 nm Pt.	55
4.12	Influence of the time between the bonding of the PDMS stamp to the glass substrate and the filling of the stamp on the fraction of channels filled.	58
4.13	Fluoresceine was added to the inlet of a PDMS stamp directly after bonding. Fluorescence signal (Olympus IX71) could be observed in the channel and in the bottom well region.	59
4.14	Fluoresceine was added to the inlet of a PDMS stamp 3 hours after bonding. Fluorescence signal (Olympus IX71) could not be observed in the channel or in the bottom well region.	60
4.15	Air bubbles were observed in PDMS chips with only one inlet per well.	60
4.16	PDMS stamp bonded to Synaptrode chip.	61
4.17	Mesh dependency study. The mean antibody concentration at 1800s modeled for different mesh densities. A mesh with 12 442 elements provided a good trade-off between accuracy and computational complexity.	62
4.18	Diffusion of the smallest (PEG-biotine) and largest (antibody) molecules to the other well region through different channel types during the functionalization process.	63
4.19	Effect of channel length on the diffusion process of the smallest (PEG-biotine) and the largest (antibody) molecules during electrode functionalization.	64
4.20	Effect of a larger well region (2000 μm high) due to inlet/outlet punching and hydrostatic pressure difference (0.979 Pa) on the diffusion of antibodies and PEG-biotine. U is the flow velocity in the channel due to a pressure difference working against the diffusion.	65
4.21	Diffusion of antibodies through different channel types during the immunostaining process.	66
4.22	Evolution of concentration profile during the immunostaining process in a 500 μm channel.	66
4.23	Brightfield images of the smallest features of Si etched grooves. Features smaller than 3 μm were not fully resolved.	67
4.24	SEM images of the smallest features of Si etched grooves. Features smaller than 3 μm were not fully resolved.	68

LIST OF FIGURES

4.25 PDMS insert can be bonded to a glass slide and seeded with cells as a control.	72
4.26 Theoretical graph of the progress of neurites inside microchannels that could possibly be obtained by life cell imaging.	73
4.27 <i>In vitro</i> cell cultures in stamps with channel design 11, 21 and 25 fixated and stained for Tau (red) and MAP2 (green) after respectively 5, 7 and 10 DIV.	75
4.28 Illustration of metric d (distance travelled in direction parallel to groove/channel) for comparing grooves with channels.	76
4.29 3D models of three new possible master designs. Design 1 (A), design 2 (B) and design 3 (C).	77
4.30 Schematic preview of masks for a first new stamp design.	77
4.31 Schematic preview of masks for a second new stamp design. Channel regions can either be isolated by punching inlets/outlets in the black dotted regions or channel regions can be connected by punching an inlet/outlet in the red dotted region.	78
4.32 Schematic preview of masks for a third new stamp design.	79

List of Tables

2.1	Overview of axon guidance by grooves with a variety of dimensions. . .	16
2.2	Overview of microchannel device characteristics used in the literature. Days indicate the days <i>in vitro</i> that the axons need to reach the other side of the channel.	18
3.1	An overview of the different channel designs. The numbers between brackets indicate the position of the design on the mask.	31
3.2	Constants and variables for modeling diffusion of antibodies and PEG-biotine through microchannels.	40
3.3	Constants and variables for calculating fluid flow due to a pressure difference inside a rectangular microchannel.	41
4.1	Thickness measurement at 5 different locations, measured with a stylus profilometer (Dektak XT). At each location the thickness of 10 channels was measured. The mean and standard deviations were calculated. . . .	45
4.2	Obtained SU-8 2002 structures after patterning with first mask containing the different channel designs. SEM images were obtained after sputter coating a 0.8 nm Pt layer.	47
4.3	Stylus profilometry (Dektak XT) measurements of patterned SU-8 2050 spin coated at two different spin speeds.	51
4.4	Fluorescence microscopy and SEM images. Fluorescence microscopy images were obtained after applying fluoresceine to one of the wells. SEM images were obtained after sputter coating 3 nm of Pt.	55
4.5	Fluoresceine was added to the inlet of a set of PDMS stamps with straight channels at 0 min, 90 min or 180 min. Every experiment was done in triplicate, mean and standard deviation were calculated.	59
4.6	Concentration in the opposite well region at 1800s for different molecules and different channel widths.	63
4.7	Concentration in the opposite well region at 1800s for different molecules and different channel lengths, for a 3 μm wide channel.	64
4.8	Brightfield and SEM images of different groove designs.	68
4.9	Profilometry measurements of etched grooves (types 2, 5 and 11). Every type was produced in triplicate (A, B and C), on each the height of 10 different channels was measured.	71

LIST OF TABLES

5.1	Pros and cons of using PDMS microchannels for synapse soma separation.	82
5.2	Pros and cons of using silicon grooves for synapse soma separation. . . .	83
C.1	Thickness measurements (Dektak XT) of patterned SU8-2002 spincoated at 1000 rpm. 10 channels were measured at each location.	97
C.2	Stylus profilometry (Dektak XT) measurements of patterned SU-8 2050 spincoated at 1500 rpm and 1000 rpm.	97
C.3	Different types of straight channel PDMS stamps produced with fluoresceine added at 0 min after bonding. The number and percentage of channels filled with fluorescent fluid was measured (Olympus IX71). Experiment was done in triplicate.	98
C.4	Different types of straight channel PDMS stamps produced with fluoresceine added at 90 min after bonding. The number and percentage of channels filled with fluorescent fluid was measured (Olympus IX71). Experiment was done in triplicate.	98
C.5	Different types of straight channel PDMS stamps produced with fluoresceine added at 180 min after bonding. The number and percentage of channels filled with fluorescent fluid was measured (Olympus IX71). Experiment was done in triplicate.	99
C.6	Fluoresceine was added to the inlet of a set PDMS stamps with straight channels at 0 min, 90 min or 180 min. Every experiment was done in triplicate, mean and standard deviation were calculated.	99
C.7	Dektak XT measurements of etched grooves (types 2, 5 and 11). Every type was produced in triplicate (A, B and C), on each the height of 10 different channels was measured.	100

List of Abbreviations and Symbols

Abbreviations and Symbols

A(m ²)	Cross-section of channel
AP	Action Potential
calcein-AM	calcein-acetoxymethyl
CAM	Cell adhesion molecules
CF	% Channels filled with neurites
C(mol/m ³)	Concentration
CNT	Carbon nanotube
DIV	Days <i>in vitro</i>
D(m ² /s)	Diffusion constant
d(m)	Distance travelled in direction parallel to groove/channel
g(m/s ²)	Gravitational acceleration
h(m)	Channel height
J(mol/m ² s)	Massflux
k(J/K)	Boltzman constant
L(m)	Channel length
MEA	Multi-electrode array
Mw(Da)	Molecular weight
NCF	Number of channels filled with neurites
NGF	Nerve growth factor
PDMS	Polydimethylsiloxane
PDL	Poly-D-lysine
PEI	Polyethylenimine
PLL	Poly-l-lysine
PLO	Poly-l-ornithine
PSA	Polysialic acid

LIST OF ABBREVIATIONS AND SYMBOLS

RIE	Reactive ion etching
$R_{hydr}(\text{Pa} \cdot \text{s}/\text{m}^3)$	Hydraulic resistance
$r(\text{nm})$	Hydrodynamic radius
SN	Amount of channels with single neurites at outlet
$T(\text{K})$	Temperature
$t(\text{s})$	Time
$U(\text{m}/\text{s})$	Flow velocity
$w(\text{m})$	Channel width
$\Delta p(\text{Pa})$	Pressure difference
$\eta(\text{Pa} \cdot \text{s})$	Dynamic viscosity
$\rho(\text{kg}/\text{m}^3)$	Density

Chapter 1

Introduction

The work described in this Master's thesis is framed within a larger research track (the Synaptrode project) being pursued in Prof. Sebastian Haesler's lab at the Neuro-Electronics Research Flanders (NERF) center located in Leuven, Belgium. The long term goal of the Synaptrode project is to facilitate and diversify the implementation of *in vitro* and *in vivo* extracellular electrophysiology research by creating interactive electrodes specific to neural subtypes for measurement of synaptic signals. This is achieved by locally immobilizing synapse-inducing proteins on the electrodes of an electrode array.

1.1 Motivation

Since early on in human history, the nervous system has attracted the attention of scientists like Herophilus and Erasistratus (360 B.C.) who studied the central nervous system in the medical school of Alexandria [1]. Some 19th century scientists including Luigi Galvani, Raymond du Bois, and Julius Bernstein also became inspired and investigated the role of bioelectricity [1, 2, 3]. They found that bioelectricity is essential for signal processing and transduction in our nervous system. Many diseases and disorders have their origin in the failure of this system [4, 5]. As new technologies are being developed to date, more and more of its mysteries can be elucidated.

Accessing the human brain *in vivo* can be invasive and thus harmful for the patient. For this very reason animals can serve as translational models, but experimenting with living organisms still requires careful reflection on a wide variety of ethical principles. Consequently, *in vitro* methods were developed that reduce the need for animal models. For example, the use of primary neurons, or stem-cell derived neurons from human origin, can present a reliable translational *in vitro* model [6, 7]. Examples of *in vitro* methods to measure the electrical signal of neurons include patch clamping and the so-called multi- or microelectrode arrays (MEAs). When performing the patch clamp a pipette tip is sealed on a small patch of the plasma membrane allowing for single channel recordings [8]. With a MEA extracellular potential signals are

measured by metallic or non-metallic electrodes [9]. However, both techniques lack the capability of addressing specific neuronal subpopulations and are not able to directly measure extracellular synaptic potentials. Since understanding synaptic function is essential for a wide variety of neurological diseases like X-linked mental retardation and schizophrenia [4], an optimised platform is required. The goal of the Synaptrode project is to create such a platform [10].

1.2 Scope

The work presented in this thesis focuses on a key aspect of the Synaptrode platform: physical separation of the neuronal cell body (soma) from the synapse-electrode interface, thus allowing isolation of the synapto-electrical signal from the neuronal noise. The platform consists of a custom-designed multielectrode array (MEA) with vertically aligned carbon nanotube (CNT) electrodes on top. Apart from significantly lowering the electrode impedance, the CNTs also serve as the anchoring points for specific synapse-inducing proteins. The MEA consist of two regions: the first region contains only CNT microelectrodes and serves as the actual cell culture area. The second region consists of CNT electrodes functionalized with neuronal subpopulation-specific synaptogenic proteins. This area is physically separated from the first by using polydimethylsiloxane (PDMS) microchannel stamps (see Figure 1.1) that only allow the passage of neuronal extension processes (i.e. axons and dendrites) or silicon-etched grooves (see Figure 1.2). Guidance of these neuronal processes is essential for synapse/soma separation, and it is the design, manufacturing and evaluation of various PDMS microchannels/silicon grooves that will be the topic of this thesis. The Synaptrode platform creates an opportunity of single-synapse measurements specific to neural subtypes, which is an important step in further understanding brain physiology.

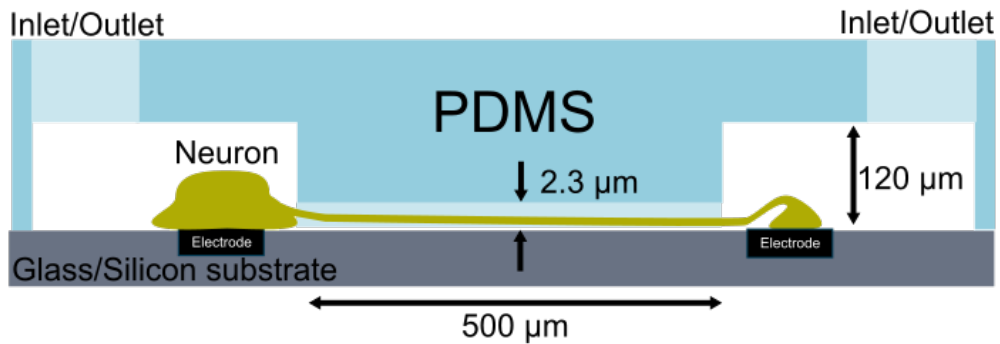


FIGURE 1.1: Schematic overview of Synaptrode chip with microchannels for axon guidance.

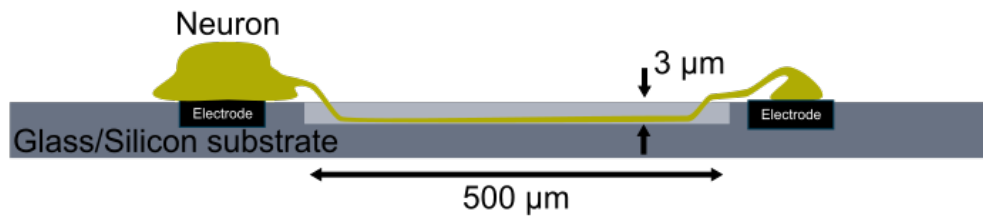


FIGURE 1.2: Schematic overview of Synaptrode chip with microgrooves for axon guidance.

1.3 Structure

Chapter two starts with a broad introduction on neurons and the Synaptrode project and ends with the state-of-the-art on axon guidance in general, and more specific by grooves and channels. Chapter three discusses the design and fabrication techniques of the PDMS microchannel stamps and silicon etched grooves, followed by a description of the techniques used for modeling diffusion inside the channels and protocols for cell culturing. Next, in chapter four the results are presented, at the end of chapter four a special Corona section is introduced with the experiments and expected results that would have been possibly achieved when no Corona crisis would have been present. The results are subsequently summarised in the concluding chapter five. All details of tools/chemicals, protocols, and supplementary data are presented in the appendices.

Chapter 2

Background and Fundamentals

The beginning of this chapter describes the biological principles of the fundamental processing unit of the nervous system, the neuron. Next, a short introduction of the Synaptrode project and the goal of the thesis is given, followed by the essential concepts on axon growth and how this growth can be guided. Finally, a more technical background on the manufacturing processes of micron-scale guiding structures is discussed.

2.1 The neuron

Neurons, a type of cell in the nervous system, are capable of receiving, propagating and transmitting electrical signals (the so-called action potentials) over distances of more than a meter [11]. A typical neuron is comprised of a soma (diameter 10-50 μm [11]), dendritic processes and an axon (Figure 2.1). The soma contains the nucleus surrounded by the cytoplasm and is responsible for the synthesis of components essential for the function and structure of the neuron. The dendrites (0.2-3.0 μm in diameter [12, 11]) receive incoming signals and have an irregular outline with the diameter decreasing along their branching. Axons have a uniform diameter (1-25 μm [11]) with a smooth appearance. Axons can propagate action potentials over long distances, eventually releasing neurotransmitters at the axon terminal (synaptic boutons) [13, 14, 11, 15].

An action potential (AP) is propagated through the axon via the following mechanism: an incoming signal depolarizes the cell membrane, opening voltage-gated Na^+ channels resulting in an influx of Na^+ (due to a concentration gradient and negative membrane potential). Na^+ diffuses inside the neuron passively spreading the local depolarization, and as a result neighboring voltage-gated Na^+ channels are activated, transporting the AP further along the axon. ± 1 ms after opening, a channel-inactivating segment from the Na^+ channel moves into the pore region preventing further influx of Na^+ (refractory period) resulting in the unidirectional transmission of an AP. Around the time the Na^+ channels close, voltage-gated K^+ channels open, resulting in an increased efflux of K^+ that hyperpolarizes the

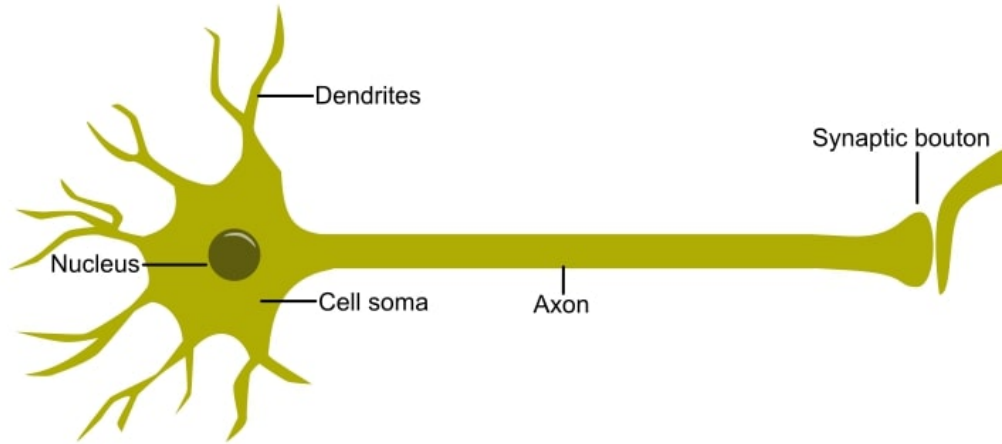


FIGURE 2.1: Structure of a neuron.

plasma membrane. Once the voltage-gated K^+ and Na^+ channels close, the membrane returns to its resting state with the help of the Na^+/K^+ pump, ready for the propagation of another action potential [16, 11, 17, 18].

2.1.1 The synapse

Neurons convey signals to other neurons with the help of synapses. Based on the mechanism, three types of synapses can be distinguished: chemical, electrical and mixed synapses. This work will solely focus on chemical synapses since these are the ones the Synaptrode interface aims to investigate [13, 19].

The non-reducible basic unit of a synapse consists of: a presynaptic zone, a synaptic cleft and a postsynaptic zone. In the presynaptic zone the machinery for storage and release of neurotransmitters is present, storing the neurotransmitters in synaptic vesicles. The synaptic cleft is the space between the plasma membranes of the connected cells (~ 20 nm). The postsynaptic zone contains postsynaptic receptors specific to the released neurotransmitter. No synapse can exist without these parts, and in most cases even more factors play an important role, e.g. support given by astrocytes and glial cells [13, 19].

As illustrated in Figure 2.2, upon the arrival of an AP at the axon terminal (1) the presynaptic membrane is depolarized, opening up the voltage-sensitive Ca^{2+} channels (2). The Ca^{2+} concentration increases in the synaptic bouton and subsequently evokes exocytosis of a synaptic vesicle (3). Next, neurotransmitters are released in the synaptic cleft and bind to receptors at the postsynaptic membrane (4). Finally, the neurotransmitters are eliminated by degradation (5a) or recycled by endocytosis (5b) [13, 19].

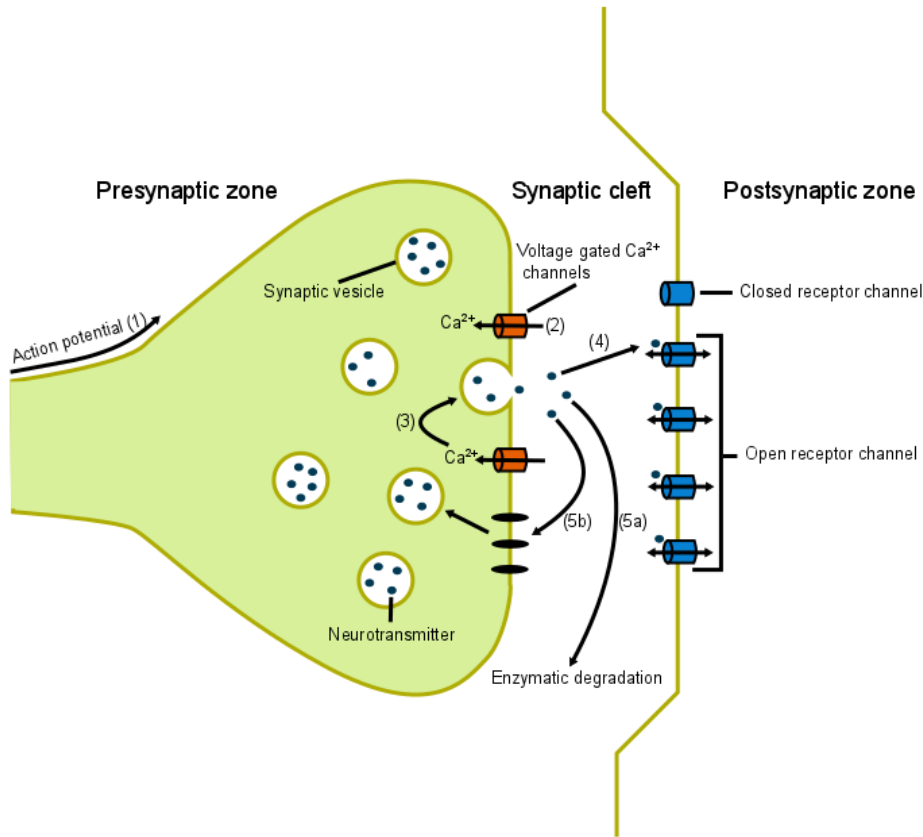


FIGURE 2.2: Signal transmission through a chemical synapse.

2.2 The Synaptrode project

After this short introduction on neurons in general, we will take a closer look at the Synaptrode project and goals of this thesis.

As indicated in the last section, synapses are an essential part of signal processing in the nervous system, and any abnormalities of the synaptic function consequently have an effect on brain function. For example, mutations in proteins that play a role in synapse formation like neuroligins and neuroligins are shown to be linked to autism, x-linked mental retardation and schizophrenia [4]. Targeting of synapses is therefore important in therapeutics for neurological disorders.

The formation of synapses is regulated in part by complex interactions between pre- and postsynaptic molecules [10]. During the past few years many pre- and postsynaptic proteins have been discovered, including ephrins, cadherins, neuroligins, neuroligins, SynCAMs and leucine-rich repeat transmembrane molecules [4]. Unpredictability in spatial and temporal formation complicates the study of their role in synapse development; thus the desire to design a new platform for the study

2. BACKGROUND AND FUNDAMENTALS

of synapses [4]. In their pursuit of creating such a platform, researchers immobilized synaptogenic proteins on abiotic surfaces [20, 21, 22, 10] (see Figure 2.3). Neurexin-1-beta dot-coated surfaces, for example, were shown to elicit dendriti- cal organization and an enrichment of postsynaptic proteins on these dots was demonstrated. SynCam1 induced presynaptical complexes [4].

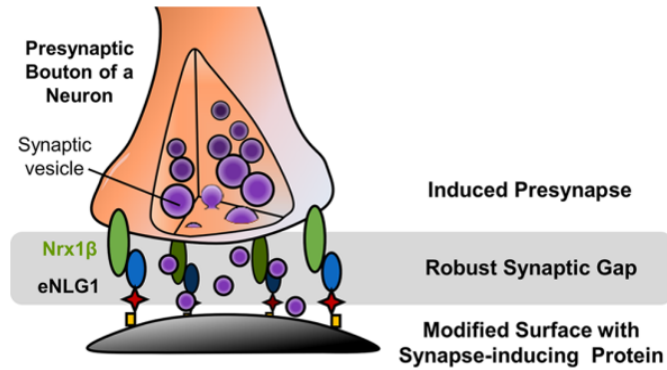


FIGURE 2.3: Schematical figure of a surface modified with synapse inducing proteins. Reprinted by permission from American Chemical Society [21].

By immobilizing synaptogenic proteins on vertically aligned carbon nanotube electrodes a new platform is being developed enabling the investigation of synapses with high spatial and temporal control. In this Synaptrode platform, neurons are grown on electrodes in one well while the growing axons are guided towards another set of electrodes functionalized with synaptogenic proteins. The separation of synapse from soma allows for single-synapse measurements (Figure 2.4). This separation by means of axon guidance will be the main goal of this thesis.

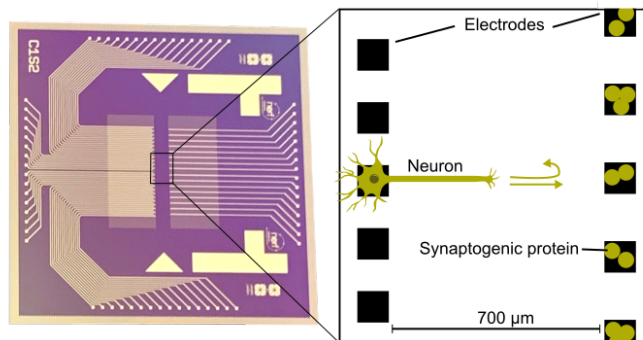


FIGURE 2.4: On the left side the actual Synaptrode chip. On the right side a schematical top view of the chip. Without axon guidance the neuron can either grow straight or in any other random direction.

2.3 Axon growth

Key in guiding axons *in vitro* is understanding the processes that come into play in *in vivo* axon growth. The location of axon growth, the growth cone, is located at the tip of the axon. The axon moves through mediation of the polymerization/depolymerization of cytoskeleton elements: microtubules and actin filaments. The growth cone can be subdivided in three domains (Figure 2.5) [23, 24]:

- **The peripheral domain:** The most distal part of the growth cone, rich in actin. This domain contains many lamellipodia, encompassing a loose meshwork of actin filaments. A large number of filopodia extend from the lamellipodia. Filopodia consist of actin-bundles undergoing cycles of elongation and retraction in response to environmental cues.
- **Transition zone:** The zone between the actin-rich peripheral domain and the microtubule-rich central domain. In this zone myosin is concentrated, enabling contraction of the actin network.
- **Central domain:** The primary site where microtubules are polymerized.

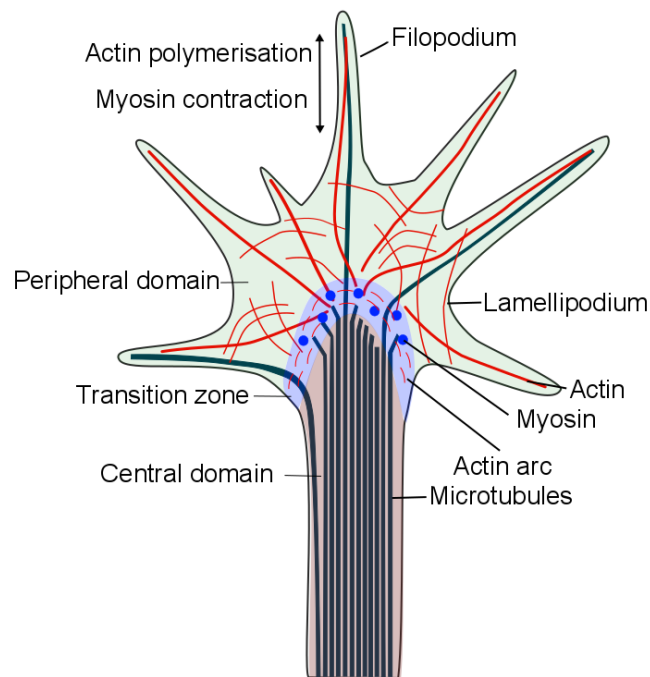


FIGURE 2.5: Growth cone structure of an elongating axon.

2. BACKGROUND AND FUNDAMENTALS

During axonal elongation three phases can be distinguished [24, 23] (Figure 2.6):

- **Protrusion phase:** The extension of lamellipodia and filopodia from the tip of the axon, mainly regulated by actin dynamics.
- **Engorgement phase:** Microtubules (MT) and organelles invade the growth cone, mostly regulated by the dynamic instability of the MT and acto-myosin interaction creating tension in the actin arcs.
- **Consolidation phase:** Interaction of microtubules and actin-associated proteins bundle the microtubules.

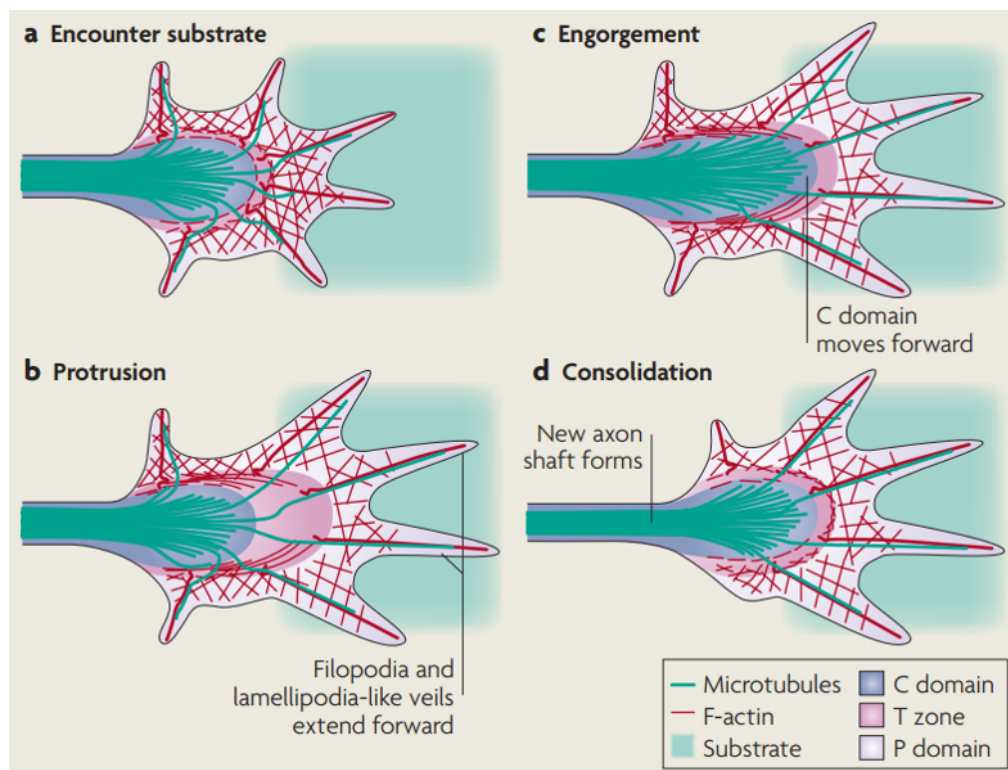


FIGURE 2.6: Stages of axon outgrowth. Reprinted by permission from Springer Nature.

Although neurites show directional growth, the dynamics are characterized by the random and constant remodeling of lamellipodia and filopodia, giving rise to a dynamic and irregular growth cone shape. When no cues are available the growth cone advances via a wandering type of motion through perpetual remodeling of lamellipodia and filopodia. When an appropriate substrate is contacted the growth cone retracts the other filopodia and flows along the contacting one. This type of movement is called 'filopodial dilation' [25].

2.3.1 Axon fasciculation

A tremendous number of connections between brain areas need to be formed. The formation of these projections is partly regulated by the fasciculation (growing alongside each other) and the defasciculation (detaching from each other) of axons (see Figure 2.7). Fasciculation processes help growing axons to reach their common target along pioneering axons. Defasciculation takes place upon arrival, every axon detaches itself from the bundle to reach its specific target. Having more than one axon in a guiding structure caused by fasciculation is potentially problematic since possibly more than one neuron will form synapses at the electrode, complicating signal analysis [26, 27, 28].

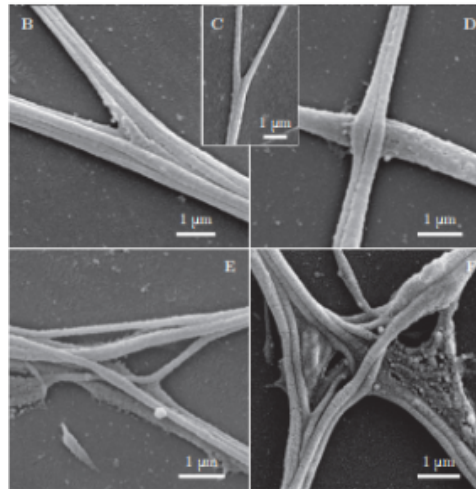


FIGURE 2.7: Electron microscopy images of fasciculating axons. Reprinted by permission from eLife [26].

One of the many regulatory mechanisms of fasciculation is the expression of cell adhesion molecules (CAM). N-CAM is involved in axon-axon adhesion [29]. By adding or removing polysialic acid (PSA) to N-CAM the cell-cell adhesion is respectively reduced or enhanced. The negative charge of PSA interacts with water and repulses other negatively charged molecules. As a result the space between the two axons will increase, preventing other adhesion molecules like L1 cadherines from getting close enough to interact (Figure 2.8) [26, 27, 29].

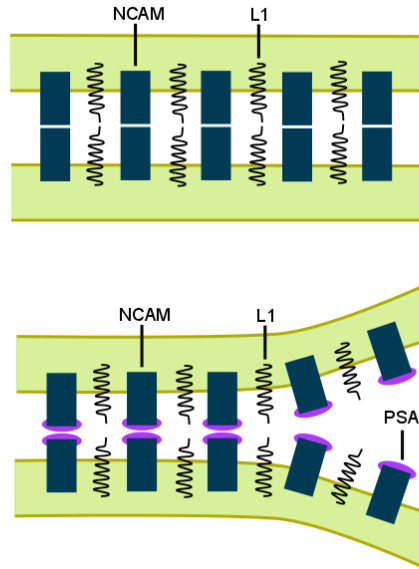


FIGURE 2.8: N-CAM without vs N-CAM with PSA. PSA prevents axon fasciculation.

It can be summarized that axons grow through a constant remodeling of their cytoskeleton elements inside the growth cone, guided by the interactions of the growth cone with the substrate. Axons do not necessarily travel alone, in most cases they fasciculate enabling the formation of dense bundles in a network. In the next section it will be elucidated how axons find their target.

2.4 Axon guidance

2.4.1 Chemical cues for axon guidance

There is a vast variety of molecules that regulate axon growth and guidance. Examples include semaphorin, ephrin, netrin, slit molecules, neurotrophic factors, ECM proteins, cell adhesion molecules (CAM), and neurotransmitters [23]. Here, we will focus on the most common molecules for *in vitro* guidance and stimulation of growth. *In vitro* there are two main strategies for chemically guiding the growth. Firstly, adhesion molecules can be patterned on a surface. Axons growth is restricted to the patterned part and as such guided [30, 31, 32], in some cases a concentration gradient of adhesion molecules is applied [33]. Secondly, axon growth can be guided by applying a gradient of a soluble molecule.

Laminin, an example of an adhesion molecule, is a high molecular weight glycoprotein with 3 subunits: alpha, beta and gamma. Laminin can bind to other laminin molecules or to proteins like collagen and as such reinforce the extracellular matrix. Binding to the integrin receptors guides and stimulates axon growth, making it a widespread

substrate for culturing neurons [34]. More than 15 laminin molecules are known, all having a similar trimer structure [30]. Axon growth from a low to a high laminin concentration in presence of a concentration gradient was demonstrated [33]. Laminin has been patterned together with non-cell adhesive molecules (PEG) to guide axon growth [30].

Another type of adhesion molecules is poly-l-lysine (PLL), poly-D-lysine (PDL) and poly-l-ornithine (PLO), which provide positive charges to a negative charged substrate enabling easier attachment of ECM proteins and cells to the substrate [35, 36, 37, 38, 39, 40, 41, 42, 43, 44].

Besides using adhesion molecules immobilised on a surface, axon growth can be guided by soluble cofactors. The neurotrophins are the best known family and contain e.g. nerve growth factor (NGF), brain-derived neurotrophic factor, and NT-3. NGF, for example, encourages axonal growth *in vitro* and *in vivo* by activating a tyrosine kinase receptor (TrkA) [30]. Another example is the application of a concentration gradient of netrin-1 or brain-derived neurotrophic factor guiding axonal growth [45]. Many more patterning techniques and guiding molecules exist but are beyond the scope of this thesis.

The application of precisely controlled gradients requires the use of complex techniques. Non-chemical guiding methods can provide an alternative and even some additional benefits. Microchannels can electrically isolate the axons, amplifying the electrical signal and microgrooves can be aligned with the electrodes of the chip with the existing lithographic techniques [46, 38, 47, 48].

2.4.2 Physical cues, topological features for axon guidance

Besides chemical cues axon growth can be guided with the help of physical cues. In this thesis 'physical cues' is used as an umbrella term for cues linked to physical phenomena and not to biochemical interactions. Example are electromagnetic radiation, temperature, topology of the surface etc.

In vivo axons can be physically guided by other axons acting as guiding structures. An example of this is the growth of axons along pioneering axons during the neuronal development phase, which depends on the geometry of the guiding structures [49]. Likewise, neurons migrate along tracks of glial cells during the development of the neocortex [50]. Additionally, peripheral nervous system guiding structures (from Schwann cells) are formed after injury, forming longitudinal tracks guiding axon growth [50]. These physical interactions between the axon growth cone and environment are regulated by the opening and closing of mechanically activated ion channels. Channels become asymmetrically activated, initiating signal cascades, influencing growth [51].

In vitro it is seen that axon growth is influenced by the topological and mechanical features of their environment just as *in vivo* [52, 49]. Growth characterized by topological guidance of the neurons is termed contact guidance. Contact guidance can be used as an engineering tool to guide growth of axons, which is further explored in the next section.

Other known axon guidance cues are the use of AC signals inducing kinetic forces including dielectrophoresis [53], IR light [54], temperature gradients [51], and microfluidic flow [55].

Grooves

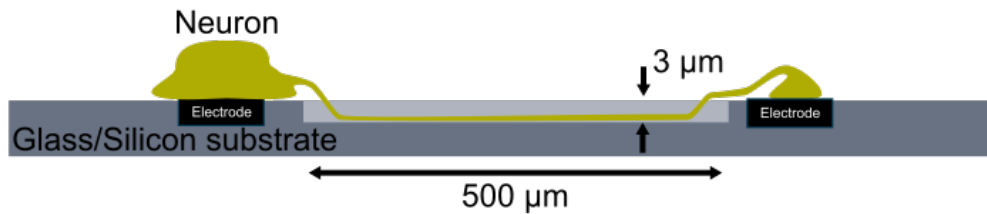


FIGURE 2.9: Neuron guided by micron scaled grooves.

Grooves with depths varying from the nm to the μm range can guide axon growth (Table 2.1) [56]. A few general trends can be discerned. The shallower the grooves, the less confined the neuron and the less polarized the growth. In some cases (for some nm sized grooves) orthogonal growth is observed [57]. The wider the groove, the less parallel the growth of the neuron will be. For very wide grooves a chance of turnback exists. Since nm scale grooves can be used for alignment it is not only the confinement that is important but also the tendency of axons to follow ridged structures [58, 59, 60, 57].

Groove depth and width influencing guiding characteristics are most likely linked to an interplay between the filopodia's adhesion to the substrate and the bending resistance of the microtubules. The growth of neurites is driven by the extension of filopodia adhering to the substrate. Depending on the groove depth the filopodia (length up to $\pm 3 \mu\text{m}$) are able to cross or not: when the depth is below $0.8 \mu\text{m}$ the filopodia have no difficulties attaching to the base of the groove. However, when the depth of the grooves increases the neurites are no longer able to touch the base, or the bend angle becomes too large (bending rigidity of the neurite cytoskeleton resists the bending mode), and as a result the neurites will grow more parallel to the grooves [50] (see Figure 2.10). Axon guidance by nm sized grooves can not be linked to the direct effect on the cytoskeleton but is probably due to an indirect effect of the grooves on signalling pathways inside the neuron (e.g. interactions of grooves with cell surface receptors). The mechanism behind this type of axon guidance has not

yet been fully elucidated and is still under investigation [61, 59, 58]. In this thesis, grooves of $3\ \mu\text{m}$ are fabricated, guiding axons by the above proposed mechanism.

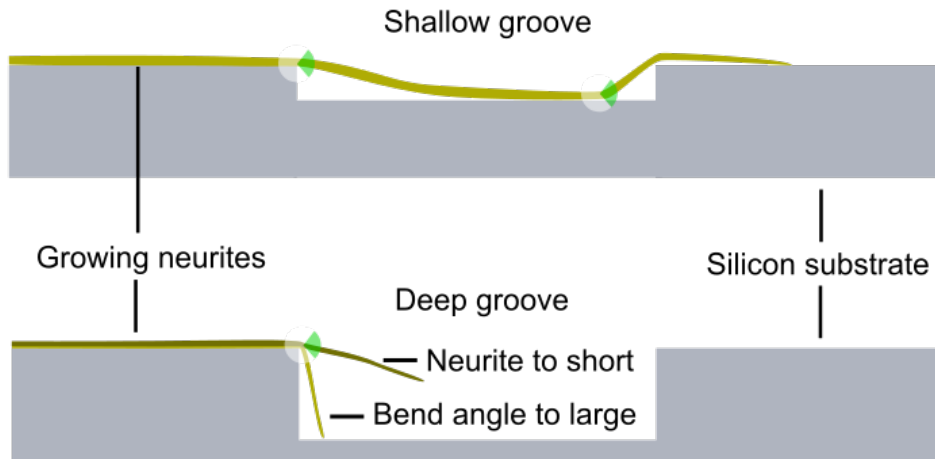


FIGURE 2.10: Upon growth in shallow grooves neurites can extend and attach to the base of the groove. When using grooves with a larger depth neurites can no longer attach to this base as a result of the neurite being too short or the bend angle too large. Consequently, deeper grooves will favor parallel growth. The green pieces of the circle indicate the most probable bend angles.

Grooves can be produced in various materials with different fabrication techniques. E.g. the photolithographic patterning/etching of SiO_2 [62], SU-8 [63] or PMMA [64], production with the help of protein crosslinking via multiphoton excitation [60], or fabrication via PDMS molding [65]. In this thesis, we will explore grooves fabricated by reactive ion etching (RIE) as in Figure 2.9. Grooves can be straight lines or can be more complex like a zigzag structure. Zigzag structures result in larger neurite directional growth awarded to the large contact area between the neurite extensions and the sidewalls [62]. Dotted patterns have been fabricated but generally don't perform as well [66].

2. BACKGROUND AND FUNDAMENTALS

Author	Depth (μm)	Width (μm)	Coatings	Cell type
Huang2018 [58]	0.016-0.224	0.198-0.904	PLL	Rat dorsal root ganglion
Terryn2018 [67]	3	4	PLO + laminin	PSC-cells
Leigh2017 [68]	1.5-8	25	PLO + laminin	Rat spiral ganglion cells (P3-5)
Chua2014 [50]	0.35-4	2	PLO + laminin	Primary murine neural progenitor cells (P5)
Li2015 [66]	1	5-15	PLL + laminin	Rat hippocampal (E18)
Bedner2012 [65]	25	5-60	PLL + laminin	Adult human progenitor cells
Barille2011 [59]	0.06	10	/	PC12 cells
Fozdar2010 [69]	0.3-2	0.4-0.5	PDL	Rat hippocampal (E18)
Gomez2007 [70]	0.4	1-2	Polyallylamine + laminin + NGF	Rat hippocampal (E18)
Gomez2007a [71]	0.4-0.8	1-2	NGF	Rat hippocampal (E18)
Francisco2007 [72]	15	20-50	Laminin	Chicken dorsal root ganglion (E10)
Lee2007 [62]	4	5-20	Fibronectin	Mouse N2a neuroblastoma
Zhang2006 [63]	5	20-40	PLL	Rat hippocampal (E18)
Mahoney2005 [64]	11	20-60	Collagen	PC12 cells
Kaehr2004 [60]	0.250	150	PLL	Neuroblastoma-glioma (NG-108-15), Rat cortical (E18-19)
Rajnicek1997 [57]	0.014-1.1	1-4	PLL	Rat Hippocampal (E16-E19), Xenopus

TABLE 2.1: Overview of axon guidance by grooves with a variety of dimensions.

Microchannels

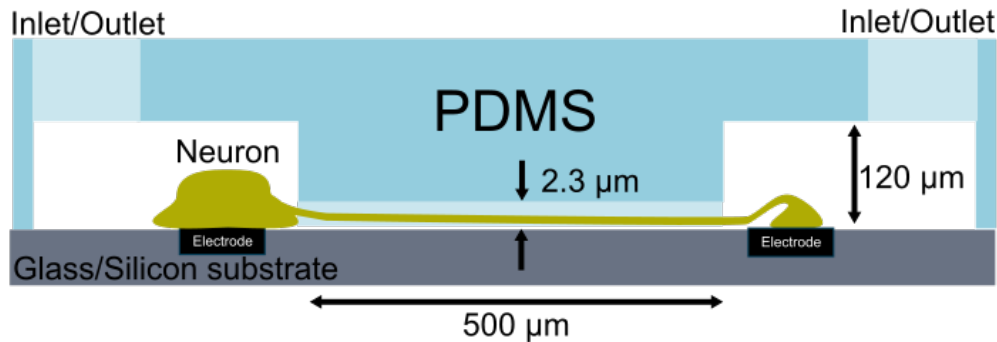


FIGURE 2.11: Neuron guided by a microchannel.

Microchannels prevent axons from crossing from one guiding structure to another, which happens frequently with grooves (see Figure 2.11). By fabricating channels longer than $450\ \mu\text{m}$ no dendrites are able to reach the other side considering their limited growth length [38]. The height of the channels are chosen so that the soma cannot enter. The soma has a minimum thickness of around $10\ \mu\text{m}$, hence channel height should be restricted to $2\text{--}5\ \mu\text{m}$ [73, 35, 36, 39, 44]. Table 3.1 shows an overview of different channel dimensions, coatings, cell types and duration of growth.

Asymmetric channels

In many cases guidance of the axon in one direction and not in the opposite is desired, which is difficult to control in straight channels since axons have the same probability of entering the channels in both directions. Asymmetric channels, for example funnel-shaped channels (axon diodes), prevent growth in the backward directions. Axons have a higher probability of entering into a wide entrance than a narrow one in the chamber wall. Once in the channel the growing speed will be the same (Figure 2.12) [79, 41].

In general, axons follow the edges of topological patterns but when the edge direction changes too abruptly, the bending stiffness of the cytoskeleton will be too large for the axon to follow. The angle under which the outgrowths are no longer able to be redirected is called the critical turning angle. This edge escape phenomenon can be used in the design of asymmetric channels [86].

One example is the loop back design (Figure 2.13) [76]. In this design the axons growing in the wrong direction are guided by a loop structure back to where they came from. When the axon travels in the right direction the bend angles for following the loop structure are too large and therefore result in the axon following a straight path.

2. BACKGROUND AND FUNDAMENTALS

Author	Width (μm)	Length (μm)	Height (μm)	Coatings	Cell type	Days
Vandewijfveven2019 [39]	10	500	5	/	Rat cortical Rat hippocampal (E17-18)	7DIV /
Habibey2017 [74]	25-40	1000	5	PDL + laminin	Rat hippocampal (E18)	9DIV
Hong2017 [75]	10	400	3	PDL + polydopamine	Rat hippocampal (E18)	3DIV
DeMarse2016 [35]	10	400	3	PDL	Rat cortical (E18)	8DIV
Renault2016 [76]	10	/	5	/	tdTomato mouse Rat cortical and hippocampal	10DIV
Habibey2015a [77]	30	800	5	PDL + laminin	Rat cortical (E18)	7DIV
Habibey2015b [78]	40	/	5	PDL + laminin	Rat cortical (E18)	10DIV
LeFebvre2015 [43]	20-10	800	5	/	Rat cortical (P1)	7DIV
Lewandowska2015 [38]	2,8,12	450	/	PEI + laminin	Rat cortical (E18)	7DIV
Malishev2015 [40]	60-161	200-1000	7	PEI	Mouse hippocampal (E18)	6DIV
Pan2015 [36]	10	400	3	PDL	Rat cortical (E18)	6DIV
Renault2015 [79]	15-2	500	3	PDL	Rat hippocampal (E19)	13DIV
Pan2014 [48]	10	/	3	PDL	Rat cortical (E18)	7DIV
Shimba2014a [80]	30	750	5	Laminin	Mouse cortical (E16)	4DIV
Shimba2014 [81]	30	700	5	PEI	Mouse cerebrocortical (E17)	10DIV
Takeyama2012 [37]	/	/	4	PEI	Rat cortical (E18)	5DIV
Peyrin2011 [41]	1,25-20	500	3	PDL	Mouse cortices and striata (E14) and transgenic GFP expressing mice	8DIV
Wieringa2010 [82]	2.5-20	1000	5	PEI	Rat cortical (P1-3)	/
Dworak2009 [42]	10	750	3	PDL	Rat cortical (E18)	5-6DIV
Morales2008 [83]	25	1000	3.7	PDL	Mouse hippocampal (E18)	7-10DIV
ClaveroL-Tinture2007 [84]	20	240	5	PLL	Helix aspersa Mouse hippocampal (E18)	/
ClaveroL-Tinture2007 [44]	60-160	70-200	7	PEI	Rat hippocampal (E18), Mouse hippocampal (E17)	6-8DIV 14DIV
Taylor2005 [85]	10	450	3	PLL	Rat hippocampal (E18), Mouse hippocampal (E17)	14DIV

TABLE 2.2: Overview of microchannel device characteristics used in the literature. Days indicate the days *in vitro* that the axons need to reach the other side of the channel.

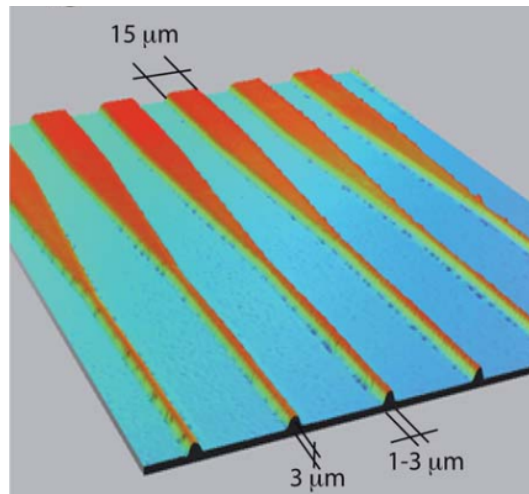


FIGURE 2.12: Funnel-shaped axon diode for unidirectional axon growth. Reprinted by permission from Royal Society of Chemistry [41].

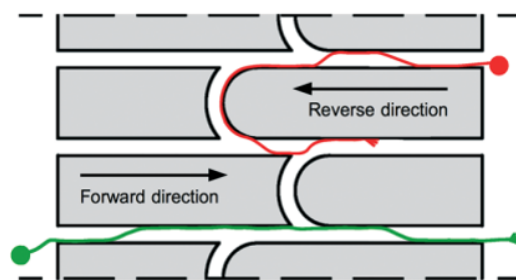


FIGURE 2.13: Asymmetric loop back structure for unidirectional axon growth. Reprinted by permission from Royal Society of Chemistry [76].

Other designs use asymmetric patterns to trap the axon in one direction but enable the passage in the other direction. Examples include the barbed patterns (Figure 2.14) [43], arrowhead patterns (Figure 2.15) [44] and all different kinds of variations.



FIGURE 2.14: Barbed channels trapping neurites in one direction but letting them pass in the other. Reprinted by permission from Frontiers in Neuroscience [43].

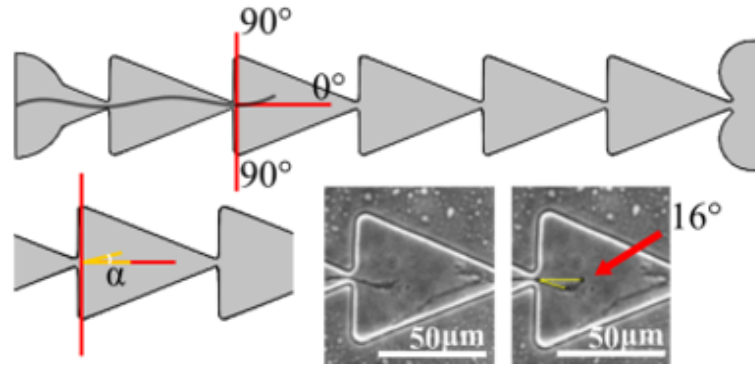


FIGURE 2.15: Asymmetric arrowhead structures, trapping neurons in one direction but letting them pass in the other. Reprinted by permission from Nature Scientific Reports [44].

Fasciculation, the entangled growth of the axons, is not always desired. In the Synaptrode project, for example, the ultimate goal is to measure single synapse activity and for this a single axon per channel is most ideal. To reduce the degree of fasciculation, bifurcated patterns can be used (Figure 2.16). The smaller the channels in the bifurcated patterns, the better the channels are able to introduce neurite separation and the probability of neurite turning becomes smaller. The explanation for the ability of the channels to separate neurites concerns the random exploratory augmentation of the neurites' growth cones. The growth cones will deviate at times from the neurite bundle. When this deviation happens at a bifurcation the neurite will be split from the axon bundle [82].

An additional advantage of using microchannels is the increase of the amplitude of an extracellularly recorded signal. By enclosure of the axon in a microchannel the volume of the extracellular fluid is reduced. Consequently, the resistance of the extracellular fluid increases, resulting in high signal strength [46, 36, 47]. The electrodes need to be positioned underneath the channel in order to make use of the effect. In the current MEA design this is not the case, but future designs could incorporate an extra array of electrodes.

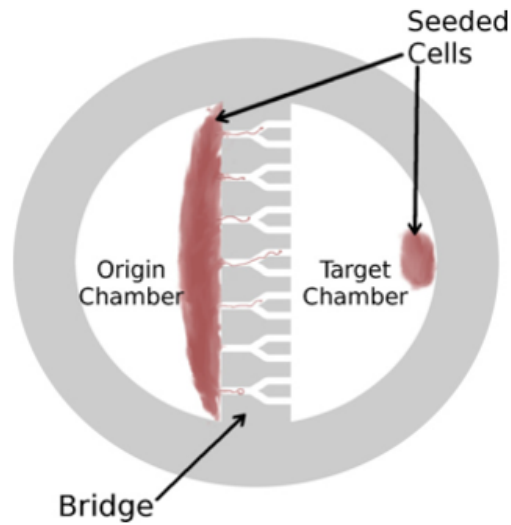


FIGURE 2.16: Bifurcating structures to split fasciculating neurites. Reprinted by permission from IOP Publishing [82].

2.5 Fabrication of grooves

This section starts with a short introduction on the general reactive ion etching (RIE) process. Next the chemical and physical reactions are discussed more in depth.

A photoresist coating can protect certain areas against the physical and chemical effects of the reactive ion etching while the non-coated parts will be exposed and be etched. Consequently, patterns can be created on different materials. In a typical process flow (see Figure 2.17) photoresist is first spin coated on a surface (1) and patterned with the help of a mask and UV light. After development, the patterns appear (3). The non-covered areas are dry etched with the help of plasma (4). Eventually the photoresist is stripped and neurons are grown on top (6) [62, 87].

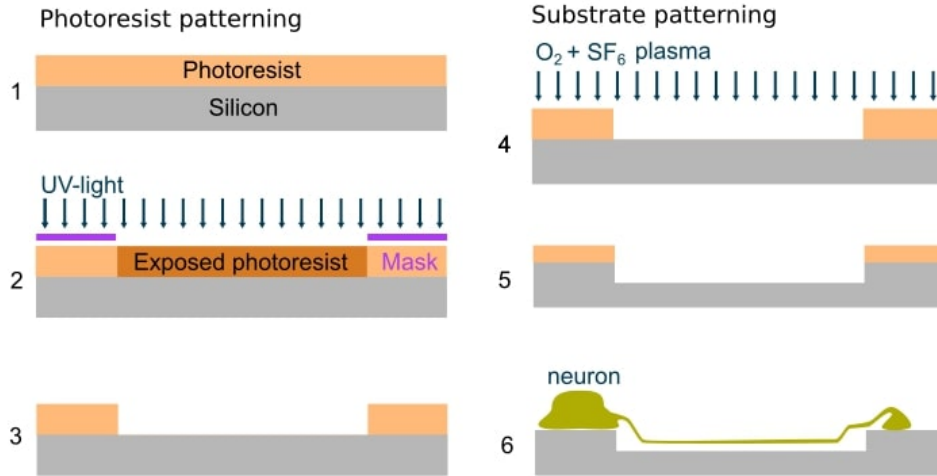


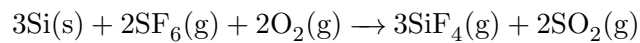
FIGURE 2.17: Schematic overview of groove fabrication directly in the silicon oxide/silicon layer of the chip.

2.5.1 RIE: reactive ion etching

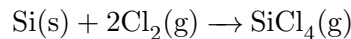
RIE is a type of dry etching utilizing a plasma. A plasma is an ionized gas with approximately the same number of ions as electrons. In RIE a combination of physical (ion bombardment) and chemical effects (reactive ion species) are used to remove material from the surface. The most important difference with classical wet etching is the directional capabilities of the process (anisotropic etching). With typical wet etching there is no control on directionality (isotropic) [88, 89, 90, 87].

The RIE process: solid + gaseous etchant \rightarrow volatile products.

The volatile etching products can easily be removed. For example etching of silicon with SF_6 or Cl_2 :



or



Typical chemicals used for etching silicon are: SiF_4 , $SiCl_4$, NF_3 , WF_6 , $AlCl_3$, $SiBr_4$. For silicon oxide etching: CHF_3 , C_2F_6 , C_3F_8 are used [88].

2.6 Fabrication of microchannels

The fabrication process of the microchannels is treated more in depth in this section. Starting with a short overview followed by a more in-depth discussion from mask making to PDMS bonding.

The Campenot devices were the first type of microchannel devices to be made for guiding axon growth [91, 92, 93]. The devices have a collagen surface containing scratches with a teflon divider on top, resulting in three chambers. By applying gradients of nerve growth factor (NGF) and seeding ganglion derived neurons in the central well, the effect of NGF on axon extensions could be investigated. Great technical skills were required to make the devices and they often exhibited leakage [91, 92].

Over the years, several methods were developed for the fabrication of microfluidic channels. Hot embossing, injection molding, 3D printing, stereolithography, micro-contact printing and many more [94]. The method that will be studied more in depth is replica molding: the molding of an elastomer by applying and letting it cure on a premade master mold. The essence of the process is visualized in Figure 2.18. This is part of a set of techniques called soft lithography techniques [95, 96]. Soft lithography uses a soft material to replicate the structure of a master. The soft character of the negative material facilitates easy separation from the hard master [97].

The obtainable resolution with the micromolding technique lies between 0.03-500 μm [97, 98]. Patterns of single-walled carbon nanotubes with a diameter of 0.5-5 nm were micromolded. At the nm length scales the molecular structure of the PDMS becomes more important [98, 99, 97]. Consequently, in this application the technique will be limited by the resolution of the SU-8 microstructures and not the molding capabilities of the PDMS [100].

To obtain a microchannel device the following steps can be taken. A layer of SU-8 is spin coated (1 and 3) and patterned by exposure through the mask (2 and 4). After being developed the mold is finished (5). For the molding process, PDMS is poured on the mold and cured by heating in an oven (6). Inlets and outlets are punched for entrance and exit of fluid and cells (7). The PDMS structure can be bonded to a silicon/glass substrate or other PDMS structures with the help of plasma bonding techniques (8) [101] (see Figure 2.18). In the following sections the different steps are reviewed in more detail.

2. BACKGROUND AND FUNDAMENTALS

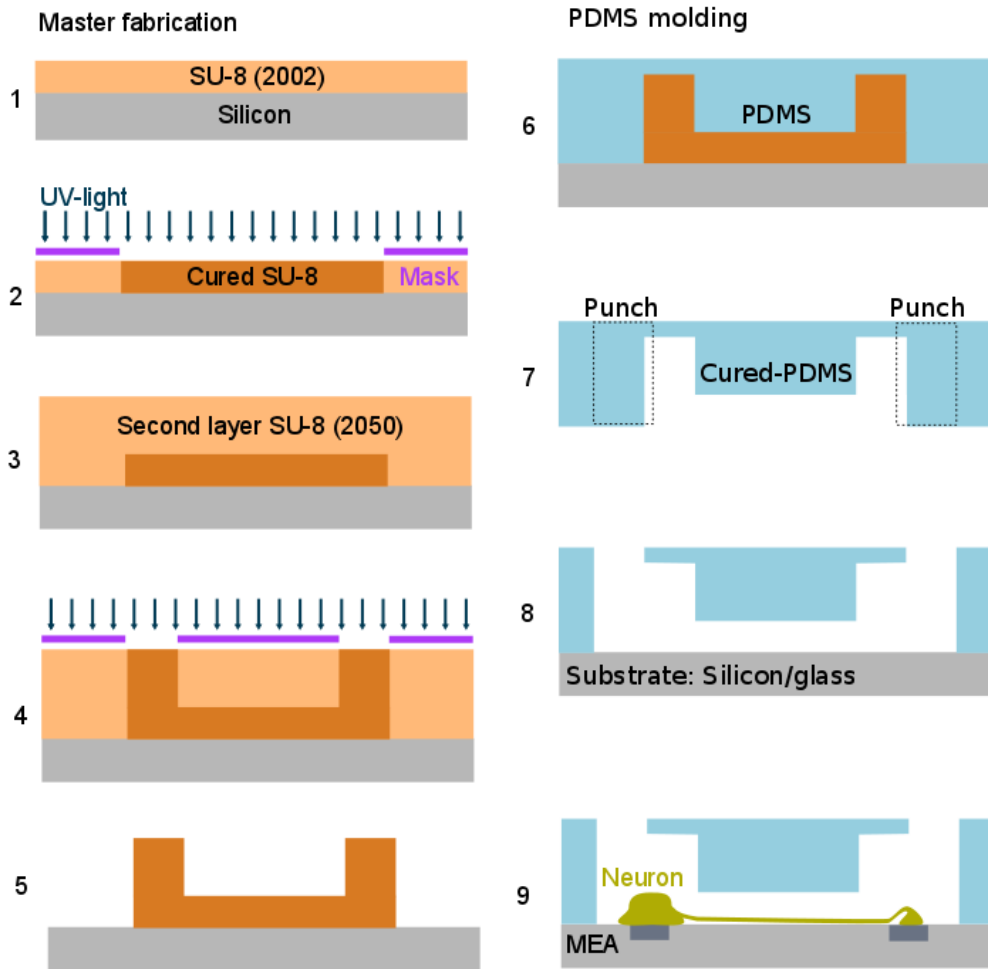


FIGURE 2.18: Overview of the microchannel fabrication process.

2.6.1 Making SU-8 master

After the design and production of the photomask, the master is made. For the fabrication of microfluidic devices SU-8 is the current standard. SU-8 has excellent mechanical and chemical stability thus enabling the use as a mold material. Additionally, SU-8 has good coating, planarization and processing properties [102, 103, 104].

Bisphenol A Novolak epoxy oligomer is one of the main components of SU-8, the structure of this molecule is depicted in Figure 2.19 [103, 105, 106]. The eight epoxy functional groups combined with a photoacid generator enable a high degree of crosslinking [107, 108, 106]. In the case of SU-8 triarylsulfonium hexafluoroantimonate (up to 10 wt%) is used. Upon UV radiation, decomposition into hexafluoroantimonic acid enables protonation of the epoxides functional groups. The protonated oxonium ions and neutral epoxides crosslink upon addition of heat, creating a dense network of cross-links. The high number of reactive sites form a strong network, giving crosslinked SU-8 thermal and mechanical stability (glass transition T of 200 °C, degradation T of 380 °C and a Young's modulus E of 4-5 GPa). Bisphenol and photoacid generator are solvated in gamma-butyrolacton, in a more recent formulation cyclopentanone is employed to improve the coating and adhesion. Layers of 2-300 μm can be produced. To get thicker layers more coatings have to be applied and to get thinner coatings SU-8 has to be diluted with solvent [103, 106].

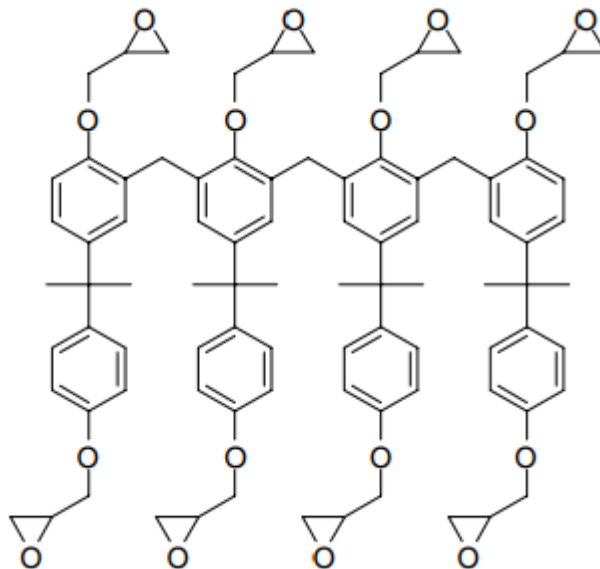


FIGURE 2.19: Chemical structure of the Bisphenol A Novolak epoxy oligomer. Reprinted by permission from Springer Publishing [103].

The photolithographic process: A substrate is chosen, in the case of this thesis a Si-wafer. SU-8 is spin coated (1000-3000 rpm depending on the SU-8 viscosity and desired thickness) on the silicon wafer. Excess solvent is removed by a soft bake where the temperature is raised to speed up evaporation while avoiding crosslinkage of the active components. A too high solvent content would generate a high film stress during the post-exposure bake [103, 109, 106].

The coating is exposed through the mask with UV-light, generating acid and producing oxonium ions. A subsequent post-exposure bake further stimulates crosslinking, increasing overall strength and decreasing solvation in developer (propylene glycol methyl ether acetate). Developer immersion solvates non-exposed photoresist, resulting in an SU-8 patterned surface [103, 106].

Wells for the depositions of cells are produced by using two-layer lithography (see Figure 2.18). In a first thin layer of SU-8 ($\sim 3 \mu\text{m}$) the channels are patterned. In a second patterning step a thicker SU-8 layer is spin coated ($\sim 120 \mu\text{m}$) to define the wells for cell culture. By puncturing inlets and outlets through the wells (in the PDMS) instead of the channels the risk of damaging the channels is reduced. Additionally the wells create a chamber protecting the cells from the outside environmental changes. The extra height is needed for the cells to be able to enter since cells have a diameter larger than $3 \mu\text{m}$ [38, 39, 40, 79, 41, 85, 42, 43, 44].

2.6.2 Casting PDMS

The material by choice to make the replica mold is PDMS. PDMS is fluid at room temperature facilitating easy application on the master. The optical transparency in the range of 240-1100 nm of the electromagnetic spectrum permits use of optical detection methods. The low autofluorescence of PDMS adds a small background signal (compared to other polymers) when using fluorescence techniques. PDMS is gas-permeable enabling the growth of cells by keeping the O_2 and CO_2 in the required range for good cell viability. The negative charge of the oxidized PDMS when in contact with neutral and basic solution supports filling of the channels with liquids with a high surface energy (like water) [110, 111, 112, 106]. Some other useful properties of PDMS are its inertness, biocompatibility, ease of fabrication, low price, low shrinkage during curing (1%) and good elastic properties [113, 101, 114, 97].

PDMS is typically made from a 3 different components: a base, curing agent and a catalyst. In most cases the base is dimethylvinyl-terminated dimethylsiloxane. The curing agent is dimethylhydrogen siloxane. The catalyst, mostly sold together with the curing agent is a metal-centered catalyst capable of promoting crosslinking. A platinum complex hydrosilyses the methylhydrogen siloxane units in the curing agent and the terminal vinyl groups in the base. The polymerization reaction can be seen in Figure 2.20 [97, 111, 106].

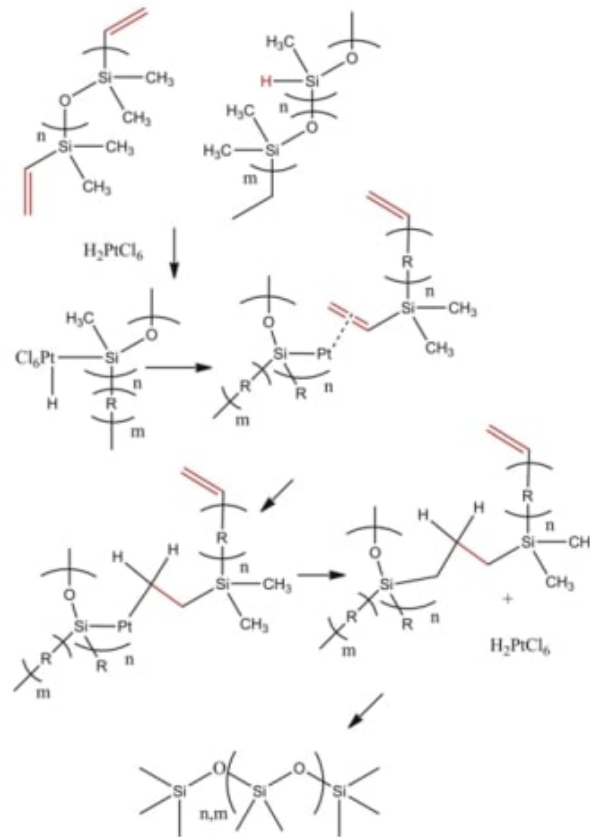


FIGURE 2.20: PDMS polymerization reaction: dimethylvinyl-terminated dimethylsiloxane reacting with dimethylhydrogen siloxane catalyzed by a platinum complex. Reprinted by permission from Elsevier [97].

To have sufficient polymerization, the base and the curing agent are mixed thoroughly together. In some cases air bubbles are formed, but can be removed by exposure to a low pressure environment. After degassing, the PDMS can be poured on the substrate and left for a few days to cure or the process can be accelerated with the help of an oven at 60-70°C [97].

Swelling of PDMS can occur when working with certain organic solvents causing feature deformation (e.g. pentane, hexane, ...). Softness of the PDMS can deform some high aspect ratio features [97, 115]. By changing the ratio of base and curing agent stiffer PDMS can be produced.

2.6.3 Plasma bonding

The PDMS stamp can be bonded to a glass or silicon surface by an oxygen plasma treatment, generating a reactive surface layer of SiOH. Once two reactive surfaces are pressed together Si-O-Si bonds are formed by condensation. Additionally, reactive SiOH groups increase wettability properties of the substrate, which is particularly useful for microfluidic applications (Figure 2.21). Care has to be taken not to expose the surface too long to the reactive plasma, which would result in the removal of all carbon components, generating brittle SiO₂ [97, 116, 117].

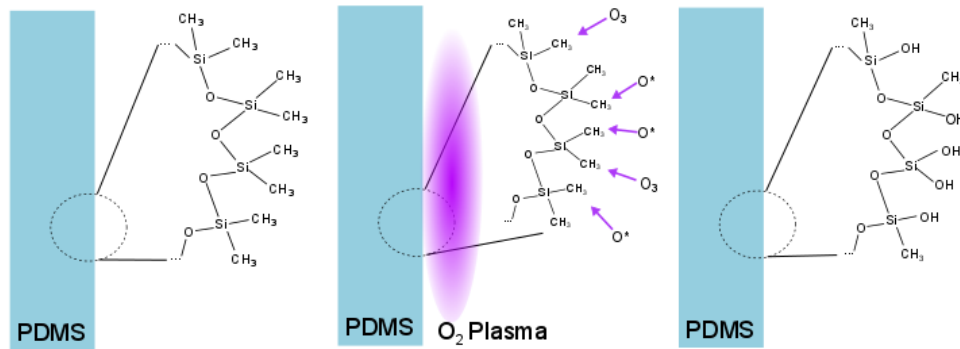


FIGURE 2.21: Oxygen plasma reacting with a PDMS stamp.

2.7 Summary

Axons grow *in vivo* by following physical and chemical guidance cues. These phenomena can be used to guide axons *in vitro*. Two methods will be explored in this thesis: physical axon guidance by microchannels and by microgrooves. Microchannels can be fabricated with the help of micromolding techniques. Grooves can be directly etched by reactive ion etching. This thesis fits in the bigger Synaptrode project facilitating separation of soma and synapse, enabling single synapse measurements.

Chapter 3

Materials and Methods

First an overview is presented of the different mask and channel designs. Next all protocols concerning master fabrication and PDMS molding are documented, followed by a description of the models made in COMSOL Multiphysics. Subsequently the protocol for groove etching is set forth. Finally, this chapter concludes with the protocols regarding cell culturing.

3.1 Mask design

Two different photomasks were designed for the two-layer SU-8 photolithographic process: the first photomask contains various channel designs and the second mask is used for the thicker well regions. Every design on mask one contains a number for determining the respective channel type during testing and a set of four alignment marks for later on chip positioning. Mask alignment marks are present on both photomasks, enabling the alignment of the first with the second SU-8 layer (see Figure 3.1).

Mask designs were created in KLayout 0.25.9 (IC layout editor). One mask (for a 4" wafer) can contain up to 35 designs for microchannel/groove fabrication. For this project, 25 different channel designs were drawn. The remaining 10 combine different channel designs and interspace distances (Table 3.1).

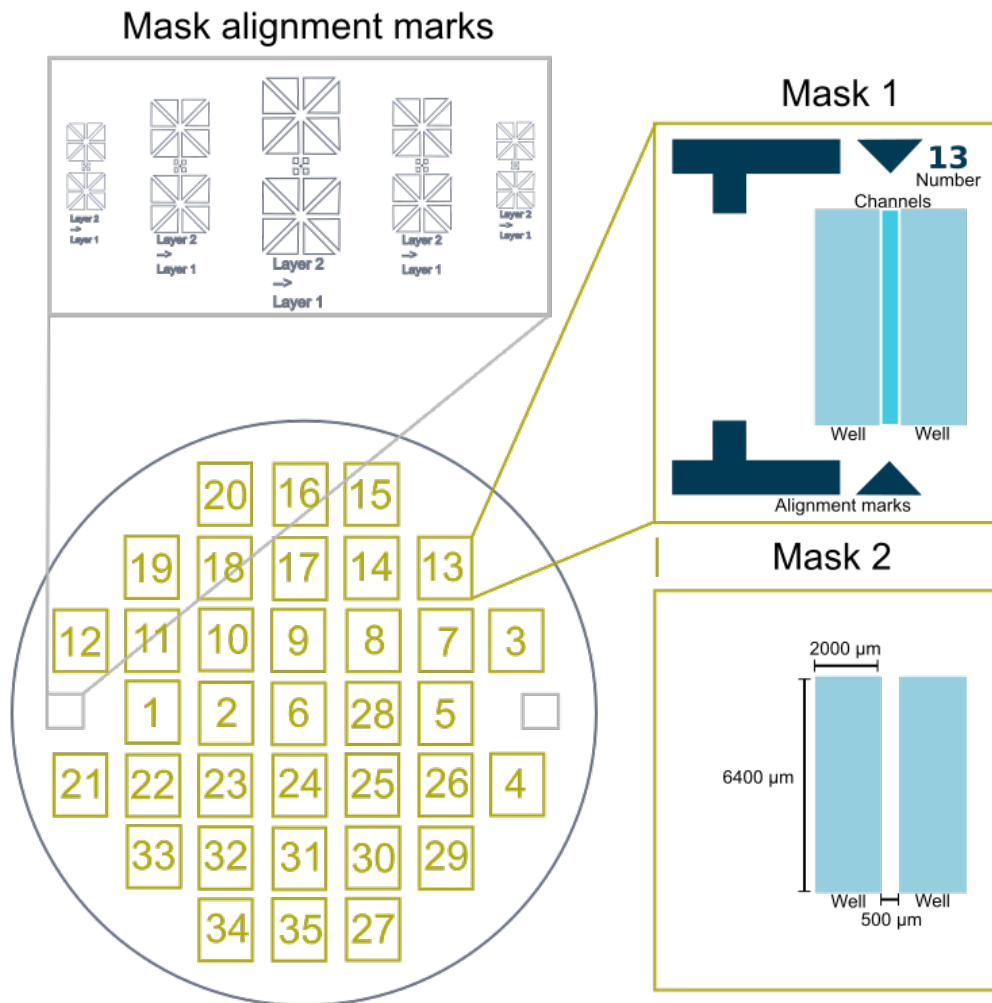

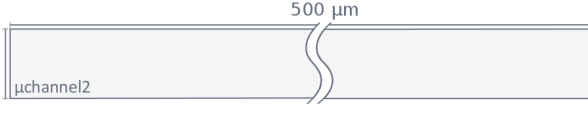



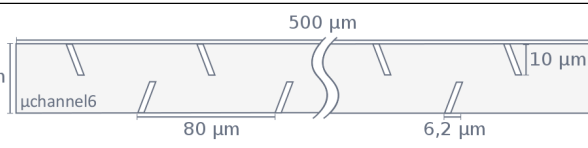
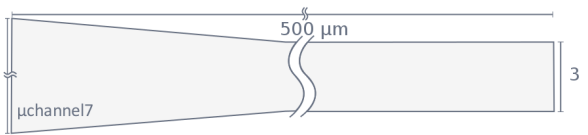
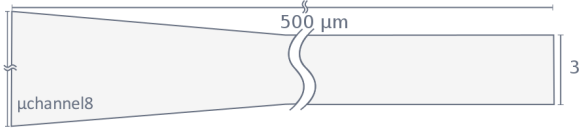
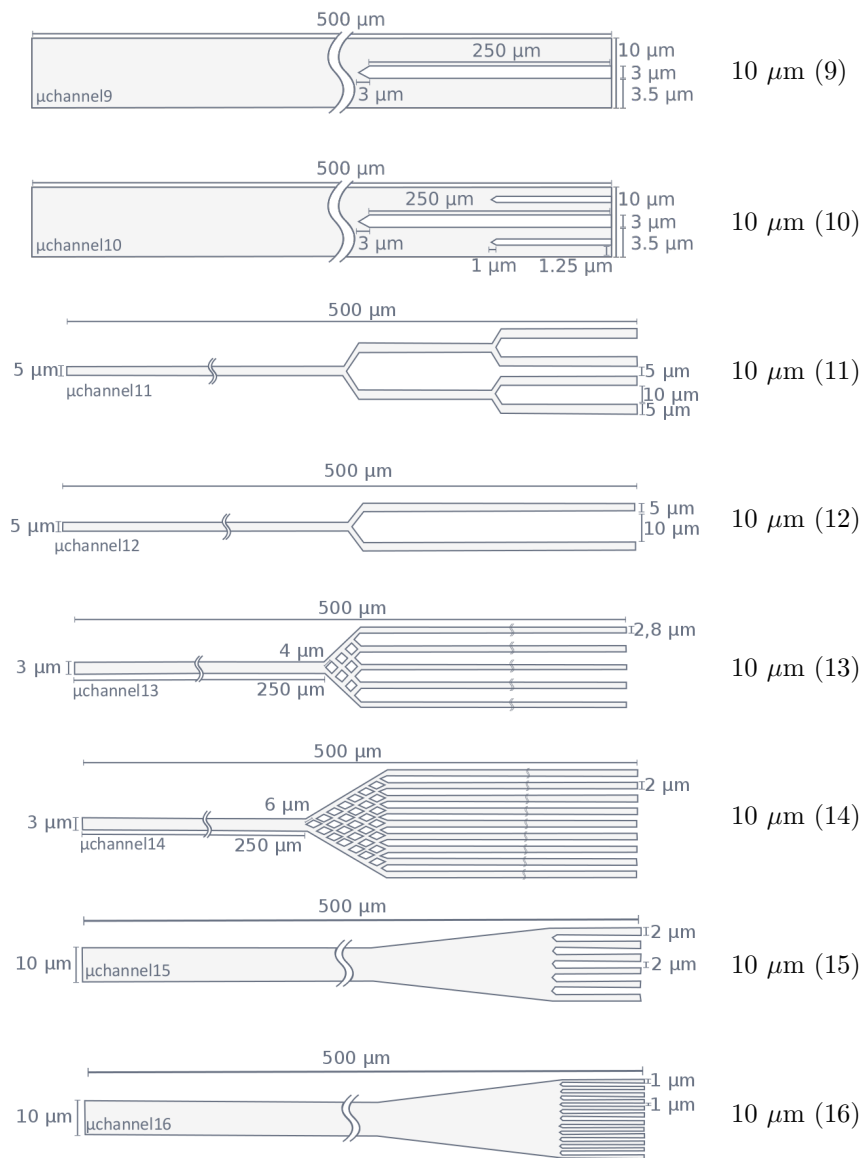


FIGURE 3.1: Schematic representation of photomask 1 and 2 with the position of the different designs indicated.

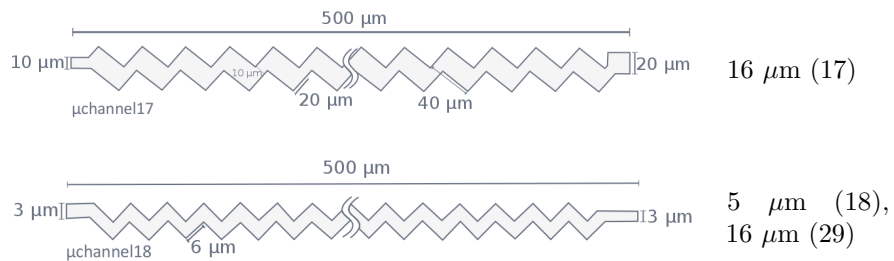
TABLE 3.1: An overview of the different channel designs. The numbers between brackets indicate the position of the design on the mask.

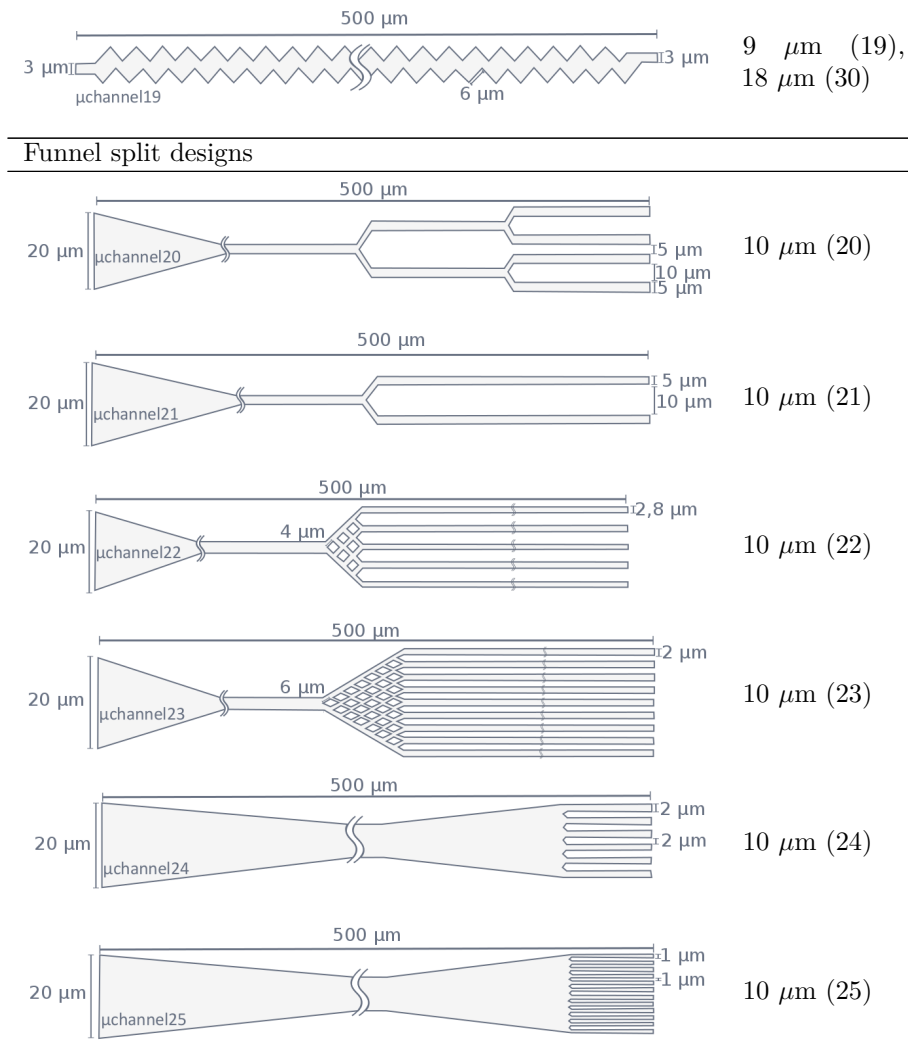
Design type	Interspace (Location)
Straight designs	
	10 μm (1), 20 μm (31), 40 μm (33), 100 μm (35)
	10 μm (2)
	10 μm (3), 20 μm (32), 40 μm (34)
	20 μm (4)
	30 μm (5)
Barbed design	
	20 μm (6)
Funnel designs	
	37 μm (7)
	17 μm (8)
Split designs	

3. MATERIALS AND METHODS



Zigzag designs





Straight designs: The first five channels have a straight design with a channel width varying between 3 and 30 μm . It is hypothesized that the larger the channel width, the higher the probability will be that an axon gets captured, but the higher the risk will be of capturing axons from different neurons [41, 40]. The channels of 3 μm were designed with 10 μm , 20 μm , 40 μm and 100 μm interspacing and the channels of 10 μm with an interspacing of 10 μm , 20 μm and 40 μm , permitting to study the effect of interspace width on PDMS stamp performance. A trade-off has to be made, the smaller the interspace width the less contact area between the stamp and the substrate the less the adherence but the more channels can be fit on the stamp.

Barbed design: This channel is designed such that axon growth is not obstructed in the forward direction but upon growing in the backward direction axons get trapped behind the barbs [43].

Funnel designs: These designs have a wider entrance than their channel width, increasing the probability of capturing axons [41].

Split designs: All split designs have branching structures splitting into many channels. This type of design could split fasciculating axons, resulting in one axon per channel, based on the random exploratory growth hypothesis [82].

Zigzag designs: A zigzag structure enhances the surface area contact and could, as such, enhance the growth of the axon [62].

Funnel split designs: Combining the funnel and split design, we aim to merge the advantages of both, i.e. higher probability of capturing axons while splitting fasciculating structures.

Mixed designs: Design 26 contains all different channels with a minimum of 10 μm interspacing. Design 27 contains 20, 21, 11, 12 with a minimum of 10 μm interspacing. Design 28 contains all the straight channel designs with a minimum of 10 μm interspacing. Design 29 contains 18 with 16 μm interspacing. Design 30 contains channel 19 with 18 μm interspacing.

3.2 Master fabrication

3.2.1 Alignment marks

For alignment of the two SU-8 layers, gold alignment marks were patterned on the surface via a metal liftoff process (see Figure 3.2 and Figure 3.3).

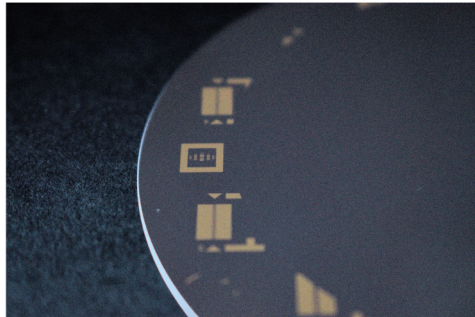


FIGURE 3.2: Picture of gold alignment marks.

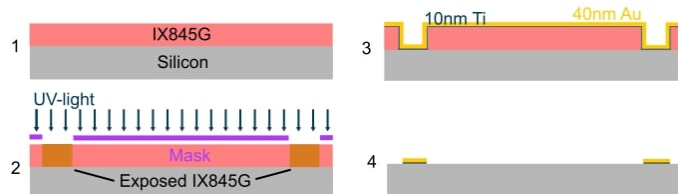


FIGURE 3.3: Overview of gold lift-off process for patterning of alignment marks.

- Dehydration bake wafer for 5 min at 190 °C
- Spin coat a layer of IX845G positive resist at 4000 rpm (30s, acceleration 1333 rpm/s)
- Bake for 1 min at 120 °C
- Expose wafer to 134.4 mJ/cm^2 (Karl Suss MA6, hard contact)
- Develop for 1 min in OPD5262
- Rinse with H_2O and dry with N_2
- Postbake for 30s at 120 °C
- Sputtercoat 10 nm Ti and 40 nm Au on the wafer
- Lift-off the Ti/Au in hot microstrip for 5 hours at 80 °C
- Transfer wafer to ultrasonic bath for 5 min
- Clean with IPA and dry with N_2
- Inspect for defects

3.2.2 Layer 1: SU-8 2002 (2.3 μm)

In a second step the first layer of the master, with the design of the different channels, is fabricated (Figure 3.4). A Ti-prime layer ensures a good adhesion of the SU-8 on the substrate.

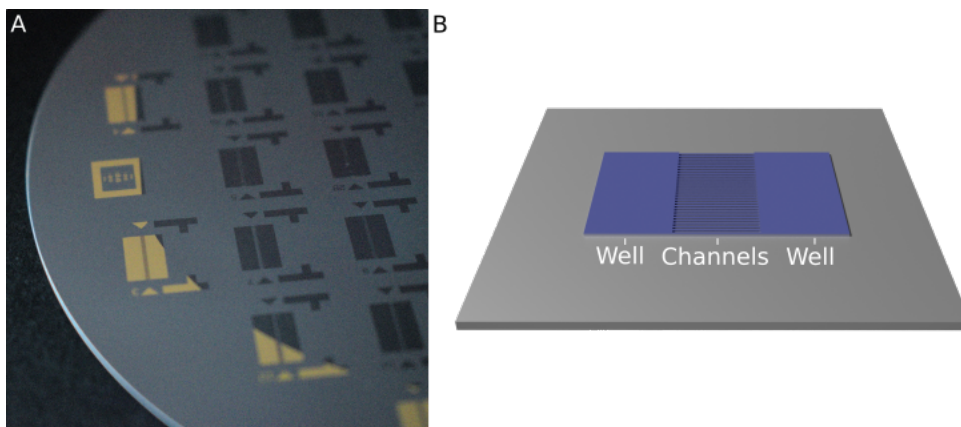


FIGURE 3.4: Picture (A) and 3D illustration (B) of SU-8 2002 layer.

- Dehydrate the wafer by baking for 5 min at 190 °C
- Spin coat Ti-prime at 2000 rpm (30s, acceleration 667 rpm/s)
- Bake the wafer for 5 min at 190 °C
- Apply SU-8 to the wafer by spin coating, 5s at 500 rpm (acceleration 100 rpms/s) and 30s at 1000 rpm (acceleration 300 rpm/s)
- Wait 15 min for wafer relaxation

3. MATERIALS AND METHODS

- Prebake 2 min at 65 °C and 2 min at 95 °C (Gradual T transition by holding wafer 10s above hotplate)
- Expose wafer to 89.6 mJ/cm^2 (Karl Suss MA6, hard contact)
- Post-illumination bake wafer on hotplate for 2 min at 65 °C and 2.5 min at 95 °C (Gradual T transition by holding wafer 10s above hotplate)
- Develop illuminated wafer for 1 min in SU-8 developer
- Take wafer out beaker and rinse with SU-8 developer, dry with N₂
- Hard bake wafer on hotplate 10 min at 130 °C
- Place wafer in hot IPA and dry with N₂
- Inspect for defects and measure thickness with stylus profilometer (Dektak XT)

3.2.3 Layer 2: SU-8 2050 (120 μm)

In a third step the second layer of SU-8 (SU-8 2050) is spin coated. SU-8 2050 results in thicker structures essential for the fabrication of the wells for cells to grow in (see Figure 3.5). A Ti-prime interlayer is used to enhance adhesion between both SU-8 layers.

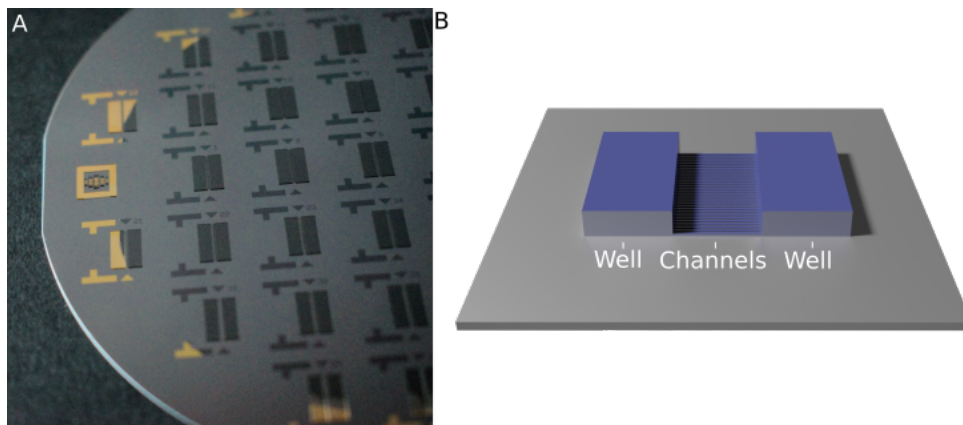


FIGURE 3.5: Picture (A) and 3D illustration (B) of SU-8 2050 layer on top of SU-8 2002 pattern.

- Dehydrate the wafer by baking for 5 min at 190 °C
- Spin coat Ti-prime at 2000 rpm (30s, acceleration 667 rpm/s)
- Bake the wafer for 5 min at 190 °C.
- Apply SU-8 to the wafer by spin coating, 5s at 500 rpm (acceleration 100 rpm/s) and 30s at 1500 rpm (acceleration 300 rpm/s)
- Wait 60 min for wafer relaxation
- Heat wafer on a the hotplate from room temperature till 95 °C over 20 min. Keep the wafer for 20 min at 190 °C and then eventually let the wafer gradually cool down for 30 min

- Expose wafer to $8 \times 184.8 \text{ mJ/cm}^2$ with 14s between every cycle (Karl Suss MA6, soft contact)
- Post-illumination bake wafer on hotplate by gradually increasing the temperature to $95 \text{ }^\circ\text{C}$ in 20 min followed by 10 min at $95 \text{ }^\circ\text{C}$ and a gradual decrease in temperature over 30 min
- Develop illuminated wafer for 20 min in SU-8 developer
- Take wafer out beaker, rinse with SU-8 developer and IPA, dry with N_2
- Hard bake wafer on hotplate by gradually increasing the temperature to $130 \text{ }^\circ\text{C}$ over 20 min, bake for 5 min at $130 \text{ }^\circ\text{C}$ and gradually let the wafer cool again to room temperature
- Place wafer in hot IPA and dry with N_2
- Inspect for defects and measure thickness with stylus profilometer (Dektak XT)

3.3 PDMS molding

The manufactured master can be used for the production of microchannels by pouring PDMS on top and subsequently curing the PDMS into an elastic stamp. These PDMS stamps can be removed from the reusable master mold, and bonded to a silicon or glass substrate after oxygen plasma treatment (Figure 3.6).

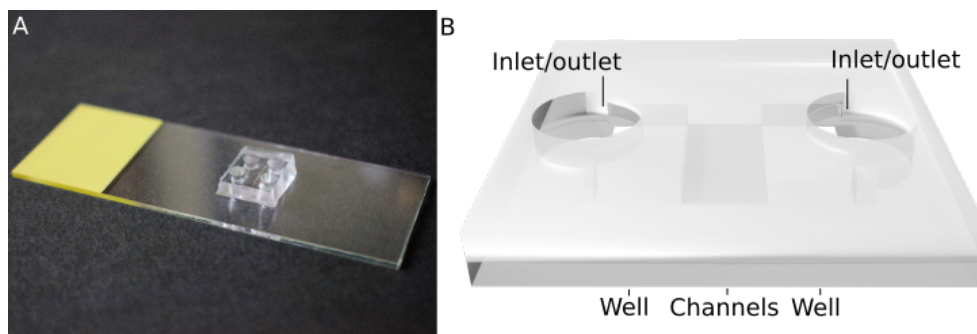


FIGURE 3.6: Picture (A) and 3D illustration (B) of a PDMS stamp bonded to glass substrate.

A Preparing PDMS (Sylgard 184)

- Weigh 50 mg (for 4" wafer) of PDMS
- Add curing agent (10% off the mass of PDMS), mix the solutions well
- De-gas the solution by applying negative pressure, wait around 20 min until no more bubbles are visible and a clear PDMS solution appears
- Place the wafer inside an open container such as a petridish or aluminium crucible
- Pour the degassed PDMS carefully on the mold

3. MATERIALS AND METHODS

B Curing PDMS

- Cure the PDMS in an oven at 50 °C for 2 h

C PDMS bonding

- Remove container and peel PDMS off the SU-8 mold
- Puncture inlet and outlet holes (3 mm biopsy puncher, Miltex)
- Use the plasma cleaner to activate the surface of stamp and glass slide/chip. 2 min at high level (RF power: 30 W, Pressure: 0.380 Torr), transforming the Si-CH₃ of the PDMS to Si-OH. When in contact with the same functional groups, strong and permanent Si-O-Si links are formed
- Bring glass/chip in contact and squeeze gently to ensure contact without closing the channels

Fluid flow is visualised with colored fluid (water-based food coloring, for more details see Appendix A) and fluoresceine (0.1 mg/ml) with the help of an inverted fluorescence microscope (Olympus IX71).

To investigate the effect of interspace and channel width on PDMS stamp performance the different straight channel designs with different interspace widths (Designs: 1, 2, 3, 4, 5, 31, 32, 33, 34 and 35) were monitored with fluoresceine (0.1 mg/ml) and an inverted fluorescence microscope (Olympus IX71). PDMS stamps were filled 0 min, 90 min and 180 min after PDMS bonding in triplicate. For every test the percentage of channels filled with fluid was calculated. Kruskal-Wallis tests were performed to determine whether differences were present between the various channel types for the three different time intervals. Wilcoxon rang-sum tests were executed to look at difference between the three different time intervals. Non-parametric tests were chosen since the data was not normally distributed (evaluated with a Shapiro-Wilk test).

To examine the effect of the number of inlets/outlets in the PDMS on the performance of the stamp, nine PDMS stamps with one 3 mm inlet/outlet at each side, nine PDMS stamps with one 8 mm inlet/outlet at each side (by punching several times with 3 mm biopsy puncher), and nine PDMS stamps with two 3 mm inlets/outlets at each side were fabricated and tested by inserting fluoresceine (0.1 mg/ml) directly after bonding and imaging with an inverted fluorescence microscope (Olympus IX71).

Apart from glass slides, PDMS stamps were also bonded on Synaptrode chips that were treated with or without oxygen plasma.

3.4 Modeling

Two phenomena were modeled: first, the ability of microchannels to fluidically isolate the two well regions [41], which could be useful for selectively functionalizing one of the two arrays of electrodes. The second modeled phenomenon is the characteristics of antibody diffusion, useful to determine the effectiveness of immunostaining techniques to visualize biological structures.

3.4.1 Fluidic isolation

All modeling was performed in COMSOL Multiphysics 5.3.0. Due to the symmetry of the problem it was sufficient to model only one channel with corresponding well regions (see Figure 3.7). The concentration at the inlet well (i.e. the location where possible functionalization takes place) was specified to be constant at 1 mM (as applied in the Synaptrode project). The initial concentrations of the channel and the second well region (i.e. the region which did not need to be functionalized) were assumed to be 0 mM. Two types of molecules were modeled: antibodies and PEG-biotine, which respectively have the largest and smallest diffusion constant of the molecules used in the functionalization process (see Table 3.2). Diffusion was modeled using Fick's laws (see equations (3.1) and (3.2)). The diffusion constant was obtained with the help of equation (3.3), equation (3.4) and the constants in Table 3.2. J being the massflux in mol/m^2s , C the concentration of antibody or PEG-biotine dependant on the model in mol/m^3 and t the time in s. The fluid level is assumed to be equal in both wells, as such no fluid flow is present.

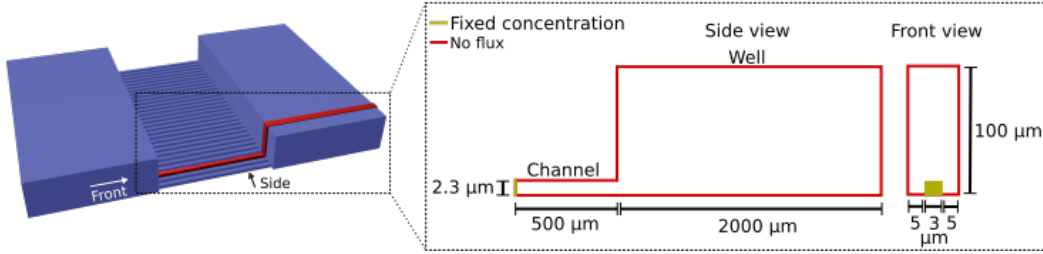


FIGURE 3.7: Model overview, one channel ($3 \mu\text{m}$ width and $10 \mu\text{m}$ interspace) and its corresponding outlet well region were modeled. At the inlet the concentration was assumed to be constant.

$$J = -D \frac{\partial C}{\partial x} \quad [118] \quad (3.1)$$

$$\frac{\partial C}{\partial t} = D \frac{\partial^2 C}{\partial x^2} \quad [118] \quad (3.2)$$

$$r \approx 0.081 \cdot \sqrt[3]{Mw} \quad [119, 118] \quad (3.3)$$

$$D = \frac{k \cdot T}{6\pi \cdot \eta \cdot r} \quad [119, 118] \quad (3.4)$$

3. MATERIALS AND METHODS

	Antibody	PEG-Biotine
Mw(Da): Molecular weight	$1.50 \cdot 10^5$ [120]	$5.89 \cdot 10^2$ [121]
r(nm): Hydrodynamic radius	4.30377	0.67885
D(m ² /s): Diffusion constant	$5.1736 \cdot 10^{-11}$	$3.2378 \cdot 10^{-10}$
k(J/K): Boltzman constant	$1.38065 \cdot 10^{-23}$ [122]	
T(K): Temperature	294.15	
η (Pa·s): Dynamic viscosity (water)	$9.76 \cdot 10^{-4}$ [122]	

TABLE 3.2: Constants and variables for modeling diffusion of antibodies and PEG-biotine through microchannels.

A mesh dependency study was executed to find the optimal balance between calculation time and accuracy. For this study, the mean concentration of antibodies in both channel and well area was calculated after 3600s for different mesh densities. Secondly, the diffusion of both PEG-biotine and antibodies was investigated for channels with a width of 3 μm , 5 μm and 10 μm , all with 10 μm interspace and length of 500 μm . Finally, the diffusion of the two types of molecules in channels with lengths of 100 μm , 200 μm , 300 μm , 400 μm and 500 μm and width of 3 μm with 10 μm interspace was determined.

In practise, the well areas will be larger due to the punching of inlets/outlets. A new model with a well height of 2000 μm instead of 100 μm was instantiated for both antibodies and PEG-biotine. Additionally, the effect of a pressure difference over the channel region working against the concentration gradient was modeled. With the help of equation (3.5) the hydrostatic pressure difference was calculated based on a water level difference of 1000 μm (fluid level of 1000 μm in one well and 2000 μm in the opposite well). This pressure difference, together with the hydraulic resistance (calculated with equation (3.6) for Poiseuille flow in rectangular channels and the constants in Table 3.3) were used as an input for equation (3.7). The flow velocity U was incorporated into the model as an extra convection term inside the channel, this term was assumed to be constant in time. The flow velocity of fluid inside the well region was assumed to be zero.

$$\Delta P = \rho \cdot g \cdot \Delta h [122] \quad (3.5)$$

$$R_{hydr} = \frac{12\eta \cdot L}{1 - 0.63 \frac{L}{h}} \cdot \frac{1}{h^3 \cdot w} [123] \quad (3.6)$$

$$U = \frac{\Delta P}{R_{hydr} \cdot A} [123] \quad (3.7)$$

$\rho(kg/m^3)$: Density (water)	998.004 [122]
$g(m/s^2)$: Gravitational acceleration	9.81 [122]
$\Delta h(m)$: Water level difference	$1.00 \cdot 10^{-3}$
$\Delta p(Pa)$: Pressure difference	0.9799
$\eta(Pa \cdot s)$: Dynamic viscosity (water)	$9.76 \cdot 10^{-4}$ [122]
$L(m)$: Channel length	$5.00 \cdot 10^{-4}$
$w(m)$: Channel width	$3.00 \cdot 10^{-6}$
$h(m)$: Channel height	$2.30 \cdot 10^{-6}$
$A(m^2)$: Cross-section	$6.9 \cdot 10^{-12}$
$R_{hydr}(Pa \cdot s/m^3)$: Hydraulic resistance	$3.104 \cdot 10^{17}$
$U(m/s)$: Flow velocity	$4.571 \cdot 10^{-6}$

TABLE 3.3: Constants and variables for calculating fluid flow due to a pressure difference inside a rectangular microchannel.

3.4.2 Immunohistochemical staining

Fluidic isolation could possibly be problematic for the immunostaining of axons inside the channels. Therefore, this phenomenon was modeled to get an idea of the diffusion times of antibodies (and thus staining times) through the channel. A new model with only one channel was created (see Figure 3.8). At both sides a concentration of 1 mM was applied. The same formulas and constants were used as in the previous model. Different lengths of 100 μm , 200 μm , 300 μm , 400 μm and 500 μm were investigated.

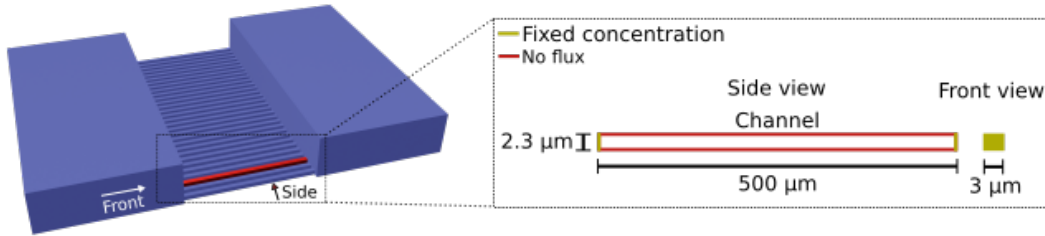


FIGURE 3.8: Model overview, one channel was modeled. The concentration was assumed to be constant in the well regions.

3.5 Groove etching

The following protocol was used in combination with the first photomask to produce grooves with a depth of $\pm 3 \mu\text{m}$ (see Figure 3.9).

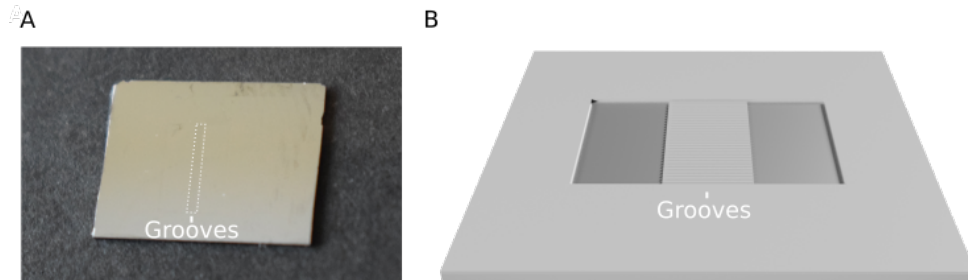


FIGURE 3.9: Picture (A) and 3D illustration (B) of grooves etched in silicon.

- Spin coat IX845 at 4000 rpm for 30s (acceleration 1333 rpm/s)
- Bake 60s at 120 °C
- Expose wafer to $341.6 \text{ mJ}/\text{cm}^2$ (Karl Suss MA6, hard contact)
- Develop 1 min in OPD5262
- Bake 10s at 120 °C
- Rinse with H_2O and dry with N_2
- Expose to O_2/SF_6 plasma for 7 min (RF: 60 W, ICP: 100 W, O_2 : 10 sccm, SF_6 : 40 sccm) with the Oxford plasmalab 100
- Submerge in acetone until all resist is removed
- Rinse with H_2O and dry with N_2
- Clean in hot IPA for 30s and dry with N_2
- Inspect for defects and measure thickness with stylus profilometer (Dektak XT)

3.6 Cell growth

After plasma bonding the PDMS stamps were immediately loaded with H_2O or 70% ethanol, the inlets were then covered with scotch tape to prevent leakage during transportation. Grooves can be directly transported to the cell lab after fabrication. Once arrived at the cell lab the stamps/grooves were sterilized.

Stamps/grooves preparation and cell culture:

- Sterilise the channels by exposing the samples to UV radiation for 60 min
- Coat overnight with 0.1 mg/ml PLO and 0.01 mg/ml laminin in sterile borate buffer 1x
- Seed approximately 50 000 (in the channels) or 25 000 (on the grooves) E19 embryonic mouse hippocampal cells with DMEM + horse serum
- Use Neurobasal + B27 as subsequent growth medium, replace half of the medium every two days
- Incubate at 37 °C and 5% CO_2

3.7 Summary

An overview was given of the collection of protocols used for master fabrication, PDMS molding, channel modeling and groove etching. At last the steps that have to be taken for *in vitro* cell culture were presented.

Chapter 4

Results and Discussion

This chapter will sequentially discuss the results regarding master template and PDMS microchannel device fabrication and characterization, diffusion modelling using the COMSOL Multiphysics software and microgroove etching fabrication and characterization. Next a Corona section describes the experiments that would have been carried out in the normal course of the thesis. Finally this chapter finishes with three new stamp designs.

4.1 Master fabrication

4.1.1 Layer 1: SU-8 2002

An existing SU-8 protocol (Appendix B: SU-8 2002 (1.6 μm), used previously at imec) was optimized to obtain a desired layer thickness of approximately 2-3 μm with the best possible resolution (resolution limited by the 3 μm resolution of the mask).

Thickness: Based on the MicroChem datasheet [124] spin speeds of 3000, 1000, 900 and 800 rpm were evaluated. Thicknesses of resulting structures were measured with a stylus profilometer (Dektak XT). A spin coating speed of 1000 rpm resulted in the desired thickness and uniformity of $2.29 \mu\text{m} \pm 0.04 \mu\text{m}$, which would result in microchannels high enough for axons to enter. The uniformity of the layer was determined by measuring the thickness of 10 channels at five different locations (see Figure 4.1). With a standard deviation of 0.04 μm , we show uniformity in layer thickness across the sample using our protocol (see Table 4.1).

	Mean (μm)	SD (μm)
N	2.309	0.002
E	2.309	0.002
S	2.22	0.02
W	2.308	0.003
Mid	2.297	0.007
Overall	2.29	0.04

TABLE 4.1: Thickness measurement at 5 different locations, measured with a stylus profilometer (Dektak XT). At each location the thickness of 10 channels was measured. The mean and standard deviations were calculated.

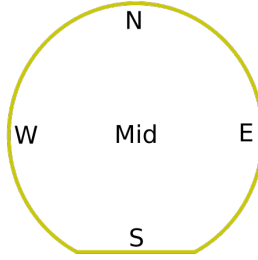


FIGURE 4.1: Locations of thickness measurements on the master.

Exposure: The exposure dose was varied to determine optimal development conditions for the SU-8 layer. Exposure doses of 89.6 mJ/cm^2 , $3 \times 89.6 \text{ mJ/cm}^2$, $2 \times 196 \text{ mJ/cm}^2$ and $4 \times 184.8 \text{ mJ/cm}^2$ were assessed. Insufficient exposure resulted in SU-8 delamination as a result of only partial cross-linking of the SU-8 close to the substrate. Larger exposures resulted in a deterioration of pattern resolution due to pattern broadening. An exposure dose of $3 \times 89.6 \text{ mJ/cm}^2$ resulted in the best achievable resolution without delamination of patterns (see Figure 4.2).

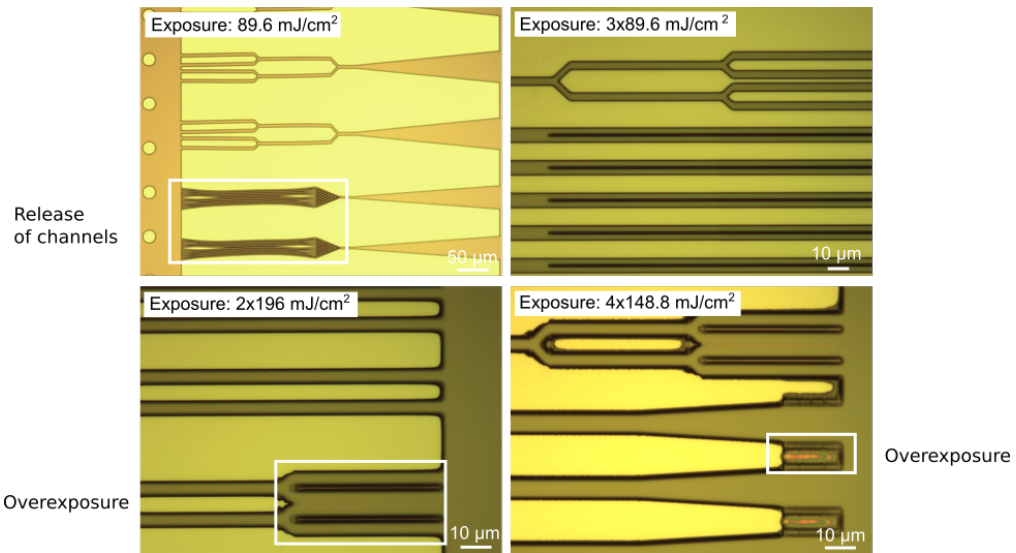

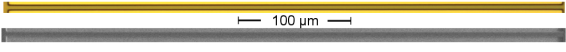



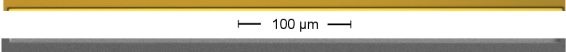

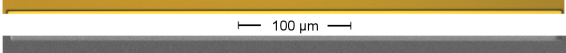

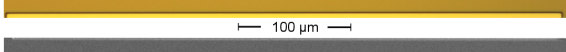

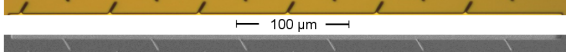

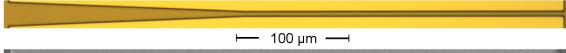

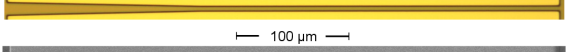

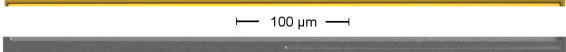

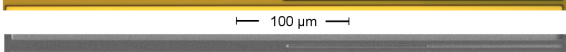
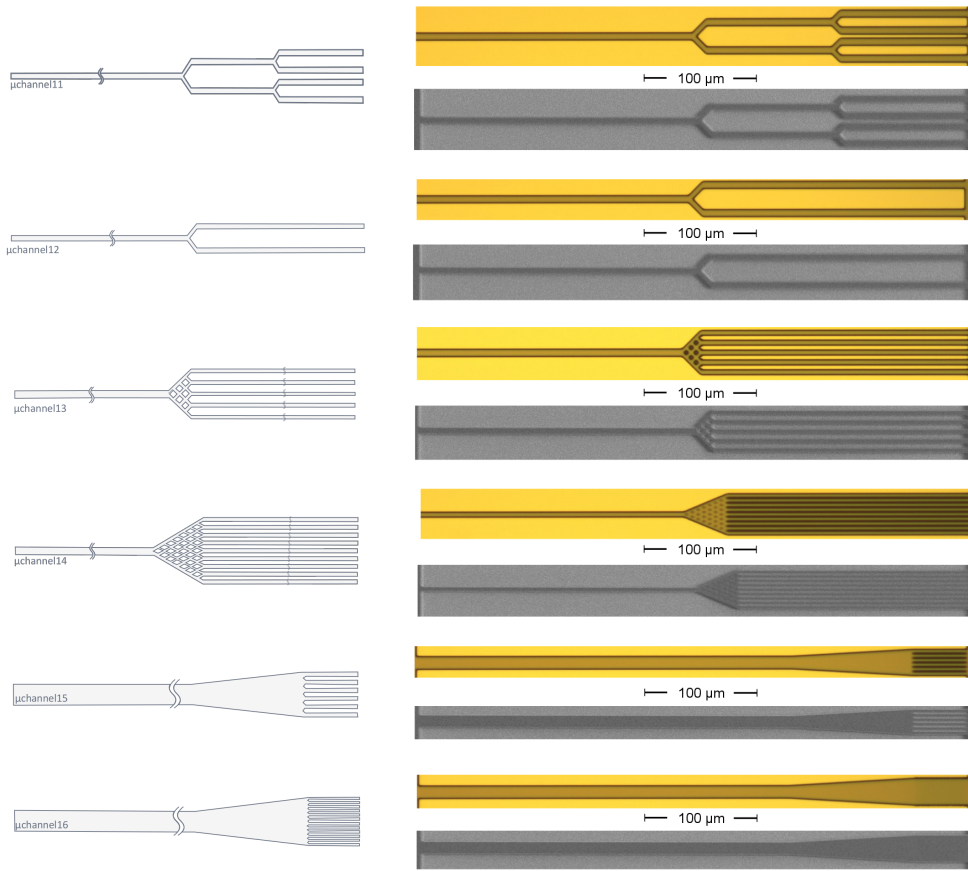


FIGURE 4.2: Four different exposure doses were evaluated. 89.6 mJ/cm^2 as recommended by MicroChem [124], $4 \times 184.8 \text{ mJ/cm}^2$ from an existing protocol at imec (Appendix B: SU-8 2002 ($1.6 \mu\text{m}$)) and two values in between. Only the lowest two exposure doses resulted in limited pattern broadening due to overexposure. When exposing for 89.6 mJ/cm^2 some of the channels delaminated due to underexposure.

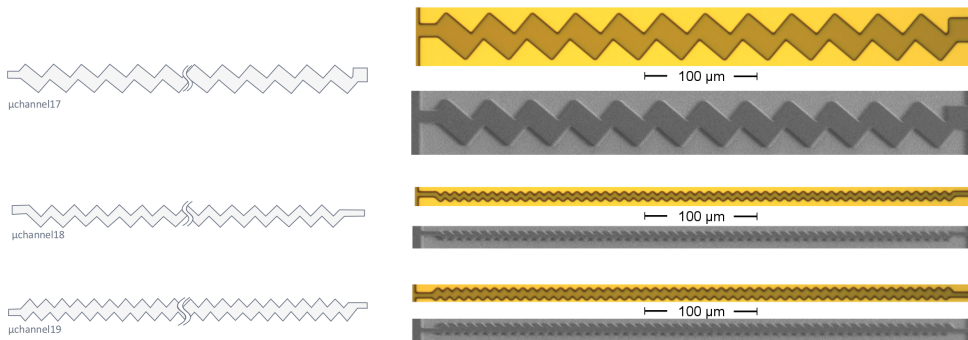
TABLE 4.2: Obtained SU-8 2002 structures after patterning with first mask containing the different channel designs. SEM images were obtained after sputter coating a 0.8 nm Pt layer.

Design	Brightfield and SEM
Straight designs	
 μ channel1	
 μ channel2	
 μ channel3	
 μ channel4	
 μ channel5	
Barbed design	
 μ channel6	
Funnel designs	
 μ channel7	
 μ channel8	
Split designs	
 μ channel9	
 μ channel10	

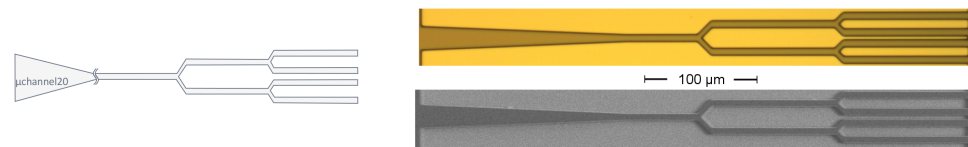
4. RESULTS AND DISCUSSION

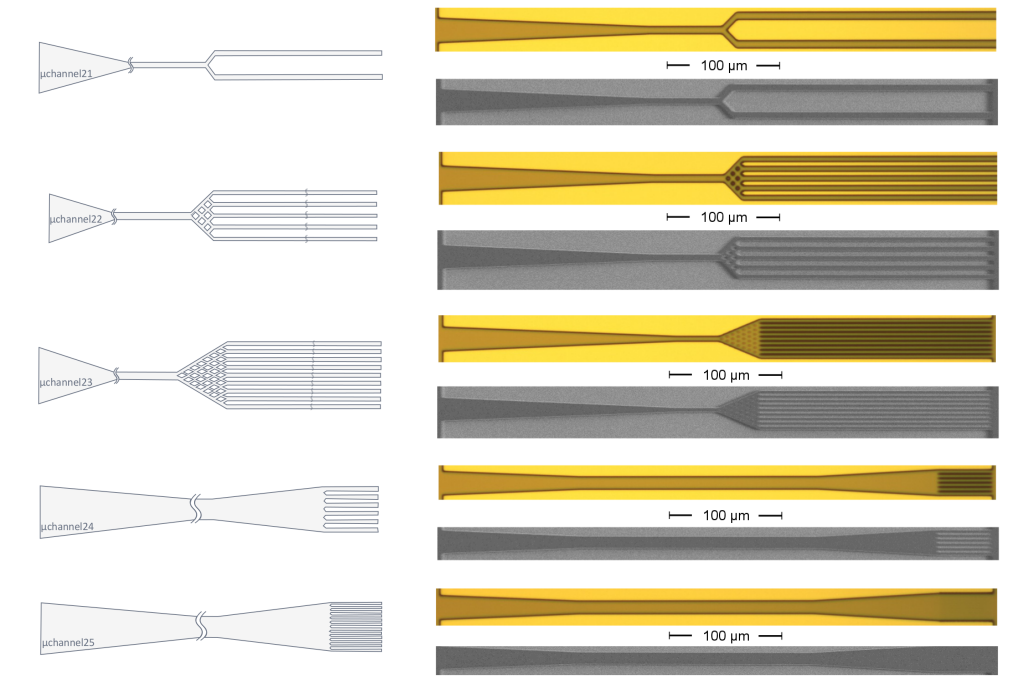


Zigzag designs



Funnel split designs





Pattern resolution was evaluated using SEM imaging. In Figure 4.3 and Figure 4.4 it can be observed that structures smaller than $3 \mu\text{m}$ were not fully resolved. In channel 6, for example, some material was left in the barbs, the corners of the diamond structures were rounded (channels 13, 14, 22 and 24) and spikes smaller than $3 \mu\text{m}$ were no longer present (channels 10, 15, 16, 24 and 25). To get a higher resolution a quartz mask can be used instead of the current soda-lime mask (with resolution of $3 \mu\text{m}$).

In a later stage, during removal of the PDMS stamps from the master mold, delamination of the SU-8 pattern from the substrate occurred. An additional processing step was introduced to extend the lifetime of the master mold. A Ti-prime layer was deposited under the SU-8 2002 layer. The exposure dose had to be reoptimized as a result of the change in reflectivity of the surface [125]. An exposure dose of $89.6 \text{ mJ}/\text{cm}^2$ resulted in similar results as earlier reported for $3 \times 89.6 \text{ mJ}/\text{cm}^2$ without Ti prime layer.

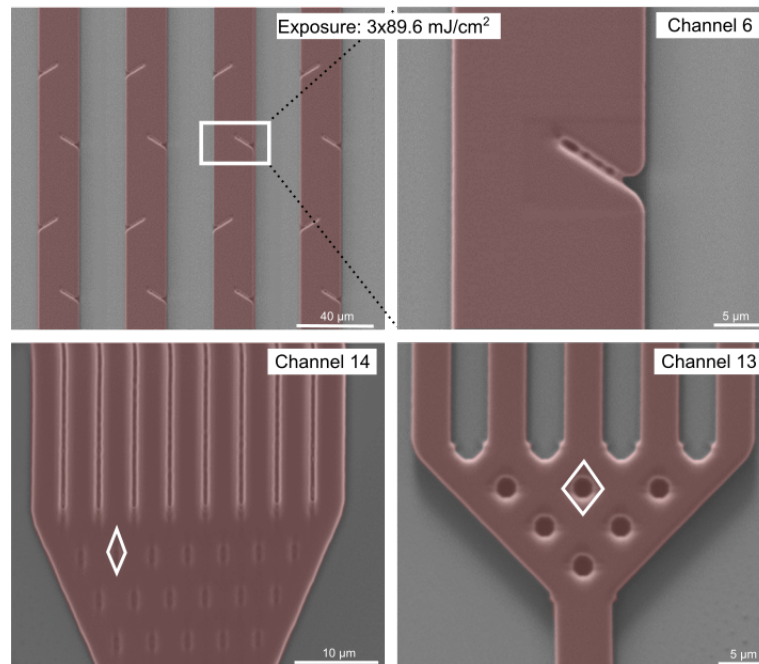


FIGURE 4.3: Close-up SEM images of SU-8 2002 (red) structures (after sputter coating a 0.8 nm layer Pt). Even with the optimised protocol (exposure dose of $3 \times 89.6 \text{ mJ/cm}^2$) not all structures are fully resolved. SU-8 is still visible in the barbs of the barbed design and the corners of diamond structures in the splitting designs are rounded.

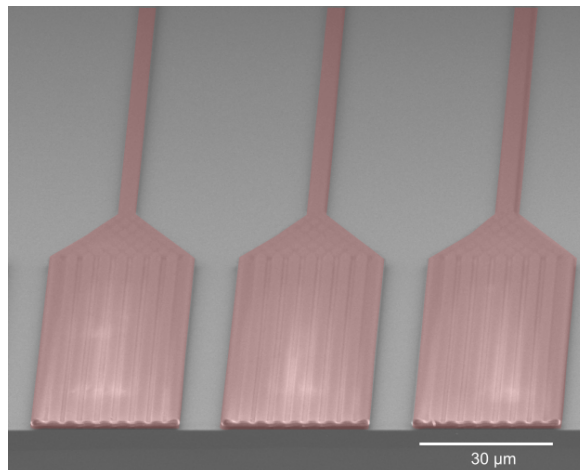


FIGURE 4.4: SEM image of channel 13 (SU-8 colored in red). Image obtained after sputter coating 3 nm of Pt. Structures are not fully resolved.

4.1.2 SU-8 2050

The protocol for the production of the thicker, second SU-8 layer for well formation was optimized starting from the data stated in the MicroChem datasheet (Appendix B: SU-8 2050 start). Initially, the SU-8 layer remained stuck to the mask, indicating incomplete baking and/or exposure. Therefore, three preventative measures were taken: 1) the softbake time was increased from 20 min to 25 min; 2) the exposure dose was increased from 392 mJ/cm^2 to $8 \times 184.8 \text{ mJ/cm}^2$; 3) the mask aligner was used in soft-contact mode to decrease contact (i.e. pressure) between the mask and the SU-8. The first two measures allow for more solvent to evaporate and the UV-exposed SU-8 to fully cross-link.

Layer thickness was evaluated with the Dektak XT for two different spin speeds: 1000 rpm and 1500 rpm (see Table 4.3). Higher spin speeds positively correlate with layer uniformity but correlate negatively with layer thickness [126]. Eventually a spin speed of 1500 rpm was chosen resulting in a layer thickness of $120 \pm 20 \text{ }\mu\text{m}$.

To confirm the results obtained with the Dektak XT, a SEM image of the profile was obtained by cleaving samples at the site of the well structure (i.e. along the channel direction). The samples were prepared for SEM visualization by sputter coating three nm of Pt on top. As shown in Figure 4.5, a thickness of $100.17 \text{ }\mu\text{m}$ was measured, a value similar to the thickness measured with the Dektak XT. Additionally, the negative slope at the top of the structure can be recognized as T-topping. This phenomenon occurs due to the strong absorption of UV-light shorter than 350 nm by the SU-8 structures, resulting in the accumulation of acid at the top which diffuses to the sides giving a T-profile [127]. Another cause of this phenomenon could be the occurrence of small air gaps between the mask and the SU-8 during exposure (possibly due to the soft contact). Light gets diffracted leading to a broadening of patterns at the top [128]. T-topping is not problematic for this project as long as the thicker well structures are transferred to the PDMS.

	1500 rpm	1000 rpm
N (μm)	105.792	164.405
E (μm)	124.285	173.772
S (μm)	157.634	268.175
W (μm)	95.785	210.437
Mid (μm)	103.992	149.490
Mean (μm)	$1.2 \cdot 10^2$	$1.9 \cdot 10^2$
SD (μm)	$2 \cdot 10$	$5 \cdot 10$

TABLE 4.3: Stylus profilometry (Dektak XT) measurements of patterned SU-8 2050 spin coated at two different spin speeds.

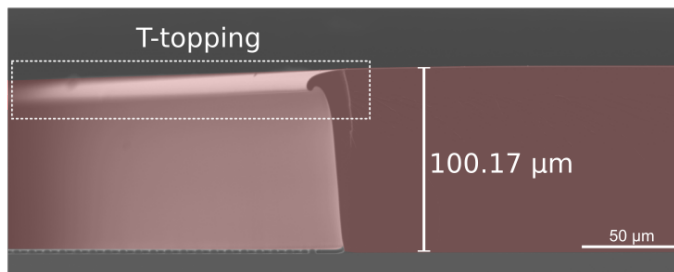


FIGURE 4.5: SEM image of an SU-8 2050 well structure (red). Images were obtained after sputter coating 3 nm of Pt.

4.1.3 SU-8 2050 on SU-8 2002

As SU-8 2002 and 2050 have a similar refractive index, alignment of both layers was problematic. In order to facilitate this process we first patterned Au alignment marks under the first layer (Figure 4.6).

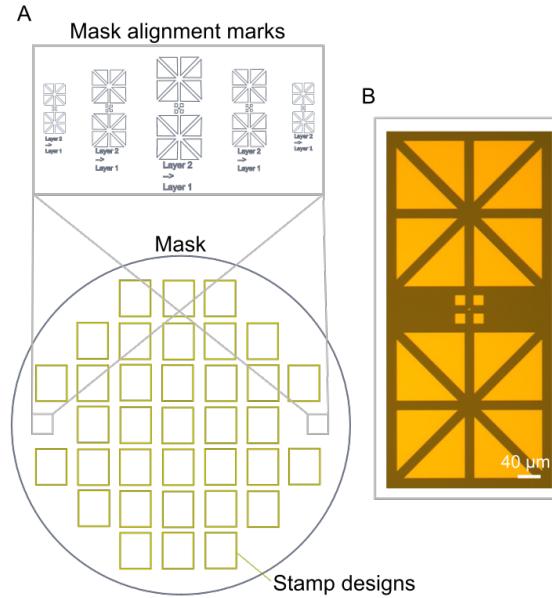


FIGURE 4.6: Gold alignment marks were patterned via a lift-off process on the left and right side of the wafer. In (A) the location on the mask is illustrated. A brightfield microscopy image of the smallest alignment marks patterned on the silicon wafer is shown in (B).

During processing, it became apparent that SU-8 2050 tends to delaminate from the underlying SU-8 2002, likely due to differences in the expansion coefficient between the two SU-8 layers, which induces stresses throughout the heating and cooling steps of the fabrication protocol (see Figure 4.7) [129, 106, 130]. Delamination is more apparent in the thicker SU-8 2050 layer than the thinner SU-8 2002, since the thicker the layer the higher the stresses [129, 106, 131]. To overcome this problem the stresses have to be reduced and/or the adhesion has to be enhanced. Three different strategies were applied.

Oxygen plasma treatment of the SU-8 2002 layer (1 min at 100W) made the surface more reactive, leading to stronger adhesion between both SU-8 layers, but still some delamination was observed [132].

Thermal ramping of all heating and cooling, this was done manually with a ramp of approximately 5-10 °C/s. Thermal ramping reduces induced stresses [129, 106, 131], but also here delamination was still observed.

Ti-prime adhesion layer on the SU-8 2002 in combination with thermal ramping. Using this strategy, the delamination of SU-8 2050 from the substrate was resolved.

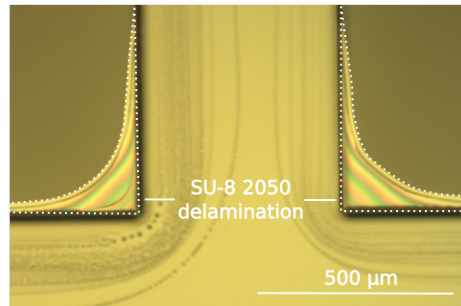


FIGURE 4.7: Delamination of SU-8 2050 well structures from the underlying SU-8 2002 substrate.

4.2 PDMS molding

In a first step, PDMS was molded on top of a master with only the first (thin) SU-8 layer. No fluid flow could be observed when water-based food coloring was added to one of the inlets (see Figure 4.8). The lack of fluid flow can be explained by the collapse of the well region between the inlet and the channels. This collapse is the result of the limited height ($2.3 \mu\text{m}$ in the case of a one-layer master) of the wells and elasticity of the PDMS. Additionally, some small circles are present on Figure 4.8, which are pillars designed to prevent collapse, but due to a too large interspacing they were not able to yield sufficient support to the PDMS.

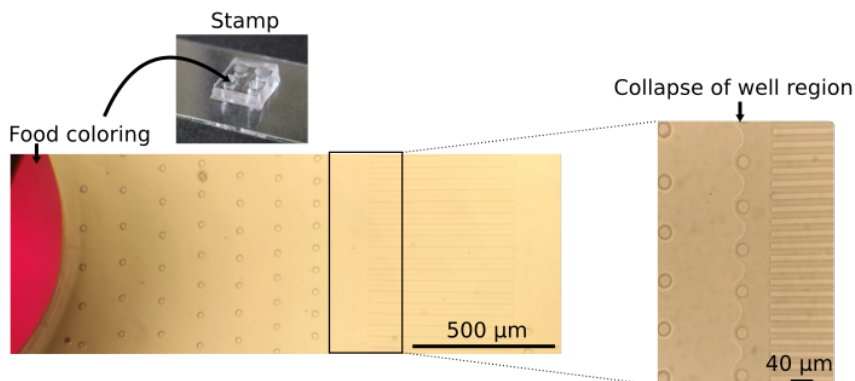


FIGURE 4.8: PDMS stamp produced with a one-layer master. No fluid flow was observed due to collapse of the well region. Inside the well region some circles are present, these were pillars designed to prevent the collapse of this region, but due to a too large interspacing they could not give enough support to the PDMS.

When applying PDMS to the two-layer (i.e. completed) master a PDMS stamp as in Figure 4.9 was obtained. On the SEM images of the cross-section (see Figure 4.10) the height of the well region was measured to be $98.88 \mu\text{m}$ and the region did not collapse, which fits within expectations. Upon addition of colored fluid (i.e. the water-based food coloring) to the left well region the fluid was transported to the right well region. To look at fluid flow inside the channels, the fluorescent dye fluoresceine was added and the channels were

4. RESULTS AND DISCUSSION

observed under a fluorescence microscope (Olympus IX71). In Table 4.4 an overview of all channel designs filled with fluorescent dye are visualized.

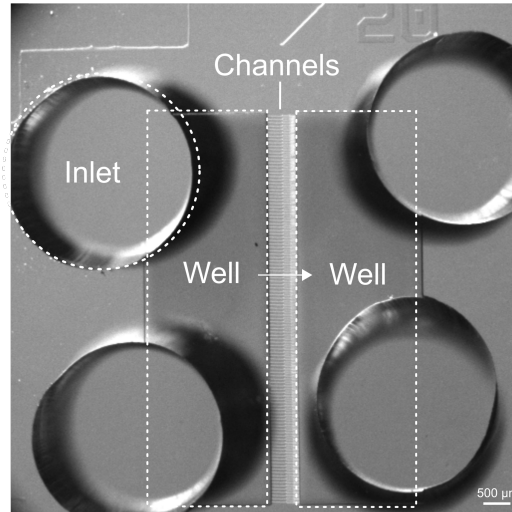


FIGURE 4.9: Brightfield image of the PDMS stamp made with a two-layer master. Fluid is pipetted inside the inlet which then flows via the channel region from the left to the right well.

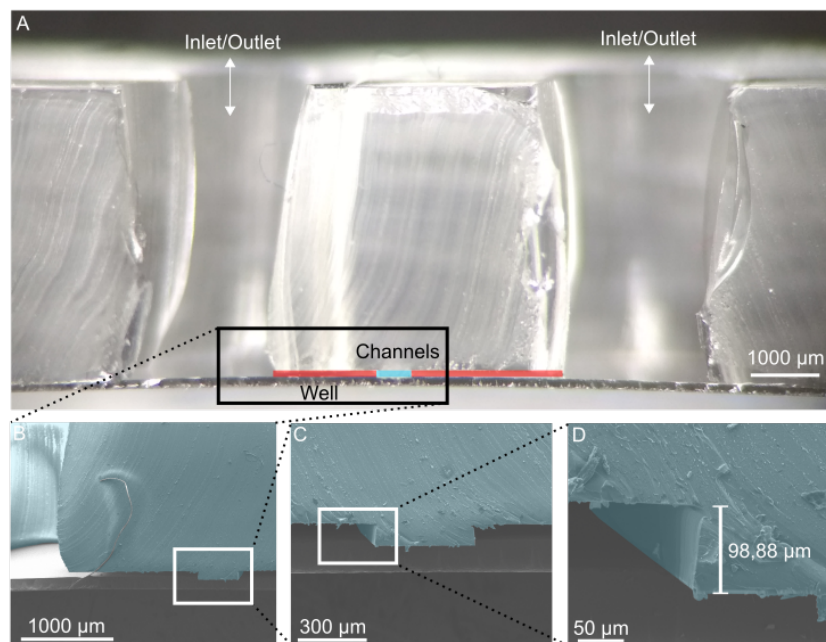


FIGURE 4.10: Stereoscopy (A) and SEM images (B, C and D) of the cross-section of a PDMS stamp. PDMS is colored in blue. SEM images obtained after sputter coating 3 nm of Pt.

It was found that all 25 different channel designs facilitated the passage of fluid. The barbs of design 6 were transferred to the PDMS despite the fact that these were not being fully resolved in the master. In Figure 4.11 some of the non-resolved features were imaged with SEM. Brief overview of missing/unresolved structural features:

- Channel design 10: Two smaller side peaks of $1\ \mu\text{m}$ width
- Channel design 13 and 22: Diamond structures
- Channel design 14 and 23: Diamond structures
- Channel design 15 and 24: Peaks of $2\ \mu\text{m}$ thick
- Channel design 16 and 25: Peaks of $1\ \mu\text{m}$ thick

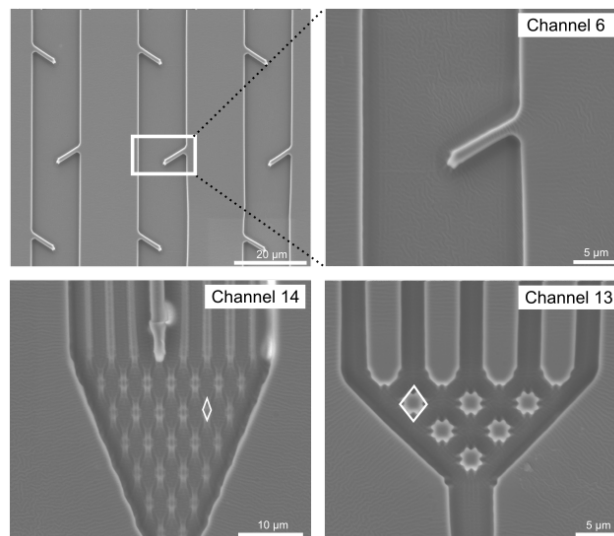
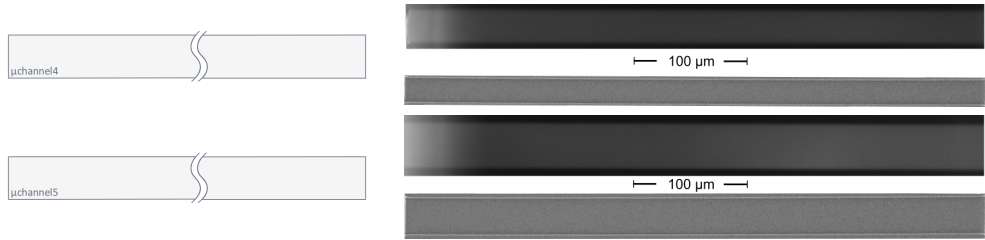


FIGURE 4.11: SEM images of smallest features on PDMS stamps. Features smaller than $3\ \mu\text{m}$ were not fully resolved. Images were obtained after sputter coating $3\ \text{nm}$ Pt.

TABLE 4.4: Fluorescence microscopy and SEM images. Fluorescence microscopy images were obtained after applying fluoresceïne to one of the wells. SEM images were obtained after sputter coating $3\ \text{nm}$ of Pt.

Design	Fluorescence microscopy and SEM images
Straight designs	

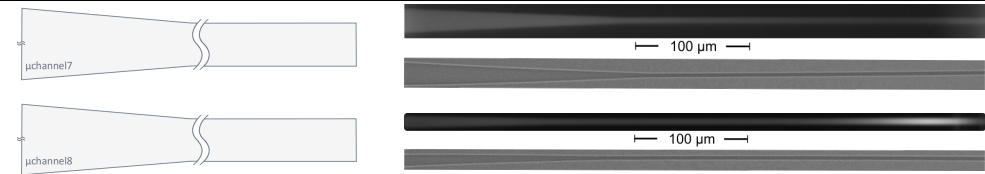
4. RESULTS AND DISCUSSION



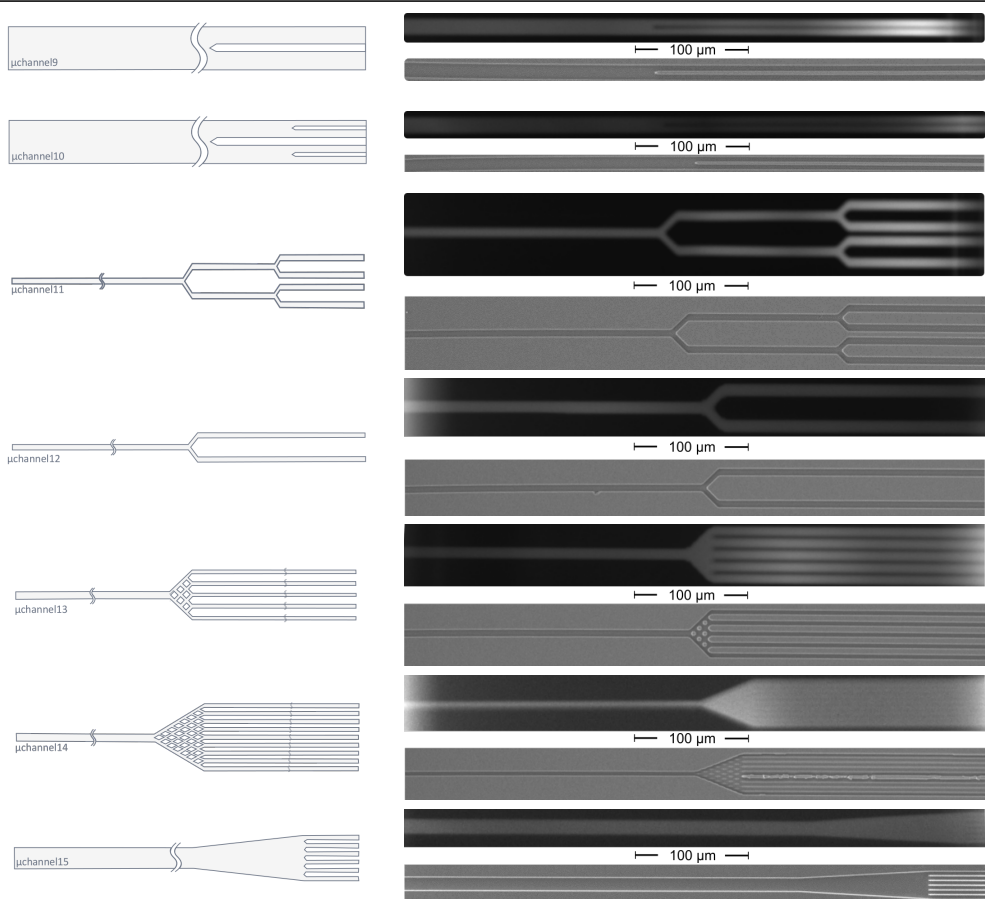
Barbed design

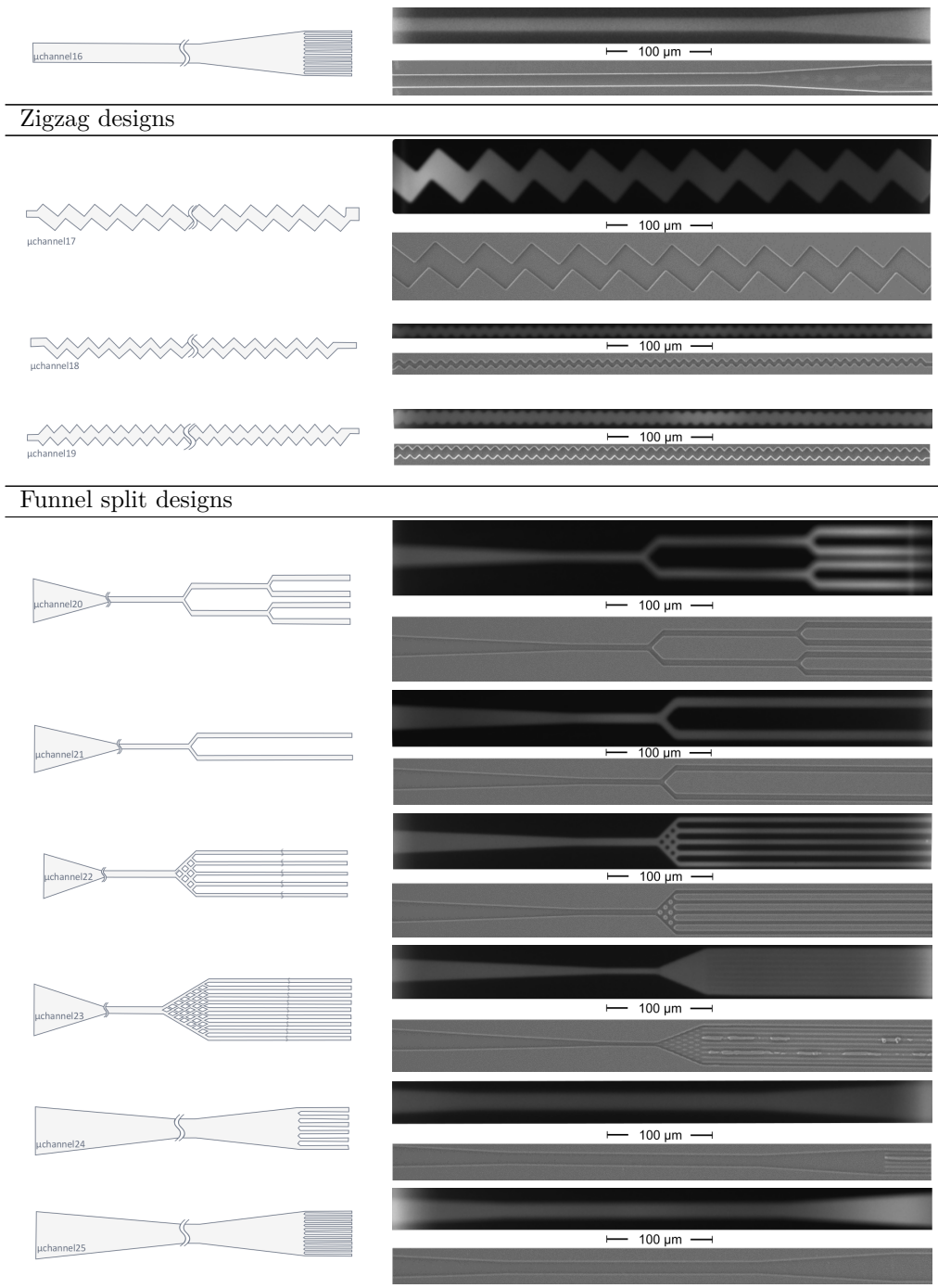


Funnel designs



Split designs





4.2.1 Time between bonding and filling

A wide variety of straight channels were designed with a width of $3\ \mu\text{m}$, $5\ \mu\text{m}$, $10\ \mu\text{m}$, $20\ \mu\text{m}$ or $30\ \mu\text{m}$. The channels were designed with different interspace widths which can be found in Table 3.1. It was hypothesized that the larger the interspace width, the larger the adherence to the substrate, and thus the smaller the probability would be that a channel fails (by forming, for example, a connection with a neighboring channel). A second factor influencing stamp performance is the time between bonding and filling of the stamp: during the oxygen plasma treatments, the PDMS becomes hydrophilic, enhancing capillary flow [116, 133, 132]. Over time the PDMS returns to its hydrophobic state, thus reducing stamp performance. To investigate the effect of interspace width and time between bonding and filling, different straight channel designs: 1, 2, 3, 4, 5, 31, 32, 33, 34 and 35 were compared with 0 min, 90 min and 180 min between bonding and filling with fluoresceine.

Of the stamps filled immediately after bonding, 97% (SD: 13%) of the channels contained fluid (see Table 4.5). At 90 min and 180 min, channels were respectively 15% (SD: 26%) and 13% (SD: 21%) of the time filled (see Figure 4.12). By applying Wilcoxon rang-sum tests a significant difference between 0 min & 90 min and 0 min & 180 min was found with p values of respectively $3.0 \cdot 10^{-11}$ and $6.6 \cdot 10^{-12}$. No significant difference between the data of 90 min & 180 min was observed (p value of 0.33). Kruskal-Wallis tests to determine differences between the various channels were performed for the 0 min, 90 min and 180 min data, p-values of respectively 0.22, 0.27 and 0.07 were obtained. These results indicate that there is no significant influence of channel or interspace width on channel filling.

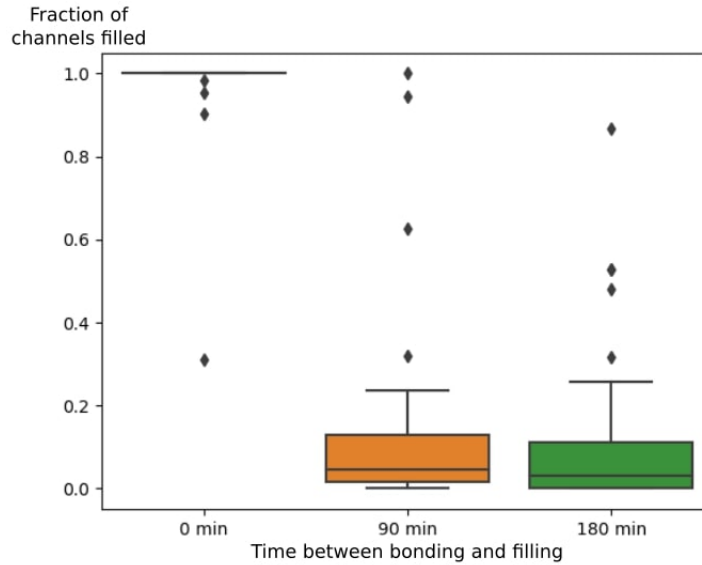


FIGURE 4.12: Influence of the time between the bonding of the PDMS stamp to the glass substrate and the filling of the stamp on the fraction of channels filled.

4.2. PDMS molding

	Type	Interspace width (μm)	0 min		90 min		180 min	
			Mean fraction filled	SD	Mean fraction filled	SD	Mean fraction filled	SD
5 μm , 20 μm and 30 μm channels	2	10	1.00	0.00	0.09	0.11	0.02	0.02
	4	20	1.00	0.00	0.45	0.45	0.38	0.42
	5	30	0.77	0.40	0.42	0.52	0.51	0.03
10 μm channels	3	10	1.00	0.00	0.25	0.33	0.07	0.06
	32	20	1.00	0.00	0.04	0.04	0.09	0.14
	34	40	1.00	0.00	0.02	0.02	0.01	0.02
3 μm channels	1	10	1.00	0.00	0.06	0.06	0.02	0.02
	31	20	1.00	0.00	0.07	0.10	0.12	0.17
	33	40	0.98	0.03	0.08	0.05	0.01	0.01
	35	100	0.96	0.05	0.01	0.01	0.03	0.04
Overall			0.97	0.13	0.15	0.26	0.13	0.21

TABLE 4.5: Fluoresceine was added to the inlet of a set of PDMS stamps with straight channels at 0 min, 90 min or 180 min. Every experiment was done in triplicate, mean and standard deviation were calculated.

The decrease in stamp performance could possibly be explained by a return of the PDMS to the hydrophobic state as described above. This can be due to diffusion of uncrosslinked, low molecular-weight polymer chains to the thermodynamically unstable surface, the reorientation of surface functional groups and the adsorption of organic contaminants present in the air [133, 134, 135, 136, 137, 138]. Since the channels need to be filled with fluid for cells to grow, it is important to fill them as soon as possible after the oxygen plasma treatment. Figure 4.13 and Figure 4.14 are examples of images obtained of stamps with and without fluoresceine inside their channels.

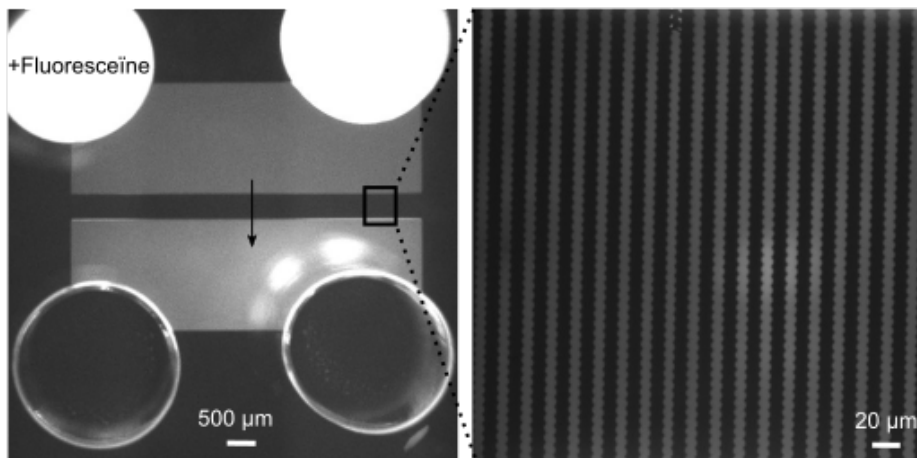


FIGURE 4.13: Fluoresceine was added to the inlet of a PDMS stamp directly after bonding. Fluorescence signal (Olympus IX71) could be observed in the channel and in the bottom well region.

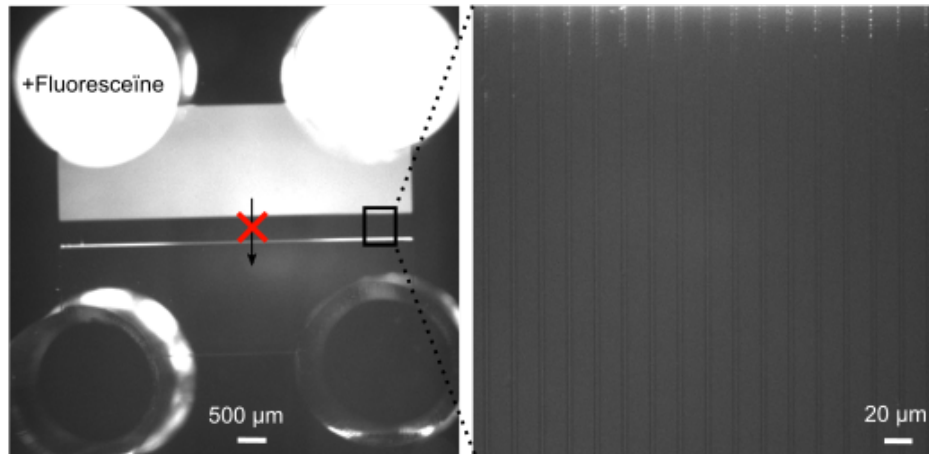


FIGURE 4.14: Fluoresceine was added to the inlet of a PDMS stamp 3 hours after bonding. Fluorescence signal (Olympus IX71) could not be observed in the channel or in the bottom well region.

4.2.2 Four inlets/outlets vs two inlets/outlets

Upon comparing the four inlets/outlets configurations (each 3 mm) with the two inlets/outlets configurations, it was observed that all nine stamps with two inlets/outlets contained an air bubble inside the inlet well, while none of the four inlets/outlets configurations contained air bubbles (see Figure 4.15). The air bubbles got trapped since they could not escape through the channels. Air bubbles should be avoided as they will impede cell growth. Future designs should therefore incorporate enough space to punch sufficient inlets/outlets for the escape of air. Here, an alternative method for avoiding air bubbles was used, i.e. by creating a larger inlet/outlet of 8 mm by punching several times with a 3 mm biopsy puncher. Using this method, no air bubbles were encountered in the wells.

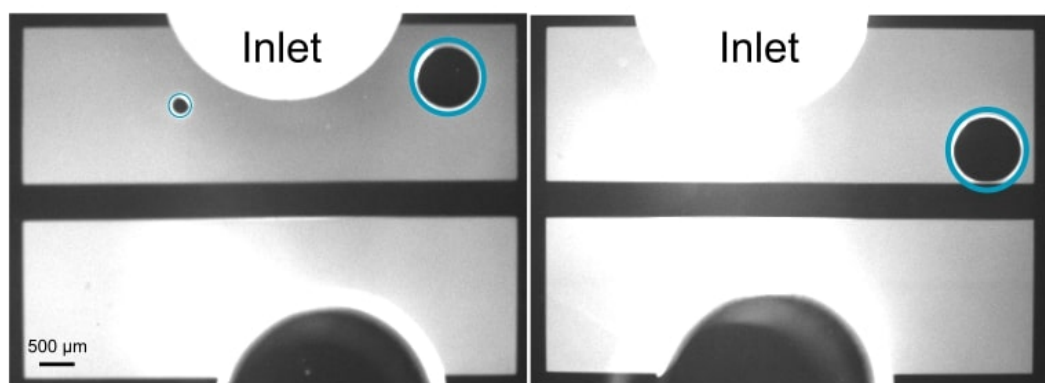


FIGURE 4.15: Air bubbles were observed in PDMS chips with only one inlet per well.

4.2.3 Bonding on chip

Oxygen plasma treated PDMS chips, were bonded to Synaptrode chips treated with and without oxygen plasma. We found that the PDMS adhered well to these chips, irrespective of the oxygen plasma treatment (see Figure 4.16).

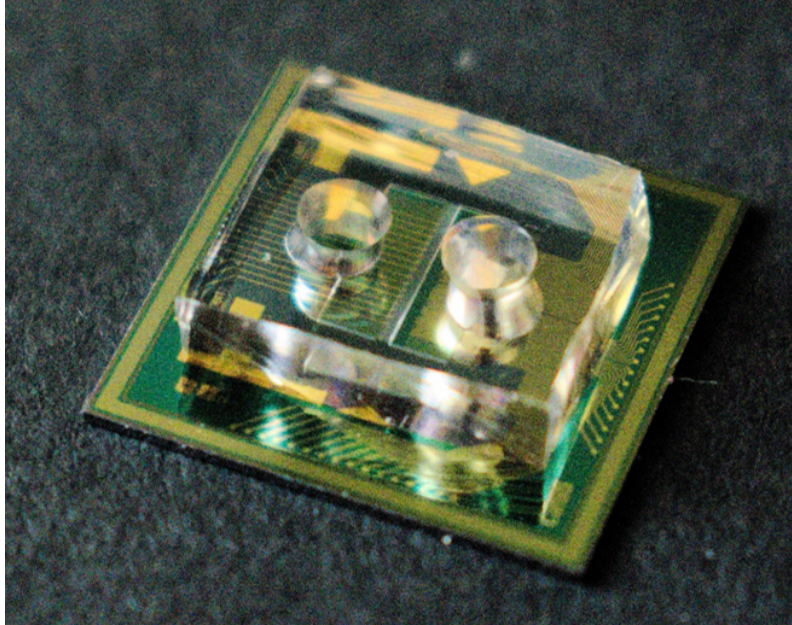


FIGURE 4.16: PDMS stamp bonded to Synaptrode chip.

4.3 Modeling

4.3.1 Mesh dependency study

In Figure 4.17 the influence of the mesh density on the results (average concentration in channel and well area) is visualized. A swept mesh with 12 442 elements was selected. A further increase in mesh density was found to produce a minimal change (less than $0.001 \cdot 10^{-4}$ mM) in the mean concentration of antibodies at 1800s (see Figure 4.17). This mesh density was used throughout the rest of this thesis.

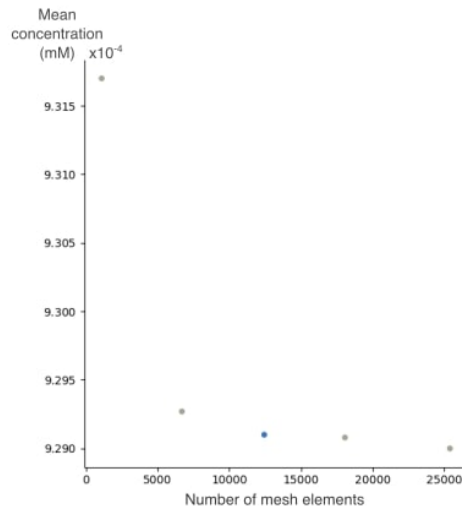


FIGURE 4.17: Mesh dependency study. The mean antibody concentration at 1800s modeled for different mesh densities. A mesh with 12 442 elements provided a good trade-off between accuracy and computational complexity.

4.3.2 Electrode functionalization

For the *in vitro* Synaptrode paradigm, electrodes are functionalized with synapse-inducing proteins at a location physically remote to the cell culture. The two-well design of the PDMS stamps accommodate for this prerequisite. Selective functionalization of the electrodes in one of the wells requires comparatively much lower concentration of protein in the opposite well. In-house functionalization protocols suggest incubation times of no longer than thirty minutes. To estimate diffusion of reagents from one well to the other through the connecting microchannels, biotin-PEG and average commercial antibodies were selected to model diffusion profiles. As the diffusion coefficient of molecules depends largely on their size, the selected molecules were chosen to represent the smallest and largest reagents involved in the Synaptrode functionalization protocol.

In Figure 4.18 the diffusion of the two selected molecules is visualized for different channel widths. Diffusion laws (equations (3.1) and (3.2)) predict that wider channels will lead to higher average concentrations at 1800s. In all cases, the concentration of the molecules in the opposite well at 1800s is at least three orders of magnitude smaller than the inlet concentration (see Table 4.6). More experiments will need to be performed to show whether these concentrations are low enough to avoid functionalization of the incorrect electrodes.

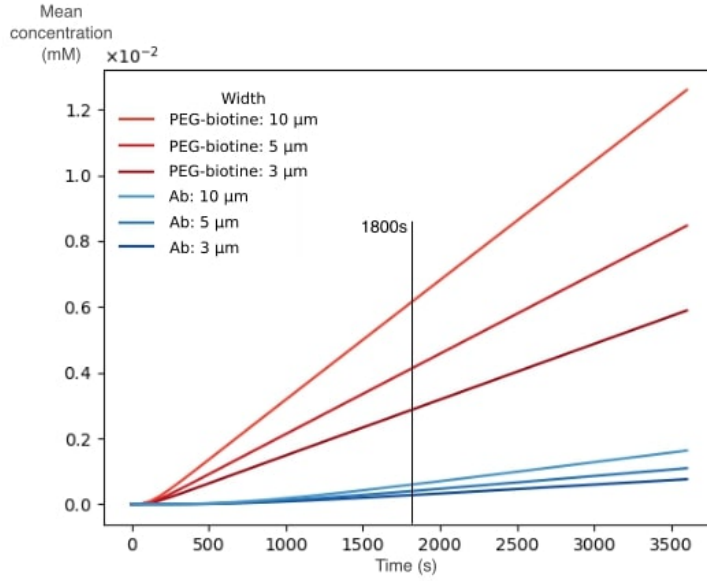


FIGURE 4.18: Diffusion of the smallest (PEG-biotine) and largest (antibody) molecules to the other well region through different channel types during the functionalization process.

Molecule	Width (μm)	C_n at 1800s (mM)
PEG-biotine	10	$6.1 \cdot 10^{-3}$
PEG-Biotine	5	$4.1 \cdot 10^{-3}$
PEG-Biotine	3	$2.8 \cdot 10^{-3}$
Ab	10	$5.9 \cdot 10^{-4}$
Ab	5	$3.9 \cdot 10^{-4}$
Ab	3	$2.7 \cdot 10^{-4}$

TABLE 4.6: Concentration in the opposite well region at 1800s for different molecules and different channel widths.

In Figure 4.19 the diffusion of both modeled molecules in channels with different lengths (100 to 500 μm) and a width of 3 μm is visualized. As can be expected from the Fickian diffusion theory (equations (3.1) and (3.2)), the longer the channel the longer it will take for the wells to reach their final concentration. In all cases, the concentration at 1800s remained two orders of magnitude lower than the final concentration (see Table 4.7). Whether this is low enough for avoiding functionalization of the incorrect electrodes should be demonstrated in future experiments. On the current mask all channels have a length of 500 μm , thus in order to test these shorter channels the design of a new photomask is required.

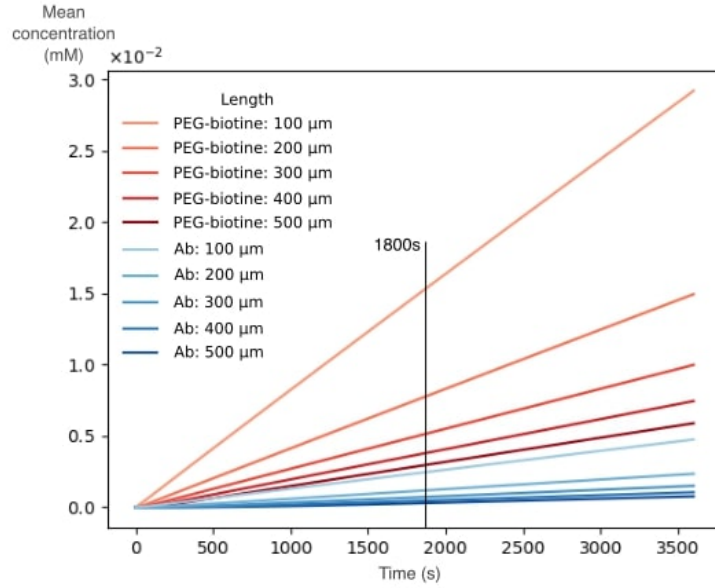


FIGURE 4.19: Effect of channel length on the diffusion process of the smallest (PEG-biotine) and the largest (antibody) molecules during electrode functionalization.

Molecule	Length (μm)	C_n at 1800s (mM)
PEG-biotine	100	$1.5 \cdot 10^{-2}$
PEG-Biotine	200	$7.5 \cdot 10^{-3}$
PEG-Biotine	300	$4.9 \cdot 10^{-3}$
PEG-biotine	400	$3.6 \cdot 10^{-3}$
PEG-Biotine	500	$2.8 \cdot 10^{-3}$
Ab	100	$2.4 \cdot 10^{-3}$
Ab	200	$1.1 \cdot 10^{-3}$
Ab	300	$6.8 \cdot 10^{-4}$
Ab	400	$4.4 \cdot 10^{-4}$
Ab	500	$2.7 \cdot 10^{-4}$

TABLE 4.7: Concentration in the opposite well region at 1800s for different molecules and different channel lengths, for a $3 \mu\text{m}$ wide channel.

In the subsequent model the effect of larger well regions (as a result of inlet/outlet punching) and fluid flow due to a hydrostatic pressure difference was modeled. In the case of zero pressure difference, the mean concentration in the well region (after half an hour) remains four orders of magnitude lower than the final concentration. In a second case, a pressure difference of 0.979 Pa resulted in a concentration seven orders of magnitude lower than the final concentration (for antibodies even 22 orders of magnitude). As a result, the well are virtually isolated.

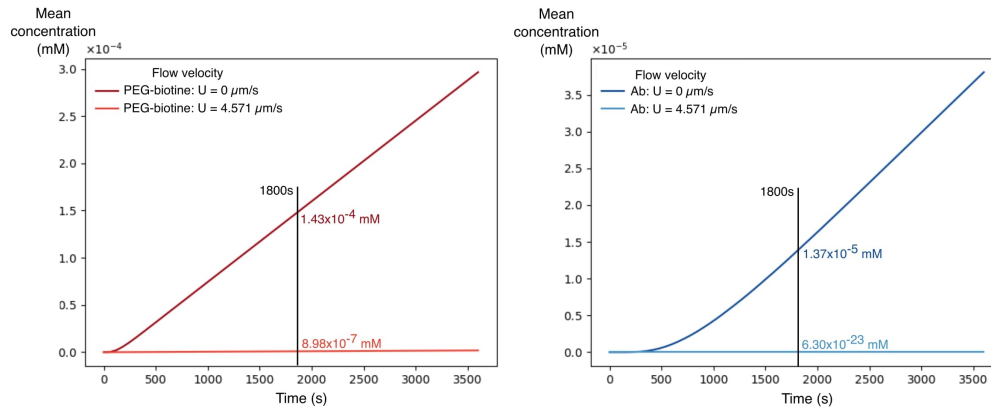


FIGURE 4.20: Effect of a larger well region ($2000 \mu\text{m}$ high) due to inlet/outlet punching and hydrostatic pressure difference (0.979 Pa) on the diffusion of antibodies and PEG-biotine. U is the flow velocity in the channel due to a pressure difference working against the diffusion.

In this and all previous models a whole range of assumptions were applied. Examples are Poiseuille flow, no interactions between molecules and channel walls, constant pressure difference, and no flow inside the well area. Validation will, however, be necessary. In future experiments this could be performed by adding a fluorophore to one well and looking at the evolution of fluorescence intensity in the opposite well. These results could then be compared to a diffusion model made in COMSOL Multiphysics where the diffusion constant of the fluorophore is used. Next, in a second experiment the functionalization could be performed. The amount of functionalization of the electrodes in the opposite well could be quantified by binding an antibody connected to a fluorophore and utilization of fluorescence microscopy.

4.3.3 Immuno staining

In Figure 4.21 it can be seen that all channels reach 95% of their final concentration after approximately 1320s. As can be expected from the Fickian diffusion laws ((3.1) and (3.2)), the longer the channel the longer it will take for the channel to reach its final concentration. It can be concluded that upon use of $500 \mu\text{m}$ the immunostaining steps should take at least 1320 s. As this is the case in the current protocol, no influence of the channels in the staining process is expected. For further channel designs even longer channels could be chosen.

4. RESULTS AND DISCUSSION

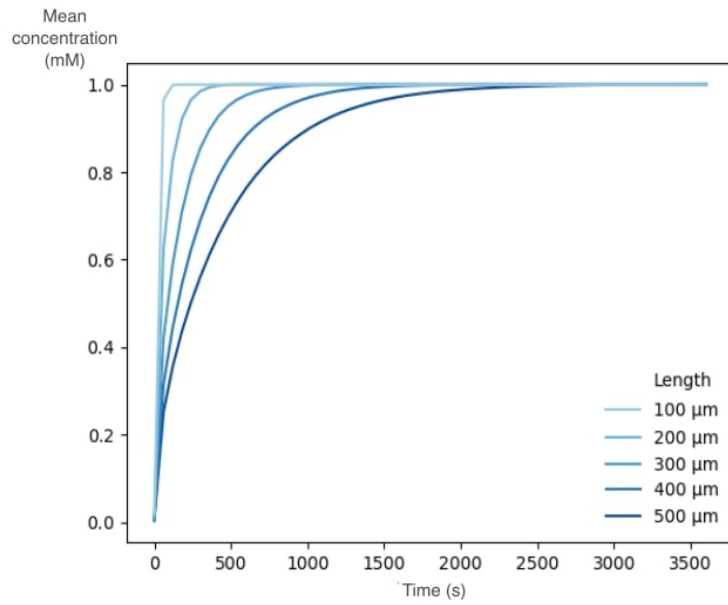


FIGURE 4.21: Diffusion of antibodies through different channel types during the immunostaining process.

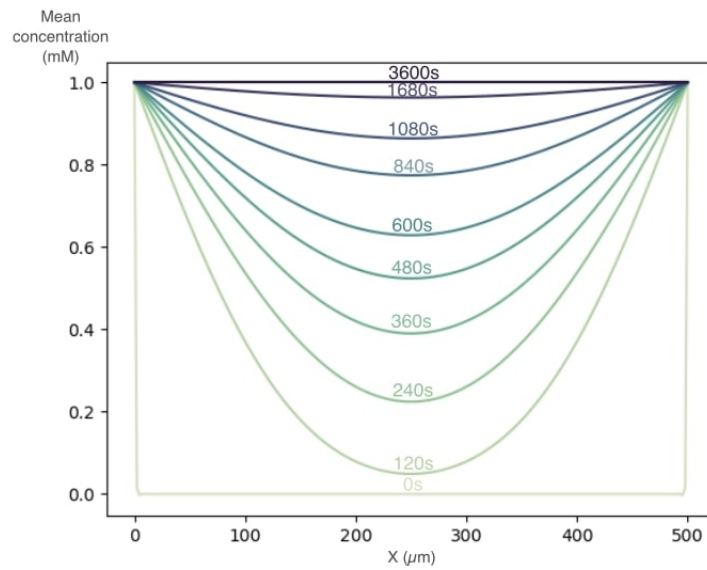


FIGURE 4.22: Evolution of concentration profile during the immunostaining process in a 500 μm channel.

4.4 Groove etching

In Table 4.8 an overview of all the different grooves etched into silicon is given. All different designs with features larger than $3\ \mu\text{m}$ could be transferred. Smaller features are not fully resolved (see Figure 4.23 and Figure 4.24).

- Channel design 10: Two smaller side peaks of $1\ \mu\text{m}$ width
- Channel design 13 and 22: Diamond structures
- Channel design 14 and 23: Diamond structures
- Channel design 15 and 24: Peaks of $2\ \mu\text{m}$ thick
- Channel design 16 and 25: Peaks of $1\ \mu\text{m}$ thick

The resolution is slightly better compared to that of the SU-8 patterns. The $1\ \mu\text{m}$ peaks in design 16 were, for example, partially resolved in the grooves but non-existent in the SU-8 patterns. The square structures of design 13 were less rounded in the etched patterns than in the SU-8 structures. The better resolution of the etched patterns could be the result of thinner resist films used in the etching procedure compared to the SU-8. Thinner resist layers typically show less variations in thickness and straighter slopes [139].

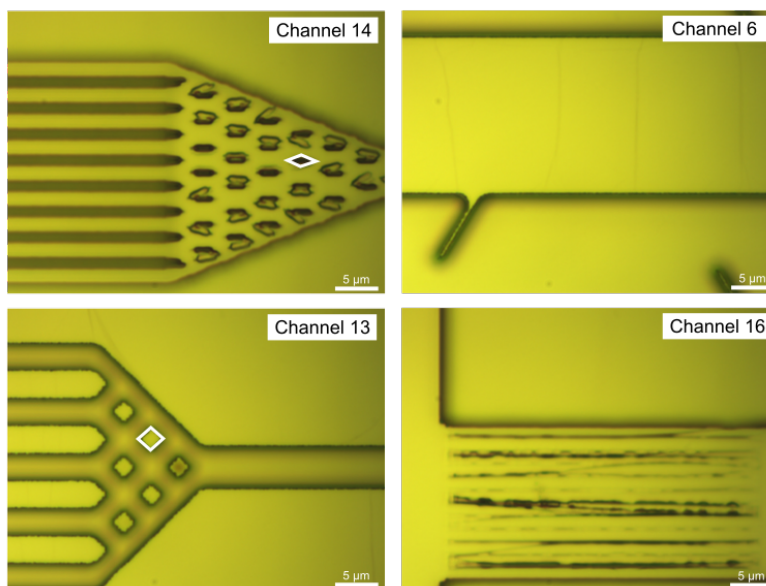


FIGURE 4.23: Brightfield images of the smallest features of Si etched grooves. Features smaller than $3\ \mu\text{m}$ were not fully resolved.

4. RESULTS AND DISCUSSION

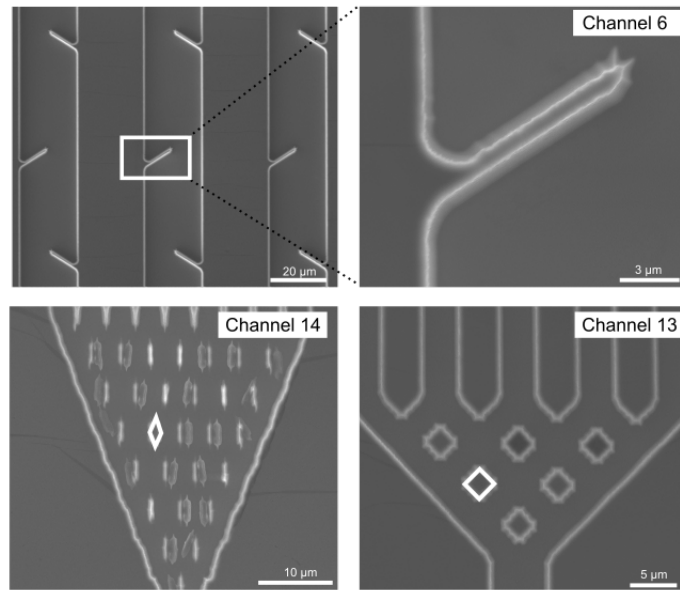



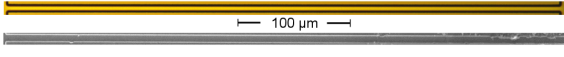



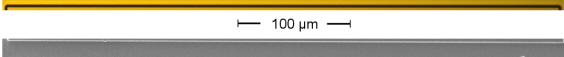

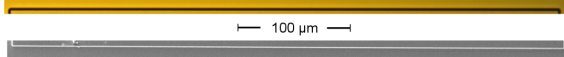

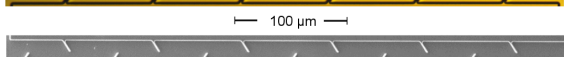
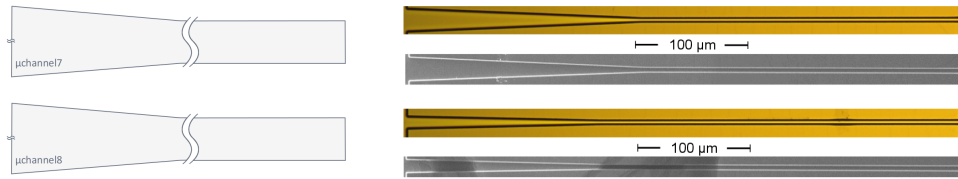


FIGURE 4.24: SEM images of the smallest features of Si etched grooves. Features smaller than $3 \mu\text{m}$ were not fully resolved.

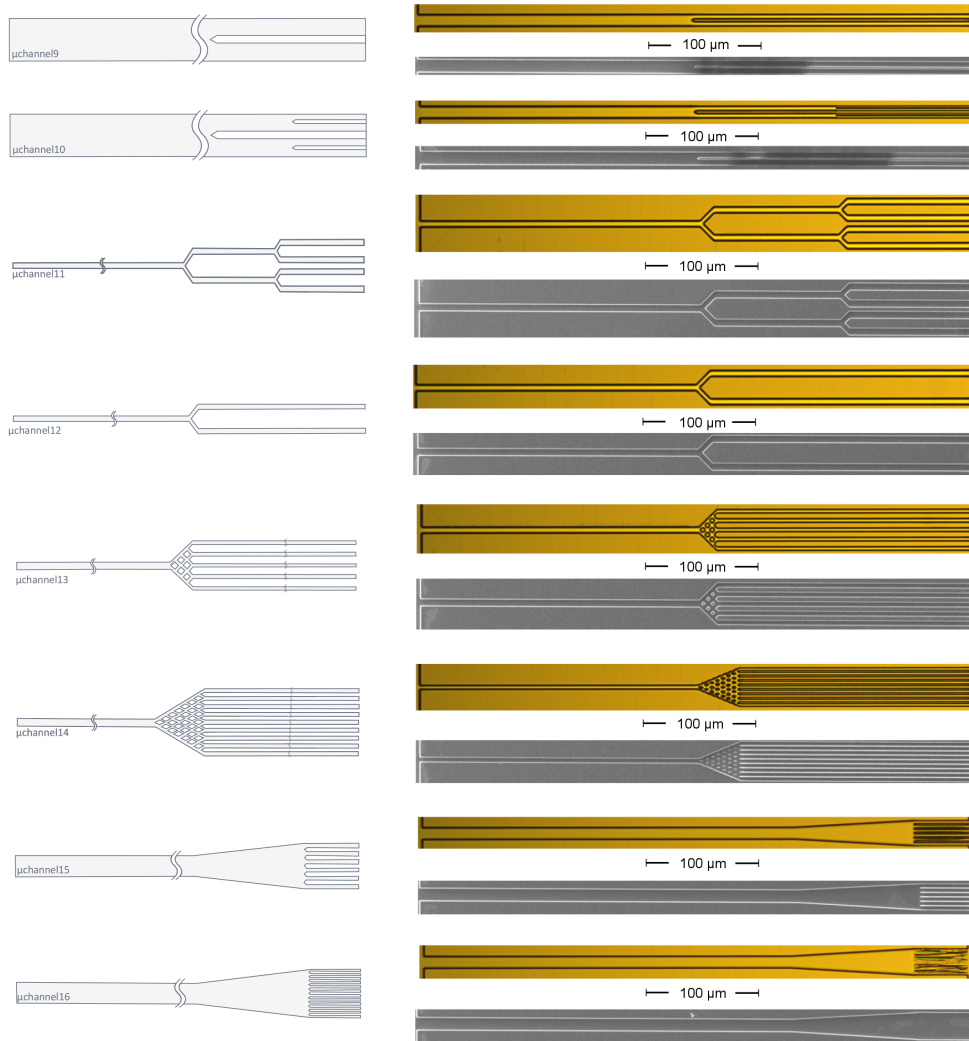
TABLE 4.8: Brightfield and SEM images of different groove designs.

Design	Brightfield and SEM
Straight designs	
	
	
	
	
	
Barbed design	
	

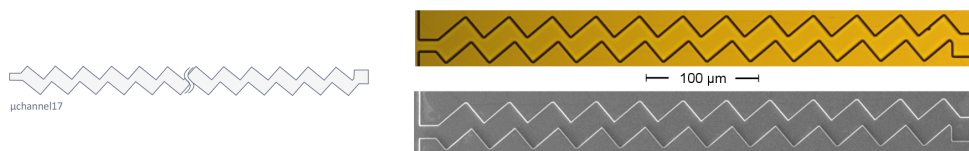
Funnel designs



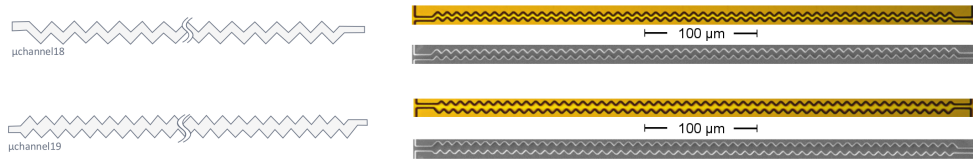
Split designs



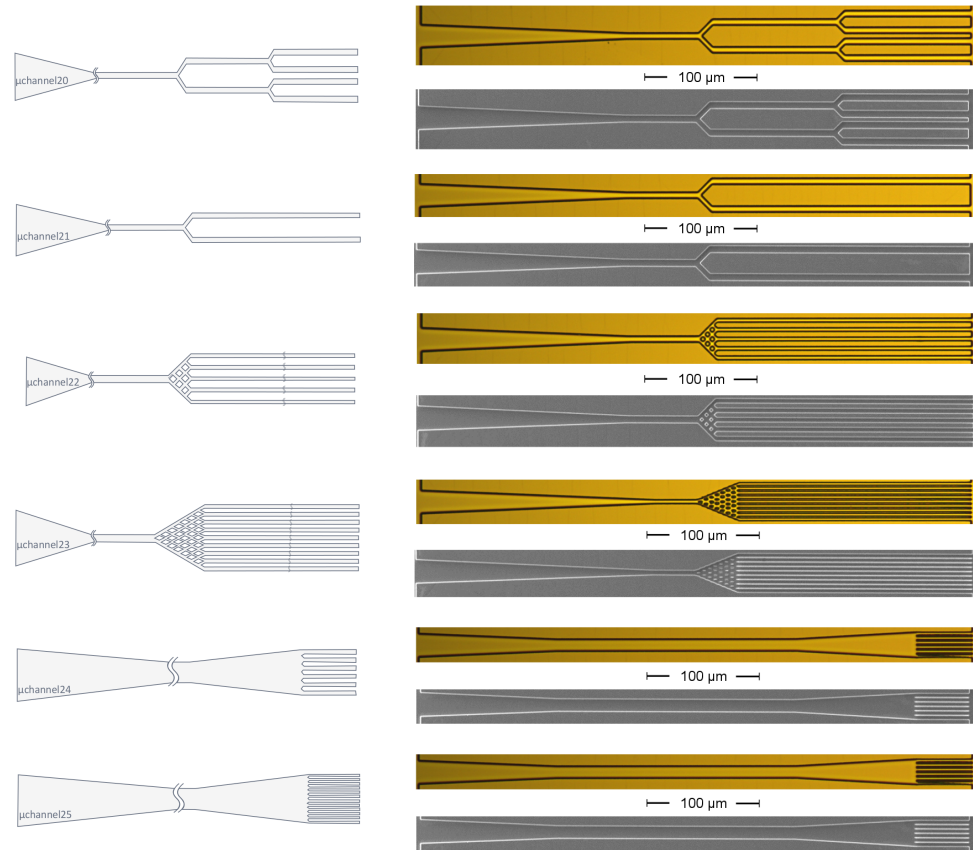
Zigzag designs



4. RESULTS AND DISCUSSION



Funnel split designs



In Table 4.9 the depths of the channels measured with a stylus profilometer (Dektak XT) used in subsequent cell experiments are summarized. Each channel type was produced in triplicate and 10 channels were measured per unit. With the applied protocol grooves with a depth of $2.96 \pm 0.06 \mu\text{m}$ can be fabricated.

Channel type		Mean(μm)	SD(μm)
2	A	2.90	0.05
	B	2.95	0.04
	C	2.97	0.08
	Total(2)	2.94	0.07
5	A	2.980	0.003
	B	2.96	0.01
	C	2.95	0.02
	Total(5)	2.96	0.02
11	A	3.0	0.1
	B	2.99	0.04
	C	2.92	0.06
	Total(11)	2.98	0.08
Total(2,5 and 11)		2.96	0.06

TABLE 4.9: Profilometry measurements of etched grooves (types 2, 5 and 11). Every type was produced in triplicate (A, B and C), on each the height of 10 different channels was measured.

4.5 Cell growth

The first three cultures suffered from a lack of cell medium due to evaporation. After every failure the following measures were subsequently taken to reduce this evaporation and the effects of it: check the humidity regulation system in the incubator, surround the PDMS stamp with DI water and replacement of medium every two days to avoid a too high ion concentration and replenish the nutrients.

The three subsequent cell cultures suffered bacterial contamination. This could be the result of insufficient sterilization prior to cell seeding, but since other non-related experiments suffered in the same way, it was assumed to be more of a structural problem in the cell-lab, the source has not yet been identified and the search had to be paused due to the Corona crisis.

Upon softening of the measures taken to prevent the spread of the Corona virus, some of the cell experiments were reinitiated. The impact of the Corona crisis and some of the final results are described below.

4.6 Impact of the Corona crisis

Cell experiments had to be paused due to the Corona crisis. The following section is a combination of hypothetical experiments that were initially planned and some final results of experiments that in the end were performed.

4.6.1 Channels

Every time new hippocampal neurons are extracted from mice, stamps 2, 5 and 11 will be seeded with $\pm 50\,000$ cells per well. Channels need a higher cell density compared to the grooves to assure a sufficient amount of cells close to the channels. Additionally, a PDMS insert will be bonded to a glass slide which will be seeded as a control (see Figure 4.25). Experiments will be performed until three successful samples are obtained for every channel type. Stamps 2, 5 and 11 were chosen since they are all fully resolved. Secondly, by comparing stamp 2 with 5 the effect of entrance width on neurite capture can be investigated. Lastly, with stamp 11 the ability of a channel splitting structures for splitting fasciculating axons can be compared with normal straight channels. Later on, other channel types could be examined, for example 17, 18 or 19, to examine the effect of zigzag structures, or stamp 6 to examine the effect of barbs inside the channels.

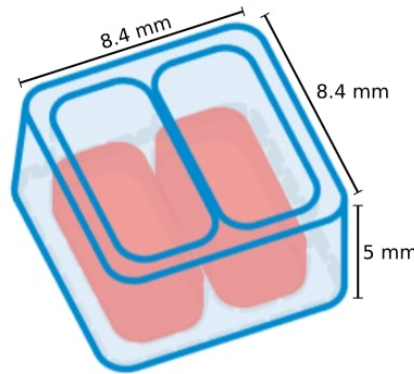


FIGURE 4.25: PDMS insert from [140] can be bonded to a glass slide and seeded with cells as a control.

Throughout the experiment cells can be monitored with a brightfield inverted microscope (Olympus IX71) and a live cell imaging fluorescent dye such as calcein-AM (calcein-acetoxymethyl) imaged with an epifluorescence inverted microscope (Olympus IX71). Calcein-AM is lipid soluble and can pass the lipid membrane. Inside the cell calcein-AM is converted by intracellular esterases to a molecule with a bright green fluorescence. These molecules will be retained by the cell as long as the cell is alive [35, 141]. Every two days the cells will be visualized with both techniques, a special heating plate will be employed that can be fitted on the microscope to keep the cells at 37°C during imaging. From the obtained images the progress of the neurites in the channels can be plotted (see Figure 4.26 for an example of a hypothetical graph). This graph could later be used to estimate neurite growth on a chip and determine when to start electrophysiology measurements, since imaging is obstructed by the silicon die.

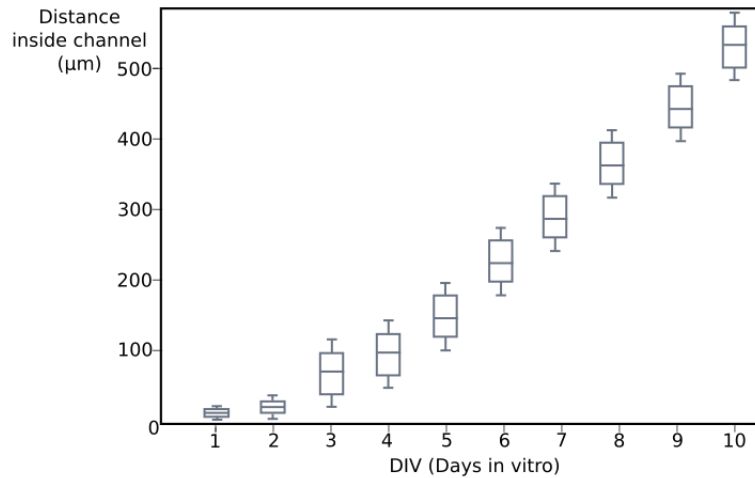


FIGURE 4.26: Theoretical graph of the progress of neurites inside microchannels that could possibly be obtained by life cell imaging.

At the end of the experiments (10 DIV) cells will be fixed and permeated after which they will be stained with antibodies for Tau (for the visualization of axons) and MAP2 (for the visualization of dendrites), the nucleus can be visualized with DAPI.

Tau: A protein associated with microtubules. The protein is preferentially expressed in axons making it a good candidate for axon visualization by immunostaining [84, 85, 41, 38, 142].

MAP2: A microtubule associated protein that is more abundant in dendrites. When visualizing MAP2 with immunostaining, soma/dendrites can be distinguished from the axons [85, 77, 38, 11].

DAPI (4',6-diamidino-2-phenylindole): A widely used dye for visualization of dsDNA. DAPI binds to the minor groove of AT-rich sequences. Since the DNA of a cell is located in the nucleus, DAPI can be employed to visualize individual cell nuclei. An alternative for this are Hoechst dyes [37, 41, 143].

Protocol for staining:

- Fixate with 4% PFA and 4% sucrose in PBS for 15 min at RT
- Rinse 2 times in PBS (5 min)
- Permeabilize with 0.25% Triton X100 in PBS for 5 min at 4 °C. Wash twice in PBS
- Add 20% BSA as blocking agent in PBS for 1 h at RT
- Incubate the primary Abs overnight at 4 °C (for more details on the specific types of antibodies used see Appendix A)
- Wash with PBS 3 times at RT

4. RESULTS AND DISCUSSION

- Incubate with secondary Abs in PBS for 1 h at RT (for more details on the specific types of antibodies used see Appendix A)
- Wash 3 times with PBS at RT
- Store in PBS at 4 °C till visualization

Several metrics can be determined to compare PDMS channels. The following metrics can be calculated by analyzing the images of the immunostained samples (with ImageJ) imaged with a (confocal) fluorescence microscope (Nikon C2 Eclipse Ni-E).

A first metric is the percentage of channels that contain neurites reaching the other well area (Channels filled: CF), influenced by the entrance width. Channels 2, 5 and 11 have an entrance width of 5 μm , 30 μm and 5 μm , respectively. Channel 5 is thus expected to have a higher CF. With this metric the effect of entrance width can be evaluated.

A second metric is the number of channels containing neurites (NCF). The NCF is both determined by channel width and the amount of channels on a stamp. Stamps 2, 5 and 11 have respectively 426, 106 and 320 channels on their stamp and an entrance width of 5 μm , 30 μm , and 5 μm . It is expected that the NCF will increase with channel width and with the number of channels on the stamp.

A last metric is the amount of channels with single neurites at their outlet (SN). It is expected that stamp 11 will have the highest SN due to its splitting ability.

Dependant on the experiments performed with the Synaptrode chip, one of the metrics can become more important. In a first experiment it could be important to only look at synapse formation. In such a case it could be critical to have as many neurites on the other side as possible. To boost the probability of synapse formation, the NFC metric can then be used to determine the best stamp. In more advanced experiments where single-axon activity is investigated it could be important to have a single neurite forming a synapse at the electrode. For such a case SN is a more appropriate metric.

Upon start of the Corona exit strategy *in vitro* cell cultures were reinitiated with the stamps left from previous experiments. Stamps with channel design 11, 21 and 25 were seeded with mouse hippocampal cells and fixated after respectively 5, 7 and 11 DIV. The fixated samples were stained with anti-Tau and anti-MAP2 antibodies (using the protocol described above). No more contamination issues were observed. In Figure 4.27 it can be noticed that axons were able to grow through the produced microchannels. Additionally, these experiments suggest a minimum of 6 to 7 DIV for the axons to reach the other side, which is comparable to the data described in literature [39, 78, 40]. Another phenomenon that could be observed is the tendency of the axons to follow the edges of the channel (edge guidance) as described by Holloway and coworkers [86]. A relatively large amount of aspecifically bound antibody is present, which could be explained by the difficulty experienced in washing due to the small volumes involved, suggesting that bigger well areas would improve image quality. At last it can be concluded that it is possible to stain axons in small microchannels as was modeled in COMSOL Multiphysics.

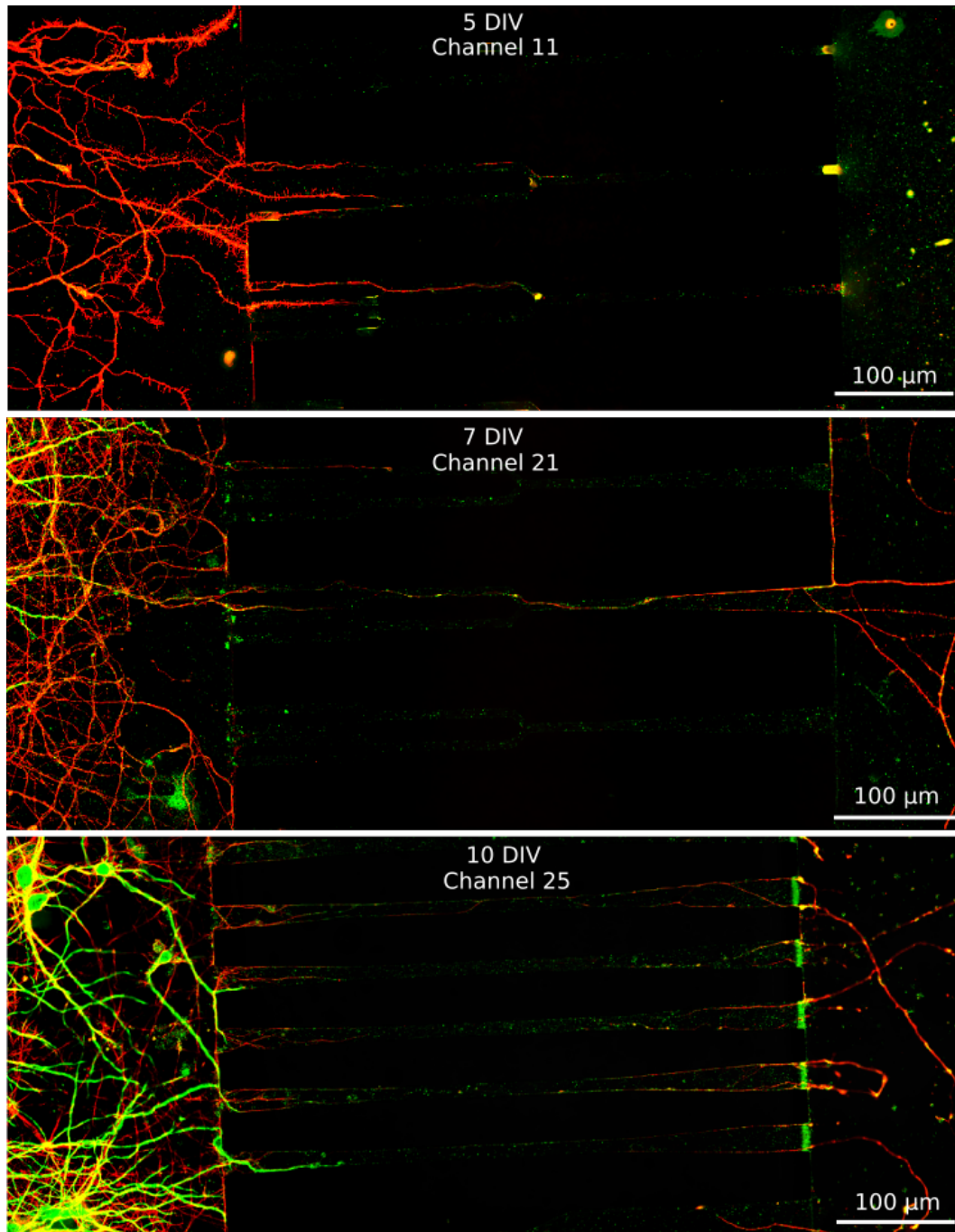


FIGURE 4.27: *In vitro* cell cultures in stamps with channel design 11, 21 and 25 fixated and stained for Tau (red) and MAP2 (green) after respectively 5, 7 and 10 DIV.

4.6.2 Grooves

Grooves 2, 5 and 11 (tested in triplicate) will be treated similarly to their PDMS counterparts, after fabrication they will be sterilized and coated with laminin and PLO. Subsequent cell seeding will be executed with a PDMS insert (from [140]) which will be removed upon further incubation in neural basal medium + B27 for 10 DIV. No visualization can be done during the growth process. After the 10 DIV the cells will be fixed, permeated and stained in the same fashion as the cells inside the PDMS stamps. Cells will be visualized with a Nikon spinning disk microscope.

4.6.3 Comparison stamps/channels

Grooves will be compared to microchannels by calculating the distance travelled in the direction parallel to the channels/grooves (d) for the 100 farthest grown neurons (see Figure 4.28). The d metric can be calculated in ImageJ based on the immunostained samples imaged with a confocal microscope. It is expected that the d metric will be on average higher for the channels compared to the grooves. Since neurites on grooves can grow from one to the other groove, slowing down their progress in the desired direction.

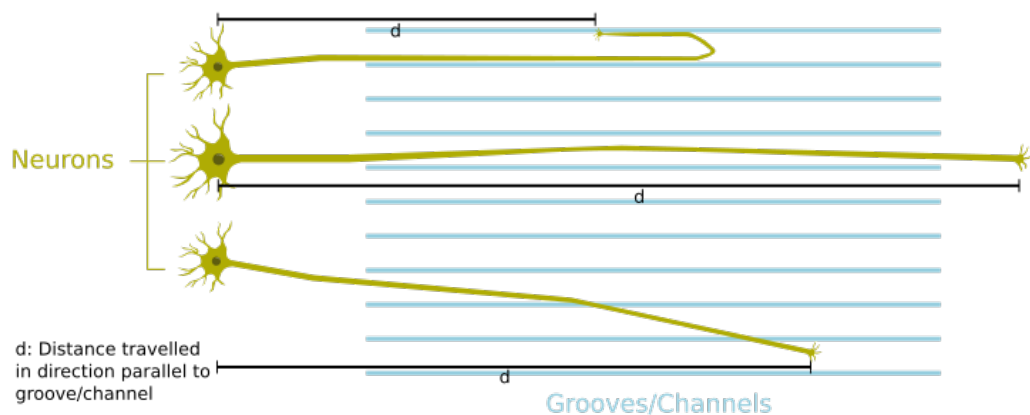


FIGURE 4.28: Illustration of metric d (distance travelled in direction parallel to groove/channel) for comparing grooves with channels.

4.7 New stamp designs

3 new masks were designed based on the knowledge gathered in this thesis (see Figure 4.29).

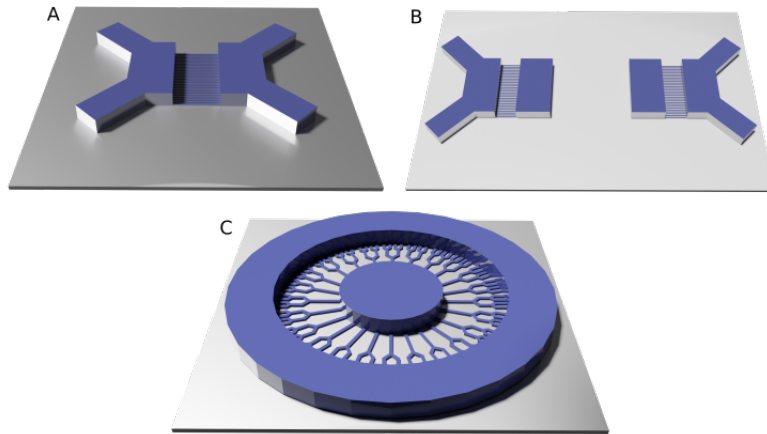


FIGURE 4.29: 3D models of three new possible master designs. Design 1 (A), design 2 (B) and design 3 (C).

4.7.1 New design 1

In Figure 4.30 the two masks for a new design are represented. In this first new design the area of the well region is decreased to reduce the stresses during master fabrication. Additionally, for each well there is room to punch two inlets/outlets.

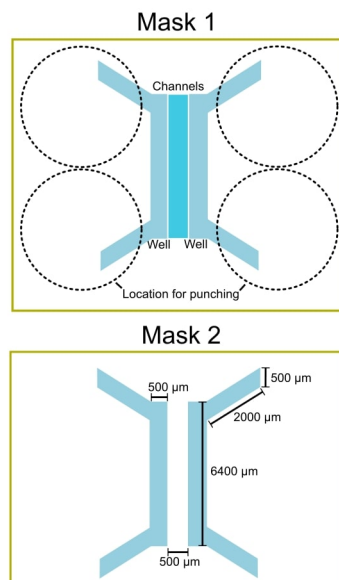


FIGURE 4.30: Schematic preview of masks for a first new stamp design.

4.7.2 New design 2

In Figure 4.31 the two masks for a second new design are represented. In this second new design two channel regions are present. By punching the inlet/outlet at the right location these regions can possibly be isolated from each other facilitating two experiments on one chip. Or the stamp can be punched in such a way that a fluid connection is created. Upon plating cells at both outer sides chemoattractive species will be exchanged enhancing growth and directionality of both compartments.

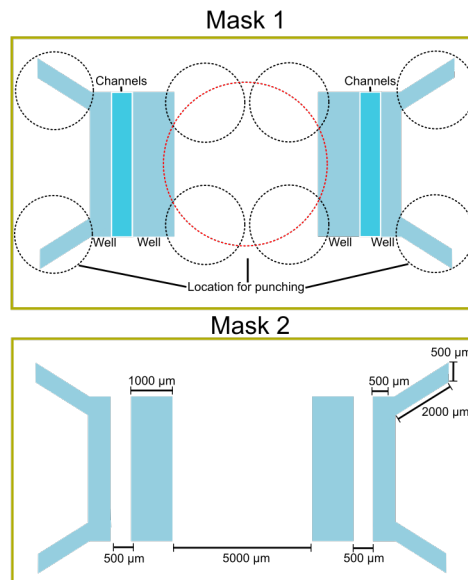


FIGURE 4.31: Schematic preview of masks for a second new stamp design. Channel regions can either be isolated by punching inlets/outlets in the black dotted regions or channel regions can be connected by punching an inlet/outlet in the red dotted region.

4.7.3 New design 3

In Figure 4.31 the two masks for a third new design are represented. This circular design can be combined with different channel types. In this case a splitting design can make use of the larger circumference of the outer ring compared to the inner ring. This design can fit within a cell culture ring.

The channel length in the three new designs can possibly be reduced to shorten the time needed for the separation of synapse and soma decreasing the risk of denatured synaptogenic proteins although also decreasing synapse soma separation. For designs two and three a new type of Synaptrode chip will have to be fabricated.

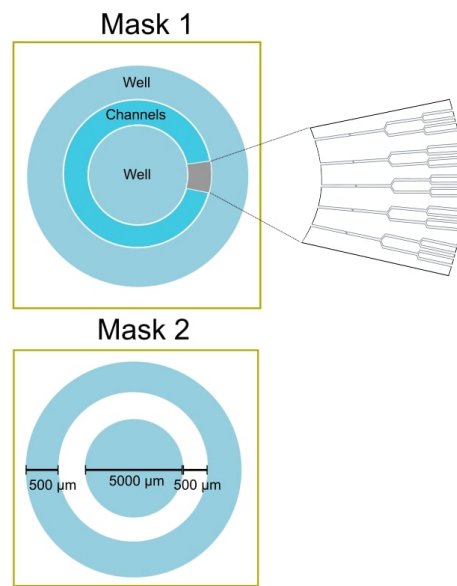


FIGURE 4.32: Schematic preview of masks for a third new stamp design.

4.8 Summary

A wide variety of different channels and grooves were obtained with features as small as $3 \mu\text{m}$. All models created in COMSOL Multiphysics suggest that the fabricated channels enable selective functionalization of one array of electrodes and do not interfere with the immunostaining process. Cell experiments were started, but as a result of the Corona crisis these had to be stopped prematurely. Hypothetical future experiments were presented together with some of the preliminary results. At last three new stamp designs were proposed.

Chapter 5

Conclusion

In light of the Synaptrode project, the goal of this thesis was to design, fabricate and test various microchannel/microgroove structures to enable the separation of neuronal synapses from the soma in order to allow future measurements of single synapses.

Both RIE and PDMS/SU-8 soft lithography techniques allowed the creation of patterns with feature sizes down to $3\ \mu\text{m}$. The resolution of RIE was slightly better due to the utilization of thinner resist layers. The resolution could possibly be further enhanced upon using a quartz photolithography mask with higher resolution.

A two-layer SU-8 master was produced. A first layer of $2.29 \pm 0.04\ \mu\text{m}$ with the channel designs and a second layer, the well region with a thickness of $120 \pm 20\ \mu\text{m}$. To avoid delamination a Ti prime layer was introduced before each spinning step. This was essential for the adhesion of the second layer which has a tendency to delaminate due to a buildup of stresses as a result of the large surface area and many heating/cooling steps. In the two-layer lithography procedure it was essential to pattern gold alignment marks to enable later alignment of layer one and layer two.

SU-8 patterns were converted to PDMS via a molding procedure. All different types of channels facilitated fluid transport, no influence of channel or interspace width was observed. The greater thickness of the second layer (with wells) was essential for avoiding the collapse of this region. Oxygen plasma-treated PDMS stamps can be bonded to the silicon oxide surface of the Synaptrode chips, the Synaptrode chips do not need an oxygen plasma treatment for this. To enable filling of the channels they have to be filled directly after bonding. Already after one and a half hours channel filling was limited. Probably due to a return to the hydrophobic state [134, 133, 132]. Stamp design should incorporate enough/large inlets/outlets to enable the escape of air bubbles.

From the diffusion models it can be concluded that the PDMS microchannels in combination with a pressure difference result in virtually isolated well regions. This phenomenon can possibly be of use when selectively functionalizing the electrodes in one of the two well regions. These models need to be further validated.

The fabricated microchannels facilitate guided axon growth *in vitro*. A separation of $500\ \mu\text{m}$ is achieved after 6-7 DIV. Future experiments will have to determine which channels design is most suited for the Synaptrode project.

5. CONCLUSION

Grooves with a depth of $2.96 \pm 0.06 \mu\text{m}$ can be created with the help of a O_2/SF_6 plasma for 7 min. The effectiveness of grooves to guide axon growth remains untested.

In Table 5.1 and Table 5.2 the pros and cons of PDMS microchannels and silicon etched grooves are displayed. It can be concluded that for this specific application, separation of synapse and soma, the PDMS microchannels provides the best solution as long as a micromanipulator is present for aligning the PDMS stamps with the chip.

Pros	Cons
Selective functionalization of electrodes possible due to partial fluidic isolation.	Stamps need to be aligned with help of micromanipulator.
Neurites are fully confined, they cannot cross to neighboring guiding structures.	Protocol for master production needs to be optimized for every design.
Can be bonded directly on chip, with no damage done to the chip.	High density of neurons needed to get cells close to channel region.
Extra diffusional gradient of chemoattractant/chemorepellant can be applied by adding these guiding molecules selectively to one well.	
Once the protocol for master production is established, stamps can be created fast in large amounts.	
Amplification of signal when measured inside channel.	

TABLE 5.1: Pros and cons of using PDMS microchannels for synapse soma separation.

Pros	Cons
Grooves can be created with higher resolution than PDMS stamps.	For selective functionalization of electrodes an extra step with a PDMS insert needs to be introduced.
Easy alignment with chip via standard photolithography alignment tools.	Grooves interfere with growth of vertical CNT electrodes.
Lower density of neurons can be used.	Possible damage of chip during etching.
	No full confinement of growing neurites.
	Difficult to combine with chemical gradient.

TABLE 5.2: Pros and cons of using silicon grooves for synapse soma separation.

5.1 Future work

Future work will now need to focus on the cell experiments using the channels and grooves fabricated in this thesis. More specifically, more work has to be done regarding the visualization of the neurons growing inside the channels, and on thoroughly comparing the various channel designs. Future data will then shed new light on the creation of possible novel stamps and channel designs. Another important step is thorough testing of the Synaptrode chip, including selective functionalization of the electrodes and, ultimately, the electrophysiological measurements of neurons.

Appendices

Appendix A

Tools and Chemicals

An overview of all tools and chemicals used in this thesis.

A.1 Tools

In this section extra information on some of the tools is given.

Mask aligner: Karl suss MA6 [\[144\]](#)

- Exposure time: protocol dependant
- Alignment gap: $30\ \mu\text{m}$
- Exposure type: hard or soft, protocol dependant
- HC wait: 3s
- WEC Type: Cont
- WEC offset: off
- Exposure(J): $56\ \text{mW}/\text{cm}^2$
- Exposure time: $t = \text{desired exposure (mJ}/\text{cm}^2)/J$
- Peak wavelength: UV-400
- Max resolution: $0.6\ \mu\text{m}$

Stylus Profiler: Dektak XT [\[145\]](#)

- Vertical resolution: 0.1 nm max
- Step height repeatability: 0.4 nm
- Tip size: $2\ \mu\text{m}$

Oxygen plasma oven for PDMS bonding: Plasma cleaner PDC-002-CE

- 3 settings: Low, Medium and High. High is used in all protocols
- Maximum RF power: 30 W
- Gass: air

A.2 Chemicals

In this section an overview is given of the chemicals used in the various protocols.

A.2.1 Master fabrication

From Kayaku advanced materials:

- SU-8 2002 [124]
- SU-8 2050 [146]
- SU-8 developer

Standard IMEC cleanroom chemicals:

- IPA (KMG Ultra Pure Chemicals SAS)
- Aceton (KMG Ultra Pure Chemicals SAS)
- Microstrip (KMG Ultra Pure Chemicals SAS)
- OPD5262 (KMG Ultra Pure Chemicals SAS)
- Ti-prime (MERCK)
- Isopropanol (KMG Ultra Pure Chemicals SAS)
- IX845 (KMG Ultra Pure Chemicals SAS)

Si-wafer (4" Polishing wafer):

- Type: P/Boron
- Crystal axis: <100>
- Resistivity: 10-20 ohm-cm
- Diameter: 99.5-100.5 mm
- Thickness: 500-550 μm

A.2.2 PDMS molding

PDMS: Polydimethylsiloxane

- Sylgard 184 (Mavom nv)[147]

Glass slides: Corning microscope slides (Merck [148])

Fluoresceine (ThermoFisher [149]):

- Excitation max: 490nm
- Emission max: 525 nm
- Concentration: 0.1 mg/ml

Water-based food coloring:

- Bought in local supermarket
- Prepared in dionised water (1:10) purified with a Milli-Q 50 ultrapure water system (Millipore, Belgium)

A.2.3 Cell experiments

Chemicals from Merck:

- PLO
- Laminin
- Borate buffer
- DMEM + horse serum
- Neurobasal + B27
- PFA
- PBS
- Triton X100
- BSA
- DAPI

Primary antibodies:

- Chicken anti-MAP2 (Jackson ImmunoResearch)
- Mouse anti-Tau (Abcam)

A. TOOLS AND CHEMICALS

Secondary antibodies:

- Anti-chicken (408) (Invitrogen)
- Donkey anti-mouse (555) (Invitrogen)

Appendix B

Protocols

An overview of all protocols used in this thesis.

B.1 Gold alignment marks

- Dehydration bake wafer for 5 min at 190 °C
- Spin coat a layer of IX845G positive resist at 4000 rpm (30s, acceleration 1333 rpm/s)
- Bake for 1 min at 120 °C
- Expose wafer to 134.4 mJ/cm^2 (Karl Suss MA6, hard contact)
- Develop for 1 min in OPD5262
- Rinse with H_2O and dry with N_2
- Postbake for 30s at 120 °C
- Sputtercoat 10 nm Ti and 40 nm Au on the wafer
- Lift-off the Ti/Au in hot microstrip for 5 hours at 80 °C
- Transfer wafer to ultrasonic bath for 5 min
- Clean with IPA and dry with N_2
- Inspect for defects

B.2 SU-8 protocol: SU-8 2002 (1.6 μm) start

- Apply SU-8 to the wafer by spin coating, 5s at 500 rpm (100 rpms/s) and 30s at 2000 rpm (300 rpm/s)
- Wait 15 minutes for wafer relaxation
- Prebake 2 min at 65 °C and 2 min at 95 °C. (Gradual T transition by holding wafer 10s above hotplate)
- Expose wafer to 4x184.8 mJ/cm^2 (Karl Suss MA6, hard contact)

B. PROTOCOLS

- Post-illumination bake wafer with resist on hotplate 2 min at 65 °C and 2.5 min at 95 °C (Gradual T transition by holding wafer 10s above hotplate)
- Develop illuminated wafer in SU-8 developer 5 min in first beaker and 5 min in second beaker
- Take wafer out beaker and rinse with SU-8 developer, dry with N₂
- Spin dry with SU-8 developer and IPA. 30s at 2000 rpm
- Hard bake wafer with resist on hotplate 10 min at 130 °C
- Place wafer in hot IPA and dry with N₂
- Optional clean with O₂ plasma, can give too much adhesion when PDMS is poured on top
- Inspect defects

B.3 SU-8 protocol: SU-8 2002 (2.3 μm) without Ti-prime

- Apply SU-8 to the wafer by spin coating, 5s at 500 rpm (acceleration 100 rpms/s) and 30 s at 1000 rpm (acceleration 300 rpm/s)
- Wait 15 min for wafer relaxation
- Prebake 2 min at 65 °C and 2 min at 95 °C (Gradual T transition by holding wafer 10 s above hotplate)
- Expose wafer to 3x89.6 mJ/cm² (Karl Suss MA6, hard contact)
- Post-illumination bake wafer on hotplate 2 min at 65 °C and 2.5 min at 95 °C (Gradual T transition by holding wafer 10s above hotplate)
- Develop illuminated wafer for 1 min in SU-8 developer
- Take wafer out beaker and rinse with SU-8 developer, dry with N₂
- Hard bake wafer on hotplate 10 min at 130 °C
- Place wafer in hot IPA and dry with N₂
- Inspect defects

B.4 SU-8 protocol: SU-8 2002 (2.3 μm) with Ti-prime layer

- Dehydrate the wafer by baking for 5 min at 190 °C
- Spin coat Ti-prime at 2000 rpm (30s, acceleration 667 rpm/s)
- Bake the wafer for 5 min at 190 °C
- Apply SU-8 to the wafer by spin coating, 5s at 500 rpm (acceleration 100 rpms/s) and 30s at 1000 rpm (acceleration 300 rpm/s)

- Wait 15 min for wafer relaxation
- Prebake 2 min at 65 °C and 2 min at 95 °C. (Gradual T transition by holding wafer 10 s above hotplate)
- Expose wafer to 89.6 mJ/cm^2 (Karl Suss MA6, hard contact)
- Post-illumination bake wafer on hotplate for 2 min at 65 °C and 2.5 min at 95°C (Gradual T transition by holding wafer 10s above hotplate)
- Develop illuminated wafer for 1 min in SU-8 developer
- Take wafer out beaker and rinse with SU-8 developer, dry with N₂
- Hard bake wafer on hotplate 10 min at 130 °C
- Place wafer in hot IPA and dry with N₂
- Inspect for defects and measure thickness with stylus profilometer (Dektak XT)

B.5 SU-8 protocol: SU-8 2050 start

- Apply SU-8 to the wafer by spin coating, 5s at 500 rpm (acceleration 100 rpms/s) and 30s at 1000 rpm (acceleration 300 rpm/s)
- Edge bead removal
- Wait 15 min for wafer relaxation
- Prebake 7 min at 65°C and 35 min at 95 °C. (Gradual T transition by holding wafer 10s above hotplate)
- Expose wafer to 392 mJ/cm^2 (Karl Suss MA6)
- Post-illumination bake wafer with resist on hotplate 5 min at 65 °C and 15 min at 95 °C (Gradual T transition by holding wafer 10 s above hotplate)
- Develop illuminated wafer 20 min in SU-8 developer
- Take wafer out beaker and rinse with SU-8 developer, dry with N₂
- Hard bake wafer with resist on hotplate 10 min at 130 °C
- Place wafer in hot IPA and dry with N₂
- Inspect defects

B.6 SU-8 protocol: SU-8 2050 (120 μm) with Ti prime layer

- Dehydrate the wafer by baking for 5 min at 190 °C
- Spin coat Ti-prime at 2000 rpm (30s, acceleration 667 rpm/s)
- Bake the wafer for 5 min at 190 °C
- Apply SU-8 to the wafer by spin coating, 5s at 500 rpm (acceleration 100 rpms/s) and 30s at 1500 rpm (acceleration 300 rpm/s)

B. PROTOCOLS

- Wait 60 minutes for wafer relaxation
- Heat wafer on a hotplate from room temperature till 95 °C over 20 min. Keep the wafer for 20 min at 190 °C and then eventually let the wafer gradually cool down for 30 min
- Expose wafer to $8 \times 184.8 \text{ mJ/cm}^2$ with 14s between every cycle (Karl Suss MA6, soft contact)
- Post-illumination bake wafer on hotplate by gradually increasing the temperature to 95 °C in 20 min followed by 10 min at 95 °C and a gradual decrease in temperature over 30 min
- Develop illuminated wafer for 20 min
- Take wafer out beaker, rinse with SU-8 developer and IPA, dry with N₂
- Hard bake wafer on hotplate by gradually increasing the temperature to 130 °C in 20 min, bake for 5 min at 130 °C and gradually let the wafer cool again to room temperature
- Place wafer in hot IPA and dry with N₂
- Inspect for defects and measure thickness with stylus profilometer (Dektak XT)

B.7 Ti-prime

- Dehydrate the wafer by baking for 5 min at 190 °C
- Spin coat Ti-prime at 2000 rpm (acceleration 667 rpm/s)
- Bake the wafer for 5 min at 190 °C

B.8 PDMS molding

The PDMS used in the following protocol is Sylgard 184

A Preparing PDMS (Sylgard 184)

- Weigh 50 mg (for 4" wafer) of PDMS
- Add curing agent (10% off the mass of PDMS), mix the solutions well
- De-gas the solution by applying negative pressure, wait around 20 min until no more bubbles are visible and a clear PDMS solution appears
- Use a container to put the wafer inside, can be a petridish or an aluminium crucible.
- Pour the degassed PDMS carefully on the mold

B curing PDMS

- Cure the PDMS in an oven at 50 °C for 2 h

C PDMS bonding

- Remove container and peel PDMS off the SU-8 mold
- Puncture inlet and outlet holes (3 mm biopsy puncher, Miltex)
- Use the plasma cleaner to activate the surface of stamp and glass slide/chip. 2 min at high level (RF power: 30 W, Pressure: 0.380 Torr). Transforming the Si-CH₃ of the PDMS to a Si-OH. When in contact with the same functional groups strong and permanent Si-O-Si links are formed
- Bring glass/chip in contact and squeeze gently to ensure contact without closing the channels

B.9 Mask cleaning

- Wash in ultrasonic hot acetone at 75 °C for 15 min
- Wash in dirty IPA for 5 min
- Rinse with water
- Wash in clean IPA for 5 min
- Wash in isopropanol for 5 min
- Dry with N₂

B.10 Groove etching

- Spin coat IX845 at 4000 rpm for 30s (acceleration 1333 rpm/s)
- Bake 60s at 120 °C
- Expose wafer to 341.6 mJ/cm² (Karl Suss MA6, hard contact)
- Develop 1 min in OPD5262
- Bake 10 s at 120 °C
- Rinse with H₂O and dry with N₂
- Expose to O₂/SF₆ plasma for 7 min (RF: 60 W, ICP: 100 W, O₂: 10 sccm, SF₆: 40 sccm) with the Oxford plasmalab 100
- Submerge in acetone until all resist is removed
- Rinse with H₂O and dry with N₂
- Clean in hot IPA for 30 s and dry with N₂

B.11 Channel/groove preparation and cell culture

- Sterilise the channels/grooves by exposing the samples to UV radiation for 60 min
- Coat overnight with 0.1 mg/ml PLO and 0.01 mg/ml laminin in sterile borate buffer 1x

B. PROTOCOLS

- Seed approximately 25 000 for the grooves and 50 000 for the channels, E19 embryonic mouse hippocampal cells inside the well regions with DMEM + horse serum
- Use Neurobasal + B27 as subsequent growth medium, replace half of the medium every two days

B.12 Cell fixation and staining

- Fixate with 4% PFA and 4% sucrose in PBS for 15 min at RT
- Rinse 2 times in PBS (5 min)
- Permeabilize with 0.25% Triton X100 in PBS for 5 min at 4 °C. Wash 2 times in PBS (5 min)
- Add 20% BSA as blocking agent in PBS for 1 h at RT
- Incubate the primary Abs overnight at 4 °C
- Wash with PBS 3 times at RT (5 min)
- Incubate with secondary Abs in PBS for 1 h at RT
- Wash 3 times with PBS at RT (5 min)
- Store in PBS at 4 °C till visualization

Appendix C

Supplementary Data

All data collected during this thesis

C.1 SU-8 2002 and SU-8 2050

SU-8 2002 at 1000 rpm: Thickness was measured (Dektak XT) in north, east, south, west and middle of the wafer. 10 channels were measured each time. The mean and standard deviation was calculated.

	1	2	3	4	5	6	7	8	9	10	Mean	SD
N (μm)	2.3070	2.3079	2.3082	2.3079	2.3092	2.3086	2.3110	2.3109	2.3125	2.3111	2.309	0.002
E (μm)	2.3096	2.3088	2.3074	2.3074	2.3130	2.3088	2.3067	2.3070	2.3099	2.3106	2.309	0.002
S (μm)	2.2500	2.2416	2.2378	2.2312	2.2278	2.2186	2.2144	2.2054	2.1975	2.1922	2.22	0.02
W (μm)	2.3129	2.3095	2.3108	2.3087	2.3080	2.3075	2.3029	2.3083	2.3040	2.3064	2.308	0.003
Mid (μm)	2.3080	2.3048	2.3023	2.2998	2.2978	2.2948	2.2946	2.2918	2.2896	2.2851	2.297	0.007
										Overall (μm)	2.29	0.04

TABLE C.1: Thickness measurements (Dektak XT) of patterned SU8-2002 spincoated at 1000 rpm. 10 channels were measured at each location.

SU-8 2050 spincoated at 1500 rpm and 1000 rpm. Thickness is measured in north, east, south, west and middle of the wafer.

	1500 rpm	1000 rpm
N (μm)	105.792	164.405
E (μm)	124.285	173.772
S (μm)	157.634	268.175
W (μm)	95.785	210.437
Mid (μm)	103.992	149.490
Mean (μm)	$1.2 \cdot 10^2$	$1.9 \cdot 10^2$
SD (μm)	$2 \cdot 10$	$5 \cdot 10$

TABLE C.2: Stylus profilometry (Dektak XT) measurements of patterned SU-8 2050 spincoated at 1500 rpm and 1000 rpm.

C.2 PDMS-molding data

Type	1		2		3		Mean		SD
	#Channels	#Filled	Fraction Filled	#Filled	Fraction Filled	#Filled	Fraction Filled	Fraction	Filled
2	426	426	1.00	426	1.00	426	1.00	1.00	0.00
4	160	160	1.00	160	1.00	160	1.00	1.00	0.00
5	106	106	1.00	106	1.00	33	0.31	0.77	0.40
3	320	320	1.00	320	1.00	320	1.00	1.00	0.00
32	213	213	1.00	213	1.00	213	1.00	1.00	0.00
34	128	128	1.00	128	1.00	128	1.00	1.00	0.00
1	492	492	1.00	492	1.00	492	1.00	1.00	0.00
31	278	278	1.00	278	1.00	278	1.00	1.00	0.00
33	148	148	1.00	148	1.00	141	0.95	1.00	0.03
35	62	62	1.00	61	0.98	56	0.90	1.00	0.05

TABLE C.3: Different types of straight channel PDMS stamps produced with fluoresceine added at 0 min after bonding. The number and percentage of channels filled with fluorescent fluid was measured (Olympus IX71). Experiment was done in triplicate.

Type	1		2		3		Mean		SD
	#Channels	#Filled	Fraction Filled	#Filled	Fraction Filled	#Filled	Fraction Filled	Fraction	Filled
2	426	1	0.00	25	0.06	90	0.21	0.09	0.11
4	160	13	0.08	51	0.32	151	0.90	0.45	0.45
5	106	2	0.02	25	0.24	106	1.00	0.42	0.52
3	320	3	0.01	36	0.11	200	0.63	0.25	0.33
32	213	1	0.00	17	0.08	7	0.03	0.04	0.04
34	128	6	0.05	3	0.02	0	0.00	0.02	0.02
1	492	5	0.01	66	0.13	21	0.04	0.06	0.06
31	278	5	0.02	2	0.01	52	0.19	0.07	0.10
33	148	15	0.10	17	0.11	3	0.02	0.08	0.05
35	62	1	0.02	0	0.00	1	0.02	0.01	0.01

TABLE C.4: Different types of straight channel PDMS stamps produced with fluoresceine added at 90 min after bonding. The number and percentage of channels filled with fluorescent fluid was measured (Olympus IX71). Experiment was done in triplicate.

C.2. PDMS-molding data

Type	#Channels	1		2		3		Mean	SD
		#Filled	Fraction Filled	#Filled	Fraction Filled	#Filled	Fraction Filled	Fraction Filled	Filled
2	426	5	0.01	0	0.00	16	0.04	0.02	0.02
4	160	139	0.87	15	0.09	30	0.19	0.38	0.42
5	106	51	0.48	56	0.53	56	0.53	0.51	0.03
3	320	38	0.12	0	0.00	28	0.09	0.07	0.06
32	213	55	0.26	0	0.00	5	0.02	0.09	0.14
34	128	4	0.03	0	0.00	0	0.00	0.01	0.02
1	492	0	0.00	15	0.03	18	0.04	0.02	0.02
31	278	3	0.01	88	0.32	9	0.03	0.12	0.17
33	148	2	0.01	1	0.01	0	0.00	0.01	0.01
35	62	5	0.08	1	0.02	0	0.00	0.03	0.04

TABLE C.5: Different types of straight channel PDMS stamps produced with fluoresceine added at 180 min after bonding. The number and percentage of channels filled with fluorescent fluid was measured (Olympus IX71). Experiment was done in triplicate.

	Type	Interspace width (μm)	0 min		90 min		180 min	
			Mean fraction filled	SD	Mean fraction filled	SD	Mean fraction filled	SD
5 μm , 20 μm and 30 μm channels	2	10	1.00	0.00	0.09	0.11	0.02	0.02
	4	20	1.00	0.00	0.45	0.45	0.38	0.42
	5	30	0.77	0.40	0.42	0.52	0.51	0.03
10 μm channels	3	10	1.00	0.00	0.25	0.33	0.07	0.06
	32	20	1.00	0.00	0.04	0.04	0.09	0.14
	34	40	1.00	0.00	0.02	0.02	0.01	0.02
3 μm channels	1	10	1.00	0.00	0.06	0.06	0.02	0.02
	31	20	1.00	0.00	0.07	0.10	0.12	0.17
	33	40	0.98	0.03	0.08	0.05	0.01	0.01
	35	100	0.96	0.05	0.01	0.01	0.03	0.04
	Overall		0.97	0.13	0.15	0.26	0.13	0.21

TABLE C.6: Fluoresceine was added to the inlet of a set PDMS stamps with straight channels at 0 min, 90 min or 180 min. Every experiment was done in triplicate, mean and standard deviation were calculated.

C.2.1 Grooves

Groove depth is measured with a stylus profilometer (Dektak XT) for the grooves used in cell experiments (2, 5 and 11). Each of the types were fabricated in triplicate from which 10 channels were measured, mean and standard deviation were calculated.

Experimental conditions: RF: 60 W, ICP: 100 W, O_2 : 10 sccm, SF_6 : 40 sccm, time: 7 min.

Type	Repeats	1 (μm)	2 (μm)	3 (μm)	4 (μm)	5 (μm)	6 (μm)	7 (μm)	8 (μm)	9 (μm)	10 (μm)	Mean (μm)	SD (μm)
2	A	2.9201	2.8236	2.9405	2.9255	2.9156	2.8869	2.8047	2.9249	2.8998	2.9230	2.90	0.05
	B	2.9584	2.9905	2.9506	2.9711	2.9751	2.9712	2.8429	2.9639	2.9603	2.9579	2.95	0.04
	C	3.0075	3.0002	3.0064	3.0082	2.8346	2.8870	3.0066	2.9967	2.8879	3.1028	2.97	0.08
											Total(2)	2.94	0.07
5	A	2.9787	2.9854	2.9784	2.9827	2.9782	2.9802	2.9781	2.9801	2.9772	2.9770	2.980	0.003
	B	2.9529	2.9538	2.9561	2.9533	2.9527	2.9510	2.9677	2.9708	2.9660	2.9581	2.96	0.01
	C	2.9381	2.9359	2.9351	2.9336	2.9370	2.9325	2.9704	2.9673	2.9706	2.9705	2.95	0.02
											Total(5)	2.96	0.02
11	A	3.0011	2.8825	3.0015	3.3003	3.0055	2.9978	3.0040	2.9983	3.0055	3.0073	3.0	0.1
	B	2.8884	3.0025	3.0026	3.0031	2.9985	3.0015	3.0151	3.0008	3.0043	2.9987	2.99	0.04
	C	2.9717	2.8571	2.8562	2.9759	2.9329	2.8552	2.8620	2.9787	2.9716	2.9691	2.92	0.06
											Total(11)	2.98	0.08
											Total (2,5,11)	2.96	0.06

TABLE C.7: Dektak XT measurements of etched grooves (types 2, 5 and 11). Every type was produced in triplicate (A, B and C), on each the height of 10 different channels was measured.

Bibliography

- [1] B. J. Larson, "A Review of the History of Electrophysiology and Electroencephalography. Part II," *American Journal of EEG Technology*, vol. 3, pp. 61–64, sep 1963.
- [2] J. Bernsten, *Untersuchungen über den erregungsvorgang im Nerven- und Muskelsysteme*. Heidelberg: Carl Winters Universitätsbuchhandlung, 1871.
- [3] L. Galvani, *De viribus electricitatis in motu musculari commentarius*. 1791.
- [4] K. Czöndör, M. Garcia, A. Argento, A. Constals, C. Breillat, B. Tessier, and O. Thoumine, "Micropatterned substrates coated with neuronal adhesion molecules for high-content study of synapse formation," *Nature Communications*, vol. 4, p. 2252, aug 2013.
- [5] K. Lepeta, M. V. Lourenco, B. C. Schweitzer, P. V. Martino Adami, P. Banerjee, S. Catuara-Solarz, M. de La Fuente Revenga, A. M. Guillem, M. Haidar, O. M. Ijomone, B. Nadorp, L. Qi, N. D. Perera, L. K. Refsgaard, K. M. Reid, M. Sabbar, A. Sahoo, N. Schaefer, R. K. Sheean, A. Suska, R. Verma, C. Vicidomini, D. Wright, X.-D. Zhang, and C. Seidenbecher, "Synaptopathies: synaptic dysfunction in neurological disorders - A review from students to students," *Journal of neurochemistry*, vol. 138, pp. 785–805, sep 2016.
- [6] A. M. Belle, H. A. Enright, A. P. Sales, K. Kulp, J. Osburn, E. A. Kuhn, N. O. Fischer, and E. K. Wheeler, "Evaluation of in vitro neuronal platforms as surrogates for in vivo whole brain systems," *Scientific reports*, vol. 8, p. 10820, jul 2018.
- [7] M. K. B. Jonsson, T. A. B. van Veen, J. Synnergren, and B. Becker, "Towards Creating the Perfect In Vitro Cell Model," *Stem cells international*, vol. 2016, p. 3459730, 2016.
- [8] L. Conforti, "Patch-Clamp Techniques," in *Methods in Cell Biology* (N. B. T. C. P. S. B. F. E. Sperelakis, ed.), ch. Chapter 20, pp. 369–381, San Diego: Academic Press, 2012.
- [9] M. E. J. Obien, K. Deligkaris, T. Bullmann, D. J. Bakkum, and U. Frey, "Revealing neuronal function through microelectrode array recordings," *Frontiers in Neuroscience*, vol. 8, p. 423, 2015.
- [10] P. Shi, M. A. Scott, B. Ghosh, D. Wan, Z. Wissner-Gross, R. Mazitschek, S. J. Haggarty, and M. F. Yanik, "Synapse microarray identification of small molecules that enhance synaptogenesis," *Nature Communications*, vol. 2, no. 1, p. 510, 2011.
- [11] C. Hammond, "Chapter 1 - Neurons," in *Cellular and Molecular Neurophysiology (Fourth edition)* (C. B. T. C. Hammond and M. N. F. Edition), eds.), ch. 1, pp. 3–23, Boston: Academic Press, 2015.

- [12] G. Stuart, N. Sprutson, and M. Häusser, *Dendrites*. New York: Oxford University Press, 3 ed., 2016.
- [13] C. Hammond and M. Esclapez, “Chapter 6 - The chemical synapses,” in *Cellular and Molecular Neurophysiology (Fourth edition)* (C. B. T. C. Hammond and M. N. F. Edition), eds.), ch. 6, pp. 121–144, Boston: Academic Press, 2015.
- [14] C. Hammond, O. El Far, and M. Seagar, “Chapter 7 - Neurotransmitter release,” in *Cellular and Molecular Neurophysiology (Fourth edition)* (C. B. T. C. Hammond and M. N. F. Edition), eds.), ch. 7, pp. 145–169, Boston: Academic Press, 2015.
- [15] J. L. Goldberg, “How does an axon grow ?,” *Genes & Dev.*, vol. 17, no. 650, pp. 941–958, 2003.
- [16] H. Lodish, A. Berk, and S. Zipursky, “The Action Potential and Conduction of Electric Impulses,” in *Molecular Cell Biology*, ch. Section 21, W. H. Freeman, 2000.
- [17] M. D. Forrest, “The sodium-potassium pump is an information processing element in brain computation,” *Frontiers in Physiology*, vol. 5, p. 472, 2014.
- [18] G. J. Kress and S. Mennerick, “Action potential initiation and propagation: upstream influences on neurotransmission,” *Neuroscience*, vol. 158, pp. 211–222, jan 2009.
- [19] T. C. Südhof and R. C. Malenka, “Understanding synapses: past, present, and future,” *Neuron*, vol. 60, pp. 469–476, nov 2008.
- [20] P. Scheiffele, J. Fan, J. Choih, R. Fetter, and T. Serafini, “Neuroigin Expressed in Nonneuronal Cells Triggers Presynaptic Development in Contacting Axons,” *Cell*, vol. 101, pp. 657–669, jun 2000.
- [21] J. Jeon, M.-A. Oh, W. Cho, S.-H. Yoon, J. Y. Kim, and T. D. Chung, “Robust Induced Presynapse on Artificial Substrates as a Neural Interfacing Method,” *ACS Applied Materials & Interfaces*, vol. 11, pp. 7764–7773, feb 2019.
- [22] D. Schreiner, J. N. Savas, E. Herzog, N. Brose, and J. de Wit, “Synapse biology in the circuit-age paths toward molecular connectomics,” *Current Opinion in Neurobiology*, vol. 42, pp. 102–110, 2017.
- [23] D. Bagnard, “Molecular mechanisms of axonal growth,” in *Axon Growth and Guidance*, vol. 621, ch. Chapter 1:, pp. 1–12, Springer, jan 2007.
- [24] L. A. Lowery and D. V. Vactor, “The trip of the tip: understanding the growth cone machinery,” *Nature Reviews Molecular Cell Biology*, vol. 10, no. 5, pp. 332–343, 2009.
- [25] H. M. Buettner, R. N. Pittman, and J. K. Ivins, “A Model of Neurite Extension across Regions of Nonpermissive Substrate: Simulations Based on Experimental Measurement of Growth Cone Motility and Filopodial Dynamics,” *Developmental Biology*, vol. 163, no. 2, pp. 407–422, 1994.
- [26] D. Šmít, C. Fouquet, F. Pincet, M. Zapotocky, and A. Trembleau, “Axon tension regulates fasciculation/defasciculation through the control of axon shaft zippering,” *eLife*, vol. 6, p. e19907, apr 2017.
- [27] A. S. f. N. George J. Siegel, R. Wayne Albers, Scott Brady, Donald L. Price, “Basic neurochemistry: Molecular, cellular and medical aspects, ed 5. Edited by George, J. Siegel, Bernard W. Agranoff, R. Wayne Albers, and Perry B. Molinoff New York, Raven Press, 1994, 1080 pp, illustrated, \$84.00,” *Annals of Neurology*, vol. 36, p. 121, jul 1994.

- [28] M. Tessier-Lavigne and C. Goodman, “The Molecular Biology of Axon Guidance,” *Science (New York, N.Y.)*, vol. 274, pp. 1123–1133, dec 1996.
- [29] J. Tang, U. Rutishauser, and L. Landmesser, “Polysialic acid regulates growth cone behavior during sorting of motor axons in the plexus region,” *Neuron*, vol. 13, no. 2, pp. 405–414, 1994.
- [30] L. M. Y. Yu, N. D. Leipzig, and M. S. Shoichet, “Promoting neuron adhesion and growth,” *Materials Today*, vol. 11, no. 5, pp. 36–43, 2008.
- [31] M. Gonzalez, X. Guo, M. Lin, M. Stancescu, P. Molnar, S. Spradling, and J. J. Hickman, “Polarity Induced in Human Stem Cell Derived Motoneurons on Patterned Self-Assembled Monolayers,” *ACS Chemical Neuroscience*, vol. 10, pp. 2756–2764, jun 2019.
- [32] O. Feinerman, A. Rotem, and E. Moses, “Reliable neuronal logic devices from patterned hippocampal cultures,” *Nature Physics*, vol. 4, no. 12, pp. 967–973, 2008.
- [33] S. K. W. Dertinger, X. Jiang, Z. Li, V. N. Murthy, and G. M. Whitesides, “Gradients of substrate-bound laminin orient axonal specification of neurons,” *Proceedings of the National Academy of Sciences*, vol. 99, pp. 12542 LP – 12547, oct 2002.
- [34] S. Willerth, “Chapter 4 - Design considerations when engineering neural tissue from stem cells,” in *Engineering Neural Tissue from Stem Cells* (S. B. T. E. N. T. f. S. C. Willerth, ed.), ch. 4, pp. 65–88, Academic Press, 1 ed., 2017.
- [35] T. B. DeMarse, L. Pan, S. Alagapan, G. J. Brewer, and B. C. Wheeler, “Feed-Forward Propagation of Temporal and Rate Information between Cortical Populations during Coherent Activation in Engineered In Vitro Networks,” *Frontiers in neural circuits*, vol. 10, p. 32, apr 2016.
- [36] L. Pan, S. Alagapan, E. Franca, S. S. Leondopulos, T. B. DeMarse, G. J. Brewer, and B. C. Wheeler, “An in vitro method to manipulate the direction and functional strength between neural populations,” *Frontiers in neural circuits*, vol. 9, p. 32, jul 2015.
- [37] Y. Takayama, N. Kotake, T. Haga, T. Suzuki, and K. Mabuchi, “Formation of one-way-structured cultured neuronal networks in microfluidic devices combining with micropatterning techniques,” *Journal of Bioscience and Bioengineering*, vol. 114, no. 1, pp. 92–95, 2012.
- [38] M. K. Lewandowska, D. J. Bakkum, S. B. Rompani, and A. Hierlemann, “Recording Large Extracellular Spikes in Microchannels along Many Axonal Sites from Individual Neurons,” *PLOS ONE*, vol. 10, p. e0118514, mar 2015.
- [39] R. van de Wijdeven, O. H. Ramstad, V. D. Valderhaug, P. Köllensperger, A. Sandvig, I. Sandvig, and Ø. Halaas, “A novel lab-on-chip platform enabling axotomy and neuromodulation in a multi-nodal network,” *Biosensors and Bioelectronics*, vol. 140, p. 111329, 2019.
- [40] E. Malishev, A. Pimashkin, A. Gladkov, Y. Pigareva, A. Bukatin, V. Kazantsev, I. Mukhina, and M. Dubina, “Microfluidic device for unidirectional axon growth,” *Journal of Physics: Conference Series*, vol. 643, p. 12025, 2015.

- [41] J.-M. Peyrin, B. Deleglise, L. Saias, M. Vignes, P. Gougis, S. Magnifico, S. Betuing, M. Pietri, J. Caboche, P. Vanhoutte, J.-L. Viovy, and B. Brugg, "Axon diodes for the reconstruction of oriented neuronal networks in microfluidic chambers," *Lab on a Chip*, vol. 11, no. 21, pp. 3663–3673, 2011.
- [42] B. J. Dworak and B. C. Wheeler, "Novel MEA platform with PDMS microtunnels enables the detection of action potential propagation from isolated axons in culture," *Lab on a Chip*, vol. 9, no. 3, pp. 404–410, 2009.
- [43] J. le Feber, W. Postma, E. de Weerd, M. Weusthof, and W. L. C. Rutten, "Barbed channels enhance unidirectional connectivity between neuronal networks cultured on multi electrode arrays," *Frontiers in neuroscience*, vol. 9, p. 412, nov 2015.
- [44] A. Gladkov, Y. Pigareva, D. Kutyna, V. Kolpakov, A. Bukatin, I. Mukhina, V. Kazantsev, and A. Pimashkin, "Design of Cultured Neuron Networks in vitro with Predefined Connectivity Using Asymmetric Microfluidic Channels," *Scientific Reports*, vol. 7, no. 1, p. 15625, 2017.
- [45] J. Mai, L. Fok, H. Gao, X. Zhang, and M.-m. Poo, "Axon Initiation and Growth Cone Turning on Bound Protein Gradients," *The Journal of Neuroscience*, vol. 29, pp. 7450 LP – 7458, jun 2009.
- [46] J. Cools, D. Copic, Z. Luo, G. Callewaert, D. Braeken, and M. De Volder, "3D Microstructured Carbon Nanotube Electrodes for Trapping and Recording Electrogenic Cells," *Advanced Functional Materials*, vol. 27, p. 1701083, sep 2017.
- [47] J. J. FitzGerald, S. P. Lacour, S. B. McMahon, and J. W. Fawcett, "Microchannels as Axonal Amplifiers," *IEEE Transactions on Biomedical Engineering*, vol. 55, no. 3, pp. 1136–1146, 2008.
- [48] L. Pan, S. Alagapan, E. Franca, T. DeMarse, G. J. Brewer, and B. C. Wheeler, "Large extracellular spikes recordable from axons in microtunnels," *IEEE transactions on neural systems and rehabilitation engineering : a publication of the IEEE Engineering in Medicine and Biology Society*, vol. 22, pp. 453–459, may 2014.
- [49] R. M. Smeal, R. Rabbitt, R. Biran, and P. A. Tresco, "Substrate Curvature Influences the Direction of Nerve Outgrowth," *Annals of Biomedical Engineering*, vol. 33, no. 3, pp. 376–382, 2005.
- [50] J. S. Chua, C.-P. Chng, A. A. K. Moe, J. Y. Tann, E. L. K. Goh, K.-H. Chiam, and E. K. F. Yim, "Extending neurites sense the depth of the underlying topography during neuronal differentiation and contact guidance," *Biomaterials*, vol. 35, no. 27, pp. 7750–7761, 2014.
- [51] B. Black, V. Vishwakarma, K. Dhakal, S. Bhattarai, P. Pradhan, A. Jain, Y.-t. Kim, and S. Mohanty, "Spatial temperature gradients guide axonal outgrowth," *Scientific Reports*, vol. 6, p. 29876, jul 2016.
- [52] D. E. Koser, A. J. Thompson, S. K. Foster, A. Dwivedy, E. K. Pillai, G. K. Sheridan, H. Svoboda, M. Viana, L. d. F. Costa, J. Guck, C. E. Holt, and K. Franze, "Mechanosensing is critical for axon growth in the developing brain," *Nature Neuroscience*, vol. 19, p. 1592, sep 2016.
- [53] T. Honegger, M. A. Scott, M. F. Yanik, and J. Voldman, "Electrokinetic confinement of axonal growth for dynamically configurable neural networks," *Lab on a Chip*, vol. 13, no. 4, pp. 589–598, 2013.

-
- [54] D. J. Stevenson, T. K. Lake, B. Agate, V. Garcés-Chávez, K. Dholakia, and F. Gunn-Moore, "Optically guided neuronal growth at near infrared wavelengths," *Opt. Express*, vol. 14, no. 21, pp. 9786–9793, 2006.
- [55] L. Gu, B. Black, S. Ordonez, A. Mondal, A. Jain, and S. Mohanty, "Microfluidic control of axonal guidance," *Scientific Reports*, vol. 4, p. 6457, oct 2014.
- [56] C. Miller, S. Jeftinija, and S. Mallapragada, "Synergistic Effects of Physical and Chemical Guidance Cues on Neurite Alignment and Outgrowth on Biodegradable Polymer Substrates," *Tissue Engineering*, vol. 8, pp. 367–378, jul 2002.
- [57] A. Rajnicek, S. Britland, and C. McCaig, "Contact guidance of CNS neurites on grooved quartz: influence of groove dimensions, neuronal age and cell type," *Journal of Cell Science*, vol. 110, pp. 2905 LP – 2913, dec 1997.
- [58] Y.-A. Huang, C. T. Ho, Y.-H. Lin, C.-J. Lee, S.-M. Ho, M.-C. Li, and E. Hwang, "Nanoimprinted Anisotropic Topography Preferentially Guides Axons and Enhances Nerve Regeneration," *Macromolecular Bioscience*, vol. 18, p. 1800335, dec 2018.
- [59] R. Barillé, R. Janik, S. Kucharski, J. Eyer, and F. Letournel, "Photo-responsive polymer with erasable and reconfigurable micro- and nano-patterns: An in vitro study for neuron guidance," *Colloids and Surfaces B: Biointerfaces*, vol. 88, no. 1, pp. 63–71, 2011.
- [60] B. Kaehr, R. Allen, D. J. Javier, J. Currie, and J. B. Shear, "Guiding neuronal development with in situ microfabrication," *Proceedings of the National Academy of Sciences of the United States of America*, vol. 101, pp. 16104 LP – 16108, nov 2004.
- [61] C. Simitzi, A. Ranella, and E. Stratakis, "Controlling the morphology and outgrowth of nerve and neuroglial cells: The effect of surface topography," *Acta Biomaterialia*, vol. 51, pp. 21–52, 2017.
- [62] J. W. Lee, K. S. Lee, N. Cho, B. K. Ju, K. B. Lee, and S. H. Lee, "Topographical guidance of mouse neuronal cell on SiO₂ microtracks," *Sensors and Actuators B: Chemical*, vol. 128, no. 1, pp. 252–257, 2007.
- [63] J. Zhang, S. Venkataramani, H. Xu, Y.-K. Song, H.-K. Song, G. T. R. Palmore, J. Fallon, and A. V. Nurmikko, "Combined topographical and chemical micropatterns for templating neuronal networks," *Biomaterials*, vol. 27, no. 33, pp. 5734–5739, 2006.
- [64] M. J. Mahoney, R. R. Chen, J. Tan, and W. Mark Saltzman, "The influence of microchannels on neurite growth and architecture," *Biomaterials*, vol. 26, no. 7, pp. 771–778, 2005.
- [65] A. Bédier, C. Vieu, F. Arnauduc, J.-C. Sol, I. Loubinoux, and L. Vaysse, "Engineering of adult human neural stem cells differentiation through surface micropatterning," *Biomaterials*, vol. 33, no. 2, pp. 504–514, 2012.
- [66] W. Li, Q. Y. Tang, A. D. Jadhav, A. Narang, W. X. Qian, P. Shi, and S. W. Pang, "Large-scale Topographical Screen for Investigation of Physical Neural-Guidance Cues," *Scientific Reports*, vol. 5, p. 8644, mar 2015.
- [67] J. Terryn, M. Welkenhuysen, O. Krylychkina, A. Firrincieli, A. Andrei, V. Reumers, P. Van Damme, D. Braeken, and C. Verfaillie, "Topographical Guidance of PSC-Derived Cortical Neurons," *Journal of Nanomaterials*, vol. 2018, pp. 1–10, oct 2018.

- [68] B. L. Leigh, K. Truong, R. Bartholomew, M. Ramirez, M. R. Hansen, and C. A. Guymon, "Tuning Surface and Topographical Features to Investigate Competitive Guidance of Spiral Ganglion Neurons," *ACS Applied Materials & Interfaces*, vol. 9, pp. 31488–31496, sep 2017.
- [69] D. Y. Fozdar, J. Y. Lee, C. E. Schmidt, and S. Chen, "Hippocampal neurons respond uniquely to topographies of various sizes and shapes," *Biofabrication*, vol. 2, no. 3, p. 35005, 2010.
- [70] N. Gomez, S. Chen, and C. E. Schmidt, "Polarization of hippocampal neurons with competitive surface stimuli: contact guidance cues are preferred over chemical ligands," *Journal of the Royal Society, Interface*, vol. 4, pp. 223–233, apr 2007.
- [71] N. Gomez, Y. Lu, S. Chen, and C. E. Schmidt, "Immobilized nerve growth factor and microtopography have distinct effects on polarization versus axon elongation in hippocampal cells in culture," *Biomaterials*, vol. 28, no. 2, pp. 271–284, 2007.
- [72] H. Francisco, B. B. Yellen, D. S. Halverson, G. Friedman, and G. Gallo, "Regulation of axon guidance and extension by three-dimensional constraints," *Biomaterials*, vol. 28, no. 23, pp. 3398–3407, 2007.
- [73] J. A. Fantuzzo, R. P. Hart, J. D. Zahn, and Z. P. Pang, "Compartmentalized Devices as Tools for Investigation of Human Brain Network Dynamics," *Developmental Dynamics*, vol. 248, pp. 65–77, jan 2019.
- [74] R. Habibey, S. Latifi, H. Mousavi, M. Pesce, E. Arab-Tehrany, and A. Blau, "A multielectrode array microchannel platform reveals both transient and slow changes in axonal conduction velocity," *Scientific Reports*, vol. 7, no. 1, p. 8558, 2017.
- [75] N. Hong, S. Joo, and Y. Nam, "Characterization of Axonal Spikes in Cultured Neuronal Networks Using Microelectrode Arrays and Microchannel Devices," *IEEE Transactions on Biomedical Engineering*, vol. 64, no. 2, pp. 492–498, 2017.
- [76] R. Renault, J.-B. Durand, J.-L. Viovy, and C. Villard, "Asymmetric axonal edge guidance: a new paradigm for building oriented neuronal networks," *Lab on a Chip*, vol. 16, no. 12, pp. 2188–2191, 2016.
- [77] R. Habibey, A. Golabchi, S. Latifi, F. Difato, and A. Blau, "A microchannel device tailored to laser axotomy and long-term microelectrode array electrophysiology of functional regeneration," *Lab on a Chip*, vol. 15, no. 24, pp. 4578–4590, 2015.
- [78] R. Habibey, A. Golabchi, and A. Blau, "Microchannel Scaffolds for Neural Signal Acquisition and Analysis BT - Neurotechnology, Electronics, and Informatics," (Cham), pp. 47–64, Springer International Publishing, 2015.
- [79] R. Renault, N. Sukenik, S. Descroix, L. Malaquin, J.-L. Viovy, J.-M. Peyrin, S. Bottani, P. Monceau, E. Moses, and M. Vignes, "Combining Microfluidics, Optogenetics and Calcium Imaging to Study Neuronal Communication In Vitro," *PLOS ONE*, vol. 10, p. e0120680, apr 2015.
- [80] K. Shimba, K. Sakai, T. Isomura, K. Kotani, and Y. Jimbo, "Axonal conduction slowing induced by spontaneous bursting activity in cortical neurons cultured in a microtunnel device," *Integrative Biology*, vol. 7, pp. 64–72, nov 2014.

-
- [81] K. Shimba, A. Saito, A. Takeuchi, Y. Takayama, K. Kotani, and Y. Jimbo, "Neural Transplantation Model Using Integration Co-Culture Chamber," *Electronics and Communications in Japan*, vol. 97, pp. 36–43, feb 2014.
- [82] P. Wieringa, R. Wiertz, E. de Weerd, and W. Rutten, "Bifurcating microchannels as a scaffold to induce separation of regenerating neurites," *Journal of neural engineering*, vol. 7, p. 16001, feb 2010.
- [83] R. Morales, M. Riss, L. Wang, R. Gavín, J. A. Del Río, R. Alcubilla, and E. Claverol-Tinturé, "Integrating multi-unit electrophysiology and plastic culture dishes for network neuroscience," *Lab on a Chip*, vol. 8, no. 11, pp. 1896–1905, 2008.
- [84] E. Claverol-Tinture, J. Cabestany, and X. Rosell, "Multisite Recording of Extracellular Potentials Produced by Microchannel-Confined Neurons In-Vitro," *IEEE Transactions on Biomedical Engineering*, vol. 54, no. 2, pp. 331–335, 2007.
- [85] A. M. Taylor, M. Blurton-Jones, S. W. Rhee, D. H. Cribbs, C. W. Cotman, and N. L. Jeon, "A microfluidic culture platform for CNS axonal injury, regeneration and transport," *Nature Methods*, vol. 2, no. 8, pp. 599–605, 2005.
- [86] P. M. Holloway, G. I. Hallinan, M. Hegde, S. I. R. Lane, K. Deinhardt, and J. West, "Asymmetric confinement for defining outgrowth directionality," *Lab on a Chip*, vol. 19, no. 8, pp. 1484–1489, 2019.
- [87] T. Akashi and Y. Yoshimura, "Deep reactive ion etching of borosilicate glass using an anodically bonded silicon wafer as an etching mask," *Journal of Micromechanics and Microengineering*, vol. 16, no. 5, pp. 1051–1056, 2006.
- [88] F. Laermer, S. Franssila, L. Sainiemi, and K. Kolari, "Chapter 21 - Deep Reactive Ion Etching," in *Micro and Nano Technologies* (M. Tilli, T. Motooka, V.-M. Airaksinen, S. Franssila, M. Paulasto-Kröckel, V. B. T. H. o. S. B. M. M. Lindroos, and T. S. Edition), eds.), pp. 444–469, Boston: William Andrew Publishing, 2015.
- [89] K. Nojiri, *Dry Etching Technology for Semiconductors*. Springer, jan 2015.
- [90] H. Jansen, H. Gardeniers, and M. D. Boer, "A survey on the reactive ion etching of silicon in microtechnology," *Journal of Micromechanics and Microengineering*, vol. 6, no. 1, 1996.
- [91] S. Mobini, Y. H. Song, M. W. McCrary, and C. E. Schmidt, "Advances in ex vivo models and lab-on-a-chip devices for neural tissue engineering," *Biomaterials*, vol. 198, pp. 146–166, 2019.
- [92] S. Kim, J. Park, A. Han, and J. Li, "Microfluidic systems for axonal growth and regeneration research," *Neural regeneration research*, vol. 9, pp. 1703–1705, oct 2014.
- [93] R. B. Campenot, "Local control of neurite development by nerve growth factor," *Proceedings of the National Academy of Sciences of the United States of America*, vol. 74, pp. 4516–4519, oct 1977.
- [94] B. Gale, A. Jafek, C. Lambert, B. Goenner, H. Moghimifam, U. Nze, and S. Kamarapu, "A Review of Current Methods in Microfluidic Device Fabrication and Future Commercialization Prospects," *Inventions*, vol. 3, p. 60, aug 2018.
- [95] Y. Xia and G. M. Whitesides, "SOFT LITHOGRAPHY," *Annual Review of Materials Science*, vol. 28, pp. 153–184, aug 1998.

- [96] P. Kim, K. W. Kwon, M. Park, S. Lee, S. M. Kim, and K. Suh, "Soft Lithography for Microfluidics: a Review," *Biochip Journal*, vol. 2(1), mar 2008.
- [97] A. M. Collins, "Chapter 5 - Physical Techniques," in *Nanotechnology Cookbook* (A. M. B. T. N. C. Collins, ed.), ch. chapter 5, pp. 205–253, Oxford: Elsevier, 2012.
- [98] J. A. Rogers and R. G. Nuzzo, "Recent progress in soft lithography," *Materials Today*, vol. 8, no. 2, pp. 50–56, 2005.
- [99] S. K. Sia and G. M. Whitesides, "Microfluidic devices fabricated in Poly(dimethylsiloxane) for biological studies," *ELECTROPHORESIS*, vol. 24, pp. 3563–3576, nov 2003.
- [100] V. C. Pinto, P. J. Sousa, V. F. Cardoso, and G. Minas, "Optimized SU-8 Processing for Low-Cost Microstructures Fabrication without Cleanroom Facilities. Micromachines," *Micromachines*, vol. 5, no. 3, pp. 783–755, 2014.
- [101] J. Friend and L. Yeo, "Fabrication of microfluidic devices using polydimethylsiloxane," *Biomicrofluidics*, vol. 4, p. 26502, mar 2010.
- [102] A. Campo and C. Greiner, "SU-8: a photoresist for high-aspect-ratio and 3D submicron lithography," *J. Micromech. Microeng.*, vol. 17, pp. 81–95, jun 2007.
- [103] F. Ceyssens and R. Puers, "SU-8 Photoresist BT," in *Encyclopedia of Nanotechnology* (B. Bhushan, ed.), pp. 2530–2543, Dordrecht: Springer Netherlands, 2012.
- [104] J.-B. Lee, K.-H. Choi, and K. Yoo, "Innovative SU-8 Lithography Techniques and Their Applications," *Micromachines*, vol. 6, pp. 1–18, jan 2015.
- [105] N. C. LaBianca and J. D. Gelorme, "High-aspect-ratio resist for thick-film applications," *Advanced Lithography*, 1995.
- [106] R. Martinez-Duarte and M. Madou, "SU-8 Photolithography and Its Impact on Microfluidics," in *Microfluidics and Nanofluidics Handbook: Fabrication, Implementation, and Applications*, pp. 231–268, CRC Press, sep 2010.
- [107] J. V. Crivello and J. H. W. Lam, "Photoinitiated cationic polymerization with triarylsulfonium salts," *Journal of Polymer Science Part A: Polymer Chemistry*, vol. 34, no. 16, pp. 3231–3253, 1996.
- [108] J. M. Shaw, J. D. Gelorme, N. C. LaBianca, W. E. Conley, and S. J. Holmes, "Negative photoresists for optical lithography," *IBM Journal of Research and Development*, vol. 41, no. 1.2, pp. 81–94, 1997.
- [109] E. Koukharenko, M. Kraft, G. Ensell, and N. Hollinshead, "A comparative study of different thick photoresists for MEMS applications," *Journal of Materials Science: Materials in Electronics*, vol. 16, pp. 741–747, nov 2005.
- [110] D. C. Duffy, J. C. McDonald, O. J. A. Schueller, and G. M. Whitesides, "Rapid Prototyping of Microfluidic Systems in Poly(dimethylsiloxane)," *Analytical Chemistry*, vol. 70, pp. 4974–4984, dec 1998.
- [111] R. Boya and G. Kulkarni, "Micromolding. A Soft Lithography Technique," in *Micro-manufacturing Processes*, pp. 329–347, Taylor & Francis, oct 2012.
- [112] T. Fujii, "PDMS-based microfluidic devices for biomedical applications," *Microelectronic Engineering*, vol. 61-62, pp. 907–914, 2002.

- [113] S. Torino, B. Corrado, M. Iodice, and G. Coppola, "PDMS-Based Microfluidic Devices for Cell Culture," *Inventions*, vol. 3, p. 65, sep 2018.
- [114] A. Piruska, I. Nikcevic, S. H. Lee, C. Ahn, W. R. Heineman, P. A. Limbach, and C. J. Seliskar, "The autofluorescence of plastic materials and chips measured under laser irradiation," *Lab on a Chip*, vol. 5, no. 12, pp. 1348–1354, 2005.
- [115] J. N. Lee, C. Park, and G. M. Whitesides, "Solvent Compatibility of Poly(dimethylsiloxane)-Based Microfluidic Devices," *Analytical Chemistry*, vol. 75, pp. 6544–6554, dec 2003.
- [116] S. Bhattacharya, A. Datta, J. M. Berg, and S. Gangopadhyay, "Studies on surface wettability of poly(dimethyl) siloxane (PDMS) and glass under oxygen-plasma treatment and correlation with bond strength," *Journal of Microelectromechanical Systems*, vol. 14, no. 3, pp. 590–597, 2005.
- [117] J. Harris, H. Lee, B. Vahidi, C. Tu, D. Cribbs, C. Cotman, and N. L. Jeon, "Non-plasma bonding of PDMS for inexpensive fabrication of microfluidic devices," *Journal of visualized experiments : JoVE*, no. 9, p. 410, 2007.
- [118] R. Freitag, "Protein Chromatography. Process Development and Scale-Up. By Giorgio Carta and Alois Jungbauer," *Biotechnology Journal*, vol. 5, oct 2010.
- [119] J. Vajda, W. Conze, and E. Müller, "Kinetic plots in aqueous size exclusion chromatography of monoclonal antibodies and virus particles," *Journal of Chromatography A*, vol. 1426, pp. 118–125, 2015.
- [120] Merck, "Antibody Basics."
- [121] ThermoFisher, "EZ-Link NHS-PEG4-Biotin," 2018.
- [122] Y. A. Cengel, J. Cimbala, and R. H. Turner, *Thermal-Fluid Sciences*. New York: McGraw-Hill Education, 5 ed., 2017.
- [123] H. Bruuse, "Hydraulic resistance and compliance," in *Theoretical microfluidics*, ch. Chapter 4:, New York: Oxford University Press, 2008.
- [124] MicroChem, "Processing guidelines for: SU-8 2000.5, SU-8 2002, SU-8 2005, SU-8 2007, SU-8 2010, SU-8 2015."
- [125] W. M. Moreau, "Optical exposure," in *Semiconductor lithography: Principles, Practices, and Materials*, ch. Chapter 8, New York: Plenum Press., 1988.
- [126] R. Chen and C.-M. Cheng, "Spin coating properties of SU8 thick-layer photoresist," *Proceedings of SPIE - The International Society for Optical Engineering*, vol. 4345, aug 2001.
- [127] R. Martinez-Duarte, G. Turon, P. Mukherjee, Q. Kang, and M. Madou, "Perspectives of Micro and Nanofabrication of Carbon for Electrochemical and Microfluidic Applications," in *Microfluidics and Microfabrication*, pp. 181–263, Springer, dec 2009.
- [128] R. Martinez-Duarte, "SU-8 photolithography as a toolbox for carbon MEMS," *Micro-machines*, vol. 5, pp. 766–782, oct 2014.
- [129] R. Barber, M. Ghantasala, R. Divan, D. Mancini, and E. Harvey, "Study of stress and adhesion strength in SU8 resist layers on silicon substrate with different seed layers," *Journal of Micro-nanolithography Mems and Moems*, vol. 6, jan 2010.

- [130] “Two-Chamber MEA to Unidirectionally Connect Neuronal Cultures,” *Proceeding of 9th Int. Meeting on Substrate-Integrated Microelectrode Arrays*, p. 259, 2014.
- [131] B. Li, M. Liu, and Q. Chen, “Low-stress ultra-thick SU-8 UV photolithography process for MEMS,” *Journal of Micro/Nanolithography, MEMS, and MOEMS*, vol. 4, pp. 1–6, oct 2005.
- [132] F. Walther, P. Davydovskaya, S. Zürcher, M. Kaiser, H. Herberg, A. M. Gigler, and R. W. Stark, “Stability of the hydrophilic behavior of oxygen plasma activated SU-8,” *Journal of Micromechanics and Microengineering*, vol. 17, no. 3, pp. 524–531, 2007.
- [133] D. Bodas and C. Khan-Malek, “Hydrophilization and hydrophobic recovery of PDMS by oxygen plasma and chemical treatment. An SEM investigation,” *Sensors and Actuators B: Chemical*, vol. 123, no. 1, pp. 368–373, 2007.
- [134] T. Senzai and S. Fujikawa, “Fast Hydrophobicity Recovery of the Surface-Hydrophilic Poly(dimethylsiloxane) Films Caused by Rechemisorption of Dimethylsiloxane Derivatives,” *Langmuir*, vol. 35, pp. 9747–9752, jul 2019.
- [135] S. H. Tan, N.-T. Nguyen, Y. C. Chua, and T. G. Kang, “Oxygen plasma treatment for reducing hydrophobicity of a sealed polydimethylsiloxane microchannel,” *Biomicrofluidics*, vol. 4, p. 32204, sep 2010.
- [136] S. Natyanun and N. Pussadee, “Hydrophobicity Recovery of Polydimethylsiloxane Treated with Oxygen Plasma and Ion Implantation,” *Journal of Physics: Conference Series*, vol. 1144, p. 12110, dec 2018.
- [137] J. Bacharouche, H. Haidara, P. Kunemann, M.-F. Vallat, and V. Roucoules, “Singularities in hydrophobic recovery of plasma treated polydimethylsiloxane surfaces under non-contaminant atmosphere,” *Sensors and Actuators A: Physical*, vol. 197, pp. 25–29, 2013.
- [138] F. Chen, J. Liu, Y. Cui, S. Huang, J. Song, J. Sun, W. Xu, and X. Liu, “Stability of plasma treated superhydrophobic surfaces under different ambient conditions,” *Journal of Colloid and Interface Science*, vol. 470, pp. 221–228, 2016.
- [139] G. Flores, W. Flack, and E. Tai, “Investigation of the properties of thick photoresist films,” *Proceedings of SPIE*, vol. 2195, pp. 733–750, may 1994.
- [140] Ibidi, “Culture-Insert 2 Well in u-Dish 35 mm.”
- [141] S. Neri, E. Mariani, A. Meneghetti, L. Cattini, and A. Facchini, “Calcein-acetyloxymethyl cytotoxicity assay: standardization of a method allowing additional analyses on recovered effector cells and supernatants,” *Clinical and diagnostic laboratory immunology*, vol. 8, pp. 1131–1135, nov 2001.
- [142] A. Kubo, H. Misonou, M. Matsuyama, A. Nomori, S. Wada-Kakuda, A. Takashima, M. Kawata, S. Murayama, Y. Ihara, and T. Miyasaka, “Distribution of endogenous normal tau in the mouse brain,” *The Journal of comparative neurology*, vol. 527, pp. 985–998, apr 2019.
- [143] J. Kapuscinski, “DAPI: a DNA-Specific Fluorescent Probe,” *Biotechnic & Histochemistry*, vol. 70, pp. 220–233, jan 1995.
- [144] S. MicroTec, “SUSS MA/BA Gen4 Series: Compact mask aligner platform for research and low-volume production.”

- [145] Bruker, “DektakXT - Technical details.”
- [146] MicroChem, “processing guidelines for SU-8 2025, SU-8 2035, SU-8 2050, SU-8 2075.”
- [147] Farnell, “Sylgard 184.”
- [148] Merck, “Corning microscope slides.”
- [149] ThermoFisher, “Fluorescein.”